Fast Joint design of RF and Gradient waveforms for MRI parallel excitation

by

Daehyun Yoon

A dissertation submitted in partial fulfillment
of the requirements for the degree of
Doctor of Philosophy
(Electrical Engineering : Systems)
in The University of Michigan
2012

Doctoral Committee:

Professor Douglas C. Noll, Co-Chair
Professor Jeffrey A. Fessler, Co-Chair
Professor Anna C. Gilbert
Professor Thomas L. Chenevert
Associate Professor Clayton D. Scott

ACKNOWLEDGEMENTS

I could not have done the work in this thesis without a tremendous amount of help, support, and sacrifice from many people. First of all, I would like to thank my co-chairs, Professor Douglas Noll and Professor Jeffrey Fessler for so much support both in research and life. I think the best teachers are those who just not only tell the good lessons, but also show them by their own examples, and I am so lucky to have such special ones as my co-chairs. I deeply appreciate that they granted me a chance to join their lab and waited for a long time with incredible patience until I could settle down to MRI research. I hope that someday I would be mature enough to pass along the great lessons I learned from them to others around me. I would also like to present profound gratitude to Professor Anna Gilbert for her great contribution in developing the core of my RF pulse design algorithms introduced in this thesis. Working with Anna was a very pleasant experience, and taught me a lot about how to enjoy research. Professor Thomas Chenevert and Professor Clayton Scott also deserve my gratitude for serving on my committee and returning very helpful suggestions for my thesis. I also deeply thank Korea Foundation of Advanced Studies for their longtime support, without which I could have not even considered to study abroad for a Ph. D program.

My lab experience was much better than I expected thanks to terrific senior researchers and lab mates. Dr. Luis Hernandez-Garcia always cheered me up with his great sense of humor, still filling me with an even larger amount of technical

MRI knowledge at the same time. Dr. Scott Peltier was approachable all the time, and open to my questions about his field though the quality of the questions was sometimes laughable. Dr. Jon-Fredrik Nielsen opened my eye to a new, important area of MRI with his specialty, which in fact became very critical later to search the next research topic after finishing my Ph. D program. I have always enjoyed working with him for his open mind and learned a lot from his extensive knowledge in both general MRI and pulse sequence implementation. I also thank my senior lab mates, Dr. Chunyu Yip and Dr. William Grissom for their huge help in learning the field of RF pulse design. Without their help, it would have taken me a painfully longer time even with much more efforts. My gratitude also goes to all other lab mates, Kiran, Christie, Hesam, Yash, Feng, Alan, Hao, and Matt for being open to talk for both work and fun all the time. I feel always lucky to have so approachable and pleasant people like those as my lab mates, especially considering my inactive personality.

I also present my deep gratitude to the administrative and technical staff in the lab and the EE:systems department. Ms. Ruth Halsey has been very kind in helping me out with so many lab businesses when I could not figure out what to do. Ms. Becky Turanski and Ms. Karen Liska always welcomed me even though I brought to them a very cumbersome paper work every time. I also like to thank Mr. Keith Newnham and Mr. Chuck Nicholas for their wonderful technical support, which was very important in making the lab life much smoother.

My gratitude should also go to my friends in Korea, U.S. and other countries. There are simply so many of them who cheered me up and encouraged me whenever I feel blue or frustrated. Without them, it would have been much tougher for me to live and work for such a long time in a foreign country. I am so sorry that I can not name all of them here for its limited space.

I would like to thank my parents, Jaehee Yoon and Naksoon Park, for their endless support and trust they have given to me, which was a huge propeller for me to go through difficult times. I also thank my brother, Hankyul, who had to take the role of the first son while I have to leave my family for a long time. I also thank my two little children, Eunji and Daham, for returning to me even more affection when I was supposed to provide it for them. Finally I would like to thank my wife, Sunyoung Park, who had to quit her job to come to U.S. with me and sacrifice so much for me since then. I can not thank her enough for her enormous love and support. I will try my best to make the time come soon that I could make it up for her.

Daehyun Yoon

Ann Arbor, Michigan

August 25th, 2012.

TABLE OF CONTENTS

LIST OF FIGURES

Figure

LIST OF TABLES

Table

CHAPTER I

Introduction

Magnetic resonance imaging (MRI) is imaging of the magnetization distribution developed by nuclei in the imaged object. Typically, water is selected as the target nucleus for imaging due to its abundance in the living organism. MRI has been increasingly used for its capability to provide superior contrast of soft tissues in high resolution compared with other popular imaging modalities such as computed tomography (CT), positron emission tomography (PET), and ultrasound. Roughly speaking, MRI is composed of two sequential procedures. The first procedure, excitation, is preparing the magnetization in the target imaging volume to be measurable. The second procedure, acquisition, is recording the Fourier transform samples of the prepared magnetization. One of the most important technical developments in MRI for last few decades is parallel imaging. In the conventional imaging, full k-space (Fourier space) measurements are measured sequentially with a single receiver coil. On the other hand, in parallel imaging, drastic reduction in the read-out period became possible because undersampled measurements recorded in parallel with each receiver coil could be combined together to reconstruct the image without aliasing artifacts.

Parallel excitation, which is simultaneous transmission of multiple radio-frequency

(RF) pulses through multiple independent RF transmission coils, has drawn great attention in the MRI community for past several years since its invention inspired by parallel imaging. The intuition behind the initial development for the parallel excitation was very analogous to that of the parallel imaging : using multiple coils to accelerate the excitation process, particularly multi-dimensional excitation. In early research, the main focus was mostly on developing a generic pulse design algorithm for uniform excitation. The advantage of parallel excitation over single coil excitation was often claimed with regard to its capability for undersampling excitation k-space, which is quite analogous to the claim used for parallel imaging. On the other hand, recent research tends to focus more on specific applications rather than on general pulse design methods. Fat-water selective excitation, signal loss correction in blood oxygenation level dependent (BOLD) functional MRI (fMRI), banding artifact correction in balanced steady-state free precession (SSFP) are such examples, and in those cases, the capability of parallel excitation to efficiently tailor excitation pattern to local off-resonance was exploited.

As briefly mentioned above, many theoretical pulse design methods and their experimental results were published, but we still have several unsolved issues that are very critical in deploying parallel excitation in practical and clinical cases. Such problems include fast computation, joint optimization of RF and gradient waveforms, and constraining specific absorption rate (SAR) for subject safety.

An MRI scanning procedure can start only after the RF pulses are prepared, so the online computation is quite an essential condition for a pulse design method to be practical. Unfortunately, in parallel excitation, we have to compute RF pulses for each transmission coil, which naturally increases the computational demand. Therefore, it is obvious that benefits of parallel excitation would be severely compromised

without developing a fast computation scheme.

Joint optimization of RF pulse and gradient waveforms is another challenge in parallel excitation. In excitation procedure, RF pulse and grdient waveforms together determines the excitation accuracy. However, in most parallel RF excitation pulse design algorithms including the pioneering investigations [1, 2], only RF pulse waveforms were optimized, and little attention has been paid to designing optimal gradient waveforms. Therefore, it is quite likely that we can further improve the excitation accuracy by developing a joint optimization scheme for RF pulse and gradient waveforms.

In all RF pulse design algorithms, the RF pulse should be constrained by the power deposition into the subject for the safety of the subject. Unfortunately, considering RF pulse power constraints in the RF pulse design algorithm poses a very difficult issue especially to parallel excitation. To estimate the RF power deposition pattern at one location, one needs to know the deposited RF pulse pattern and the subject specific parameters such as permitivity and conductivity of that location. Both the RF pulse and the subject parameters are spatially varying, so they can not be predicted in advance. Therefore, for the accurate estimation of local pulse power deposition, they first need to be measured, and then complex computer simulation should be followed using the measurements to compute the actual power deposition. This process can take a very long time, and incorporating it into an RF pulse design algorithm to give a feedback to modify the RF pulse is even more difficult. Therefore considering the local RF pulse power deposition in the pulse design has still remained as a considerably challenging issue.

In this research, we worked on solving the first two issues mentioned above : fast computation and joint optimization. Particularly, we focused on the pulse sequence

where trains of weighted slice-selective RF pulses interleaved by in-plane gradient blips are transmitted. In this pulse sequence, the number of unknown parameters for the RF and gradient waveforms are reduced significantly compared to the conventional pulse design methods that discretize the RF pulse and gradient waveforms with a few micro seconds sampling time, yielding thousands of samples to compute. Also, the size of the excitation pattern considered in the optimization decreases by a large amount since the guaranteed slice-selectivity of the pulse sequence allows us to consider only the selected volume, whereas in the conventional method, all volume within the territory of the transmission coils should be considered. We introduce a set of algorithms to jointly optimize the RF pulse and gradient waveforms for the proposed pulse sequence, and demonstrate their effectiveness mainly by computer simulation.

The chapters after this introduction are organized as following. In chapter II, the background about general MRI and MRI parallel excitation is briefly described. In chapter III, a basic application of parallel excitation for pseudo-continuous arterial spin labeling (PCASL) is presented. In chapter IV and V, two applications of our joint pulse design method in a small-tip angle domain are covered together with simulation results and adaptations specific to each application. In chapter VI, a large tip-angle RF pulse design method is proposed and simulation results for the uniform excitation are presented. Finally chapter VII presents summary of our research and a list of future work.

CHAPTER II

Background

2.1 MRI excitation overview

2.1.1 MRI in general

Magnetic Resonance Imaging(MRI) produces an image of magnetization developed by nuclear spins. Quite a few nuclei are capable of developing magnetization, but only several nuclei are practical useful. The most typical target for MRI in the clinical setting is the proton(^1H) because of its abundance in the living organism in the form of water(H_2O). The net magnitude of magnetization in a unit volume is proportional to the proton density in the volume, so contrast of an MRI magnitude image depends on the proton density.

MRI scanning consists of two sequential procedures, which are excitation and acquisition. In the acquisition step, Fourier transform samples of the transverse(xy plane) magnetization in the target object are measured. However, the initial magnetization is relaxed along the main field aligned perpendicular to the transverse plane, leaving no measurable portion of magnetization in the beginning. Therefore, the magnetization in the imaging region of interest should be tipped down toward the transverse plane prior to the acquisition step. This tipping process is called excitation.

2.1.2 MRI excitation

To tip the magnetization down on the transverse plane, we use the principle that, in the presence of an external magnetic field, the component of magnetization orthogonal to the direction of an applied magnetic field precesses around the magnetic field. The quantitative description of this phenomenon is the Bloch equation [3]:

$$\frac{d\mathbf{M}(x,y,z,t)}{dt} = \mathbf{M}(x,y,z,t) \times \gamma\mathbf{B}(x,y,z,t), \tag{2.1}$$

where x,y,z are spatial coordinates and t is a time coordinate. $\mathbf{M}$ and $\mathbf{B}$ are both 3D spatial vectors, so they have x,y,z directional components. For example, $\mathbf{M}(x,y,z,t) = (M_x(x,y,z,t), M_y(x,y,z,t), M_z(x,y,z,t))$. γ is the nuclei dependent gyromagnetic ratio, and it is 42.58 MHz/T for the proton. The precession frequency of the magnetization, ω, is also determined from the Bloch equation, which is $\omega = -\gamma\mathbf{B}$.

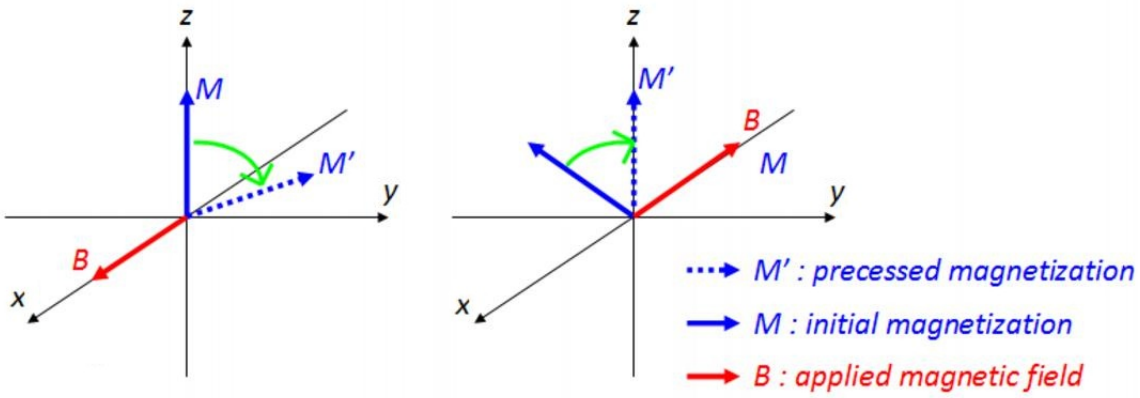

Figure 2.1: An example of tipping by magnetization precession around an external magnetic field, B, aligned along x axis. Note that the tipping can be up or down depending on the direction of both the magnetization and the B field.

In MRI, the net $\mathbf{B}$ field applied to the object consists of 3 different components: B0 main field, linear gradient fields, and B1 field. The B0 main field is a very

strong static magnetic field along the longitudinal axis that is used to align randomly oriented initial magnetization along it. The linear gradient fields are also aligned along the longitudinal axis, but its strength varies linearly along each spatial axis. For example, x-directional gradient field, **Gx**, is modeled as $\mathbf{Gx}(x, y, z, t) = (0, 0, xG_x(t))$ where x, y, z are spatial coordinates for x, y, z axis, $G_x(t)$ is the x gradient waveform, and t is a time coordinate. Unlike the other two magnetic fields, the B1 field is magnetic field well approximated to have only x and y directional components, and often called the RF field. In Figure 2.1, only B1 field is applied without B0 main field or gradient fields for a simple demonstration. However, the net B field in most MRI has both the longitudinal and transverse components as in Figure 2.2. For example, the net B field at a spatial location (x, y, z) at time t is modeled as

$$\mathbf{B}_{net}(x, y, z, t) = (\mathrm{Re}(b(t)), \mathrm{Im}(b(t)), B0 + xG_x(t) + yG_y(t) + zG_z(t)) \tag{2.2}$$

where $b(t)$ is the RF field waveform(or RF pulse waveform), $G_x(t), G_y(t), G_z(t)$ are x, y, and z directional gradient waveforms. As soon as the magnetization comes to have a transverse plane component from tipping by the RF pulse, it also starts to precess around the longitudinal axis because of the B0 field. The precession frequency around the B0 field is much higher than that around B1 field, for $|B0| \gg |B1|$. If the RF pulse remains static, the magnetization may oscillate between the first and the second example in Figure 2.1 yielding virtually no tipping at all. This indicates that the precession rate of the transverse magnetization around the B0 field and the RF pulse's phase change along with time are closely related regarding the tipping direction of the magnetization. For example, to consistently tip down the magnetization in one direction, the resonance frequency of the transverse magnetization and the frequency of the RF pulse should be same.

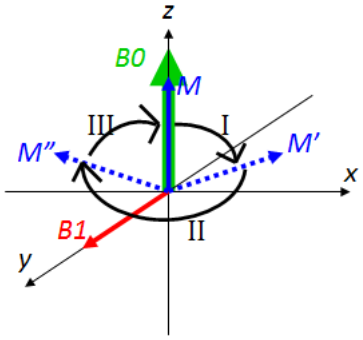

Figure 2.2: An example of no net tipping. I) The initial magnetization **M** gets tipped down resulting in **M**′. II) The transverse component of **M**′ precesses around the main field **B0** resulting in **M**". III) **M**" gets tipped up by the **B1** field, yielding no net transverse magnetization. The actual trajectory of the magnetization is more complex than what's explained above, because both **B1** and **B0** fields are continuously applied in time, .

2.1.3 MRI excitation pulse design problem

The excitation pulse design problem is defined as determining both the RF pulse and linear gradient waveforms to create a desired magnetization pattern. Mathematical formulation of the problem is as followings.

• **Unknown input to determine**

- RF pulse waveform : Complex valued $b(t)$.

- Linear gradient waveforms : Real valued $G_x(t)$, $G_y(t)$, $G_z(t)$.

t is a time coordinate ranging from 0 to T, and T is the length of RF pulse and gradient waveforms. T may be a requirement from the problem specification but often is a design choice though in most cases, a shorter T is preferred to reduce the total imaging time.

• **Desired output**

Magnetization pattern at time T : $\mathbf{M}(x, y, z, T)$.

• **Input-output relationship**

Bloch equation

Initial condition of magnetization : $\mathbf{M}(x, y, z, 0)$

• **Constraints**

RF pulse : maximum absolute amplitude and power is limited.

Linear gradients : maximum absolute amplitude and maximum absolute first order derivative (so called slew rate) are limited.

For many excitation pulse design problems, the initial condition $\mathbf{M}(x, y, z, 0)$ is $(0, 0, M_0(x, y, z))$, and the desired output $\mathbf{M}(x, y, z, T)$ is $(M_0(x, y, z)\sin\theta(x, y, z)$, 0, $M_0(x, y, z)\cos\theta(x, y, z))$ where θ is called the tip angle(or flip angle), the angle between the initial magnetization and the final tipped magnetization. In that case, we seek to determine the RF pulse and gradient waveforms to make θ uniform in the imaging region of the interest, and zero outside the imaging region of interest. For example, $\theta(x, y, z) = \theta_0$ if $(x, y, z) \in \mathbf{R}$, and 0 otherwise where $\mathbf{R}$ is the set of coordinates for the imaging region of interest. In a typical slice-selective 2D imaging, $\mathbf{R}$ is defined to be $\left\{(x, y, z)|rect\left(\frac{z-z_0}{\text{slice thickness}}\right) = 1\right\}$ as in Figure 2.3. There are also other MRI applications where the problem setting and the required output are different from the above. For example, inversion pulse design, refocusing pulse design, complex pattern excitation pulse design, and magnitude-optimized pattern excitation pulse design are such cases.

2.2 Brief review on early MRI excitation pulse design methods

2.2.1 A naive analysis for the 1-D selective excitation problem

As we see in the Figure 2.2, it was the precession of transverse magnetization that prevented magnetization from tipping consistently down toward the transverse plane. A simple solution to this problem is to make the RF field precess around the

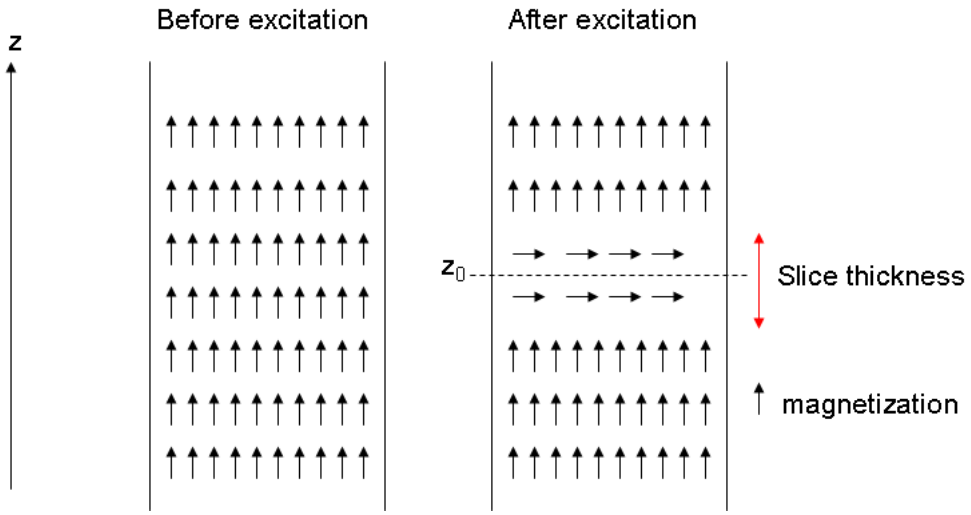

Figure 2.3: A slice selective excitation for 2D imaging. z_0 is the slice center

B0 field in the same rate with the transverse magnetization. The analysis of the magnetization precession trajectory becomes much easier in the rotating frame of reference. In the rotating frame, x and y coordinate axes are rotating around the z axis at the same frequency with the transverse magnetization. This makes the effective B0 field zero, for the transverse component is not precessing in the rotating frame. If the RF pulse is also rotating at the same frequency, its phase remains the same in the rotating frame. Because the phase of the RF field and the transverse magnetization remain the same, the magnetization is consistently tipped down as in the first example of Figure 2.1. If the precession frequency of the transverse magnetization is very different from that of the RF pulse, then magnetization would not be tipped down as in Figure 2.2.

Therefore, the frequency component of the RF pulse and the precession frequency(or resonance frequency) of the transverse magnetization determines whether tipping happens effectively or not. The resonance frequency of the transverse magnetization can be spatially controlled using linear gradients, and by matching the frequency spectrum of the RF pulse to the resonance frequency range of the selected

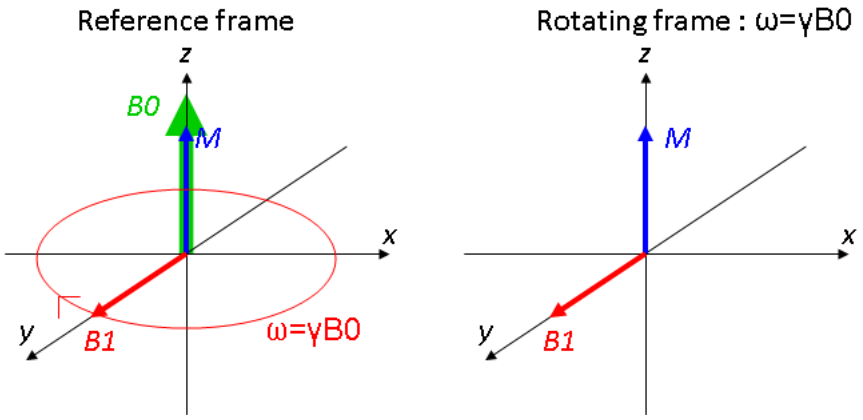

Figure 2.4: An example of rotating frame. The B1 field rotating around B0 field at the frequency ω remains static in the rotating frame of the frequency ω

region, a simple one dimensional excitation can be achieved. For example, if a static z-gradient, G_z, is on, the resonance frequency of the transverse magnetization is determined as $\omega(z) = \gamma B(z) = \gamma(B_0 + zG_z)$. If a slice ranging from $-z0$ to $z0$ is to be excited, then the frequency spectrum of the RF pulse should be uniform range from $\omega(-z0)$ to $\omega(z0)$, which implies that the resulting RF pulse envelope would be in a sinc shape. Though this is a very rough qualitative analysis because the Bloch equation is not linear with respect to the RF pulse, it works surprisingly well in most practical cases. In fact, to achieve 1-D slice selective excitation, most clinical MRI scanners typically use an RF pulse of fixed bandwidth and the desired slice thickness is achieved by matching the resonance frequency range of the selected slice to that of the RF pulse.

2.2.2 Non-iterative pulse design methods in a small tip angle domain

Jaynes [4] and Hoult [5] independently showed that Bloch equation could be approximated as a linear equation with respect to the RF pulse when the initial magnetization is fully relaxed, and the tip angle is small enough that $\sin(\theta) \simeq \theta$. Their analyses were based on a so-called perturbation theory in physics. The linearized

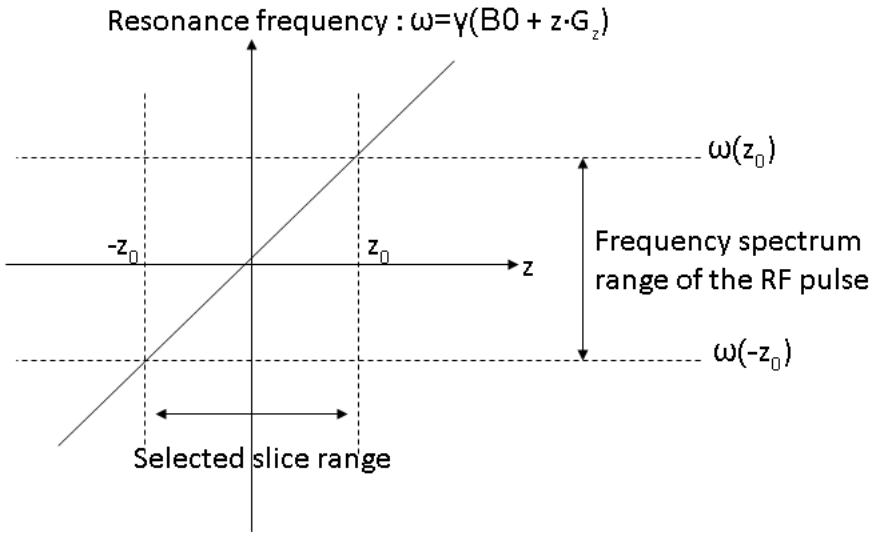

Figure 2.5: The spectrum of the RF pulse and the resonance frequency range of transverse magnetization in a simple 1D slice selective excitation

equation indicated that the Fourier transform of the RF pulse is the excited transverse magnetization pattern as in the following equation.

$$\mathbf{M_{xy}}(z) = iM_0 e^{-i\gamma z G_z(t)} \int_0^T b(t) e^{i\gamma z G_z(t)} dt \tag{2.3}$$

$\mathbf{M_{xy}}(z)$ is the transverse magnetization at z, $b(t)$ is the RF pulse waveform, T is the length of the RF pulse, and M_0 is the fully relaxed initial magnetization. The RF pulse to create a rectangular slice profile as in Figure 2.5 was determined to be the sinc pulse according to Eq.2.3. However, these methods were limited to one dimensionally selective excitation and were valid only in a small tip angle domain. Pauly [6] later presented a k-space analysis of selective excitation by extending the linearization of Bloch equation to describe multidimensional excitation. This method also inherited the assumption of small-tip angle excitation, but provided a more generalized view in designing both RF pulse and gradient waveforms. Pauly's analysis showed that the transverse magnetization pattern and the RF pulse had a multi-dimensional Fourier transform relationship as following.

First, a spatial frequency vector $\mathbf{k}(t)$ is defined as $\mathbf{k}(t) = -\gamma \int_t^T \mathbf{G}(s)ds$ where $\mathbf{G}(s)$ is a vector of linear gradient waveforms, and T is the length of the RF pulse and the linear gradient waveforms. For example, $\mathbf{G}(t) = (G_x(t), G_y(t), G_z(t))$. Then, we have

$$\mathbf{M_{xy}}(\mathbf{r}) = i\gamma M_0(\mathbf{r}) \int_0^T b(t) e^{i\mathbf{r}\cdot\mathbf{k}(t)} dt, \tag{2.4}$$

where $\mathbf{M_{xy}}(\mathbf{r})$ is a transverse magnetization at $\mathbf{r}$, which is a vector containing spatial coordinates. For example $\mathbf{r} = (x, y, z)$. In Eq.2.4, it is observed that $\mathbf{k}(t)$ forms a sampling trajectory of the spatial frequency space, while the traversed spatial frequency components are weighted by the samples of the RF pulse. One important contribution of the above analysis is that it enabled a k-space(or Fourier space) interpretation in the RF pulse and gradient waveform design. In other words, while gradient waveforms form the sampling trajectory in the k-space, RF pulses deposit the associated Fourier samples of the excitation pattern. Therefore an optimal k-space trajectory should traverse the k-space regions where corresponding k-space samples of the desired excitation pattern have large values to achieve high excitation accuracy. The optimized k-space trajectory could be easily translated to linear gradient waveforms later. Several multidimensional excitation pulse design methods based on using this k-space analysis [7, 8] were proposed. In these methods, the k-space trajectory was determined first, and the RF pulse waveform was computed by sampling Fourier transform values along the k-space trajectory and weighting them with the density compensation function. The density compensation was applied to correct for the non-uniform sampling density of the k-space trajectory as in the conjugate phase method [9] for the image reconstruction.

2.2.3 Iterative pulse design methods in a small tip angle domain

An iterative pulse design method based on the small tip angle excitation formulation was proposed by Yip et al. [10], and it was applied to the signal loss problem in functional MRI [11]. In the iterative method, the RF pulse waveform was decomposed into sequential time samples using a train of Dirac impulses with a sampling interval of Δt seconds, and the desired excitation pattern was uniformly sampled in the spatial domain. This procedure converted the continuous small tip angle approximation equation in Eq. 2.4 into a discrete matrix-vector equation as following.

$$\mathbf{m} \simeq \mathbf{A}\mathbf{b}, \tag{2.5}$$

where $\mathbf{m}$ contains the samples of the excited transverse magnetization pattern over a uniform Cartesian sampling grid, $\mathbf{b}$ is a vector containing time samples of the RF pulse, and $\mathbf{A}$ is a *system matrix* encoding the Fourier kernels determined by the k-space trajectory. For example, the elements of the matrix $\mathbf{A}$, a_{mn} is defined as

$$a_{mn} = i\gamma(\mathbf{r}_m)\Delta t e^{i\mathbf{r}_m \cdot \mathbf{k}(t_n)} \tag{2.6}$$

where t_n is the n-th sample time point, and $\mathbf{r}_m$ is the m-th spatial sample point. The off-resonance frequency due to magnetic field inhomogeneity can be easily incorporated into the system matrix, and in that case, a_{mn} is modified as following.

$$a_{mn} = i\gamma \mathbf{M_0}(\mathbf{r}_m)\Delta t e^{i\mathbf{r}_m \cdot \mathbf{k}(t_n) + i\Delta\omega(\mathbf{r}_m)(t_n - T)} \tag{2.7}$$

where $\Delta\omega(\mathbf{r}_m)$ is the off-resonance frequency at $\mathbf{r}_m$.

Using this model, an optimization problem was formulated with a cost function consisting of an excitation error term to enforce a small excitation error and a regularizer term to consider other constraints about the RF pulse. The cost function was given as

$$\hat{\mathbf{b}} = \arg\min_{\mathbf{b}} \left\{ \|\mathbf{Ab} - \mathbf{d}\|_W^2 + \mathbf{R}(\mathbf{b}) \right\} \tag{2.8}$$

where $\mathbf{d}$ is a vector including the samples of the desired excitation pattern, and $\mathbf{W}$ is a diagonal matrix indicating the excitation region of interest. $\mathbf{R}(\mathbf{b})$ is a regularizer that can serve different purposes depending on the constraint of the problem. For example, to reduce the total RF power deposition, $\mathbf{R}(\mathbf{b}) = \lambda\|\mathbf{b}\|^2$ can be used where λ is a parameter that the designer should choose to balance the excitation accuracy and the RF pulse power deposition.

In the iterative method, it becomes easier to employ a non-Cartesian k-space trajectory such as a spiral trajectory than the previous k-space domain methods [7, 8], for there is no need to explicitly compute the density compensation function. Also, it is flexible enough to adopt various factors in the cost function. For example, magnetic field inhomogeneity during excitation, spatial masking for the don't-care region in the excitation pattern, and net RF power deposition are easily included by either modifying the elements of the system matrix or adding a regularization term to the cost function as in Eq.2.8. It is very hard or impossible to compute the optimal RF pulse considering these conditions if we use the non-iterative methods.

The iterative method applied in [11] depended upon inverse Fourier transform of the desired pattern to determine the optimal k-space trajectory. However, one can not use the inverse Fourier transform approach in case that the desired pattern includes a don't-care region. For example, in case of exciting a multidimensional

pattern in a brain, the desired excitation pattern is well defined only inside of the brain whereas the air space surrounding the brain has no magnetization and thus the excitation pattern may have any value in that region. In this case, the inverse Fourier transform can not be taken because the excitation pattern is not well determined everywhere. To avoid the direct Fourier inversion, several methods were proposed. Suwit et al. [12] modeled the excitation pattern with a quadratic function, and designed the k-space trajectory based on that. Yip et al. [11] extrapolated the excitation pattern to the don't-care region with smoothness penalty and took the inverse Fourier transform of it.

In the aforementioned methods, optimization was mainly performed to obtain an effective RF pulse waveform, and less effort was invested in designing an optimal k-space trajectory. In attempt to further improve the excitation accuracy, several joint design methods for both RF pulse waveform and gradient waveforms have been recently developed. Yip et al [13] presented an optimization scheme that alternates minimization between the RF pulse and the parameterized k-space trajectory. In the method, the k-space trajectory was decomposed with a set of basis function, so the optimization of the k-space trajectory reduced to determining optimal parameters for the bases. Then, it repeated optimization of the k-space trajectory and the RF pulse until there is no significant improvement. At each iteration, the k-space trajectory was first fixed and the RF pulse was optimized using conjugate gradient algorithm, and then for the updated RF pulse, the parameters of the k-space trajectory was optimized using gradient descent algorithm. The cost function was non-linear with respect to the parameters of the k-space trajectory, so the gradient descent algorithm was used instead of the CG algorithm. This method was applied to determine optimal phase encoding locations of the EPI trajectory and showed improved performance,

though it occasionally suffered from divergence of the solution. Recently, Zelinski et el [14] recast the joint design problem as sparse approximation problem of the desired excitation pattern with a discrete set of Fourier bases, and presented a solution using basis pursuit algorithm [15]. They later extended the method to the parallel excitation pulse design [16]. Their method is very closely related to our proposed work, so the details would be covered in the Section 2.3.4.

All the pulse design methods introduced above are based on the small tip angle approximation, so they are limited to the small tip angle RF pulse design case. Many large tip angle excitation pulse design methods [17, 18, 19, 20] have been presented, but they all use predetermined gradient waveforms and optimized only the RF pulse. Because the k-space analysis is not valid in the large tip angle domain, the typical small tip-angle domain approach that first designs the k-space trajectory and then derives the gradient waveforms from it becomes much less insightful in the large tip angle excitation. The direct optimization of the linear gradient waveforms for the large tip angle excitation pulse design is still an open problem.

2.3 MRI parallel excitation

2.3.1 Motivation

In parallel excitation, multiple independent RF transmission coils are employed to simultaneously transmit multiple RF pulses. Because most of commercially available scanners are equipped with only a single coil RF transmission system, running parallel excitation definitely requires integration of additional hardware and RF pulse design software. Though this overhead is not so trivial, there are some promising applications that motivated the use of parallel excitation. One application is uniform excitation in high field MR imaging. In typical MRI scanning, volume coils such as a head coil array are assumed to have uniform sensitivity over the subject

such that uniform excitation can be performed with a single coil transmission system. However in high field greater than 3T, there have been many reports showing severe B1 field inhomogeneity of single RF transmission system. The inhomogeneity of transmission coil's sensitivity originates from various factors. One source is dielectric resonances due to shorter RF wavelength in high B0 field [21]. RF attenuation by tissue conductivity [22, 23] is another reason for the B1 field inhomogeneity in high field MR imaging. The absence of a single coil with uniform sensitivity in high field naturally gave rise to the idea of combining multiple transmission coils together to synthesize a uniform RF field, which can be done by parallel excitation. Another application is non-uniform, localized excitation. This application exploits the fact that the transmission coils adopted in parallel excitation usually have localized sensitivity. Therefore, it becomes much easier with parallel excitation to obtain a localized variation in the excitation pattern compared to the single coil transmission that depends entirely upon the linear gradients to create such a spatial variation. Applications with this type of intuition are mostly related with off-resonance correction. For example, water selective excitation in body imaging suffers from local off-resonance shifting the resonance frequency of the fat to that of water or vice versa, resulting unwanted excitation of fat. With parallel excitation [24, 25], each transmission coil can transmit an RF pulse whose carrier frequency is adjusted to compensate the off-resonance frequency within its sensitivity territory can more effectively solve the issue than a single coil transmission case. There are also other applications with parallel excitation about off-resonance correction [26, 27, 28, 29].

2.3.2 Pioneering parallel excitation RF pulse design methods

Parallel excitation was first proposed by Katscher [1] and Zhu [2] inspired by parallel imaging [30, 31, 32], which accelerates image acquisition by using multiple receive

coils with spatially localized sensitivity. In parallel imaging, combining undersampled k-space data from each receive coil allowed reconstructing the image without an aliasing artifact. Because the image acquisition speed was largely bounded by the time taken in traversing the readout k-space trajectory, parallel imaging was a breakthrough in attempt to reduce the image acquisition time. Since the multidimensional excitation in a small tip angle domain was also governed by Fourier transform as image reconstruction, the excitation pulse and gradient waveform length was also determined by the time taken in traversing the excitation k-space trajectory. Katscher [1] and Zhu [2] demonstrated that by using multiple RF transmission coils with localized sensitivity, an undersampled k-space trajectory can be used to excite a multidimensional pattern. In [2], it was also shown that the increased degree of freedom due to the increased number of pulses could be exploited to decrease RF power deposition in the imaging object.

Later, an iterative parallel excitation pulse design method [33], which is a generalized version of [10] for parallel excitation was proposed to improve the pulse design process. The small tip angle approximation in Eq.2.4 was modified to reflect that the net RF field reaching at a spatial location $\mathbf{r}$ is superposition of RF pulses transmitted from each coil. For example, $b_{net}(\mathbf{r},t) = \sum_{l=1}^{L} S_l(\mathbf{r}) b_l(t)$ where $b_{net}(\mathbf{r},t)$ is the net RF field at a spatial location $\mathbf{r}$ at time t, $S_l(\mathbf{r})$ is the l-th transmission coil's sensitivity, $b_l(t)$ is the RF pulse waveform of the l-th coil, and L is the total number of coils By replacing $b(t)$ in Eq.2.4 with $b_{net}(\mathbf{r},t)$, we obtain the small tip angle approximation equation for the parallel excitation as following.

$$\mathbf{M_{xy}}(\mathbf{r}) = i\gamma \mathbf{M_0}(\mathbf{r}) \sum_{l=1}^{L} S_l(\mathbf{r}) \int_0^T b_l(t) e^{i\mathbf{r}\cdot\mathbf{k}(t)} dt \tag{2.9}$$

The discrete approximation of the above equation in a matrix-vector form can be

acquired in a similar manner as in [10], and the resulting equation is presented in Eq.2.10.

$$\mathbf{m} \simeq \sum_{l=1}^{L} \mathbf{S}_l \mathbf{A} \mathbf{b}_l = \mathbf{A}_{full} \mathbf{b}_{full} \tag{2.10}$$

$\mathbf{A}_{full}$ is horizontal concatenation of matrices, $\mathbf{S}_l\mathbf{A}$, and $\mathbf{b}_{full}$ is a vertical concatenation of vectors, $\mathbf{b}_l$. $\mathbf{S}_l$ is a diagonal matrix containing samples of the l-th coil's sensitivity, and $\mathbf{b}_l$ is a vector composed of the time samples of the pulse from the l-th coil. $\mathbf{A}$ is the system matrix same as what is defined in Eq.2.5. The iterative parallel RF excitation pulse design has several advantages over [1]. For example, as in the single coil excitation, the iterative method automatically takes care of density compensation for a non-Cartesian k-space trajectory. Also, additional factors like the magnetic field inhomogeneity, power regulation, and spatial masking or weighting in the region of interest are easily incorporated into the pulse optimization process. The cost function for the optimization is defined by simply replacing $\mathbf{A}$ and $\mathbf{b}$ in Eq.2.8 with $\mathbf{A}_{full}$ and $\mathbf{b}_{full}$ respectively as following.

$$\hat{\mathbf{b}}_{full} = \arg\min_{\mathbf{b}_{full}} \left\{ \|\mathbf{A}_{full}\mathbf{b}_{full} - \mathbf{d}\|_W^2 + \mathbf{R}(\mathbf{b}_{full}) \right\} \tag{2.11}$$

2.3.3 Practical issues

Even though parallel excitation showed great potential in applications where multi-dimensional pulses are effective [11, 16, 24, 26, 27, 29, 34, 35] it faced a few important issues to solve before being deployed in clinical settings. First, it is computationally more demanding than the single coil excitation simply because there are more parameters to compute. The MRI scanning procedure can not start until RF

pulses are prepared, so a pulse design method becomes feasible only if the method runs quickly. Unfortunately, the on-line computation requirement becomes harder to meet for the parallel excitation. In most parallel excitation design methods, it is assumed that the transmission coil sensitivities are known, which, in fact, need to be measured by scanning the object. Therefore, for most MRI scans using parallel excitation, a prescan step is required to acquire the sensitivity pattern, and then the pulse computation gets started. Moreover, the parallel excitation pulse computation may take longer than the single coil case because there are more pulses to compute. It is obvious that the gains from parallel excitation would be severely compromised as the sensitivity mapping and pulse computation takes longer.

Second, early parallel excitation pulse design methods [1, 2, 33] focused on optimizing the pulses with a predetermined k-space trajectory, definitely leaving a room for further improvement in excitation accuracy. They only showed that undersampling k-space trajectory is possible but did not present a method to construct an optimized k-space trajectory. The inverse Fourier transform approach for the single coil excitation is not applicable to the parallel excitation because the final excitation pattern is not a direct Fourier transform of of a single RF pulse as we see in Eq.2.10. Recently, Zelinski et al. [16] proposed a method to determine the optimal k-space trajectory. The method is based on sparse approximation theory, and a generalized version of the previous method for single coil excitation [14]. This method is closely related to what we propose in this report, so the details would be covered in the next section.

Third, controlling both global and local RF power deposition is still a problem of large interest. Specific Absorption Rate(SAR) is the measure of how much energy is absorbed in a unit volume of the target object when a radio frequency electromagnetic

field is transmitted to it. There is a regulation on the maximum SAR allowed in MRI scanning, so it is essential for the RF pulse design method to produce pulses meeting the specified condition. [2] showed that extra degree of freedom given by the increased number of RF pulses can be used in the pulse optimization to reduce the total power deposited by the RF pulse. In [2], the average RF pulse power was modeled as $\mathbf{b}'\mathbf{F}\mathbf{b}$, where $\mathbf{b}$ is a column vector containing time samples of RF pulses and $\mathbf{F}$ is a matrix relating the RF pulse samples to the real electric field. It was reported that the RF pulse power was decreased by 38% compared to the optimization without power regularization. However, the method did not present a solution about how to control local SAR, for which object dependent factors should be considered. Imaging with high field MRI scanner that provides much improved SNR unfortunately suffers more from SAR because the RF power deposition tends to increase as the main field becomes stronger. To make the parallel excitation applicable in a more practical setting, a few solutions have been proposed to analyze and solve the SAR issue, but the problem still remains to be resolved.

In this thesis, our main focus is to solve the first and the second issue. Briefly speaking, our goal is to develop a fast iterative method to jointly optimize both RF pulse and linear gradient waveforms. To accelerate the RF pulse computation, we adopted the basis pulse approach initiated by [34]. To optimize the excitation k-space trajectory, we followed the sparse approximation theory with a discrete set of bases proposed by [14]. Their methods would be briefly reviewed in the next section.

2.3.4 Parallel excitation pulse design with slice selective bases for the echo-volumar trajectory

In the conventional iterative pulse design [10], the RF pulse waveform is decomposed into a train of time samples of a very short sampling interval, so it is not

unusual that the number of RF pulse samples to compute is in the order of thousands. For example, in GE 3T Signa Excite Scanner (GE Healthcare,Milwaukee, WI, USA), the time sampling interval of the RF pulse waveform is 1-4 us while many RF pulses may be longer than 5 ms. In [10], fast non-uniform FFT [36] was used to efficiently handle a large sized matrix-vector multiplication performed during the optimization, but the computation time still remained an issue in the parallel excitation due to the increased number of pulse parameters [13]. Also, spatial sampling of the desired excitation pattern increases the dimension of the problem particularly in the multi dimensional excitation. For example, for 3D spatial excitation, the excitation pattern should cover a broad range of the target object volume covered by the sensitivity of RF transmission coils. It is very obvious that the reduction of the problem dimension could decrease the complexity of the problem and the computation time would definitely benefit from it. Zhang et al. [34] proposed a solution to this problem by decomposing the RF pulse into a set of slice-selective basis pulses in conjunction with using an Echo-Volumar(EV) k-space trajectory [12].

The echo-volumar trajectory is composed of several kz-lines sampling kx-ky plane as in Figure 2.6. The sampling location of kx-ky plane is often called a phase encoding(PE) location or a spoke location. Fast oscillation along the kz axis allows achieving a rapidly changing excitation pattern along the z-axis while sampling kx-ky plane may produce a slowly varying pattern along the x-y plane. Therefore it is suitable in the application where the desired excitation pattern is in a thin slice with a smooth variation in the in-plane direction. The main idea in [34] was to deposit a single slice-selective pulse along each kz line and to determine the complex weight for each basis pulse. First of all, this approach reduced the problem dimension of the RF pulse parameters by two to three orders of magnitude, because the RF pulse

is now parameterized with a few complex weights instead of thousands of time samples. Also, a huge reduction in the dimension of the sampled excitation pattern was achieved because the slice-selectiveness of the basis pulse guaranteed slice-selection in the resulting excitation pattern, and thus spatial sampling outside the selected volume can be omitted.

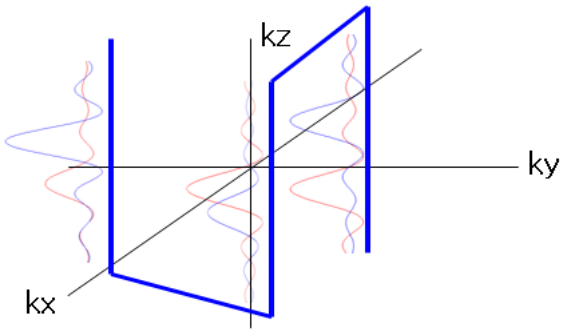

Figure 2.6: An example of Echo-Volumar k-space trajectory with slice-selective basis pulses. In the sample trajectory 3 kz lines are used while along each kz line, slice-selective sinc pulses are deposited to create a rectangular slice profile. Here a linear combination of shifted basis pulses are transmitted, but in [34] only one sinc pulse is transmitted along each kz line.

Suppose (kx_n, ky_n) is the n-th phase encoding location, and the EV trajectory has N phase encoding locations. Under the framework of using the EV trajectory and depositing a single slice selective basis pulse per each kz line, the small tip approximation equation for a single coil transmission disregarding T1,T2 relaxation and off-resonance can be rewritten as

$$\mathbf{M_{xy}}(\mathbf{r}) = i\gamma \mathbf{M_0}(\mathbf{r}) \int_0^T b(t) e^{i\mathbf{r}\cdot\mathbf{k}(t)} dt \tag{2.12}$$

$$= i\gamma \mathbf{M_0}(\mathbf{r}) \sum_{n=1}^{N} \int_{T_n}^{T_{n+1}} w(n) b_n(t) e^{i\mathbf{r}\cdot\mathbf{k}_n(t)} dt \tag{2.13}$$

$$= \mathbf{M_0}(\mathbf{r}) \sum_{n=1}^{N} w(n) e^{ixkx_n + iyky_n} \left(i\gamma \int_{T_n}^{T_{n+1}} b_n(t) e^{izkz_n(t)} dt \right) \tag{2.14}$$

$$= \mathbf{M_0}(\mathbf{r}) \sum_{n=1}^{N} w(n) e^{ixkx_n + iyky_n} p(z)$$

$$= \mathbf{M_0}(\mathbf{r}) p(z) \sum_{n=1}^{N} w(n) e^{ixkx_n + iyky_n}. \tag{2.15}$$

where T_n and T_{n+1} are the starting and the ending time of the n-th kz line, $b_n(t)$ is the basis pulse transmitted along the n-th kz line, $w(n)$ is the complex weight for $b_n(t)$, and $p(z)$ is the slice profile determined by the basis pulse. Eq.2.12 is decomposed into a sequential series of a time segment during which one kz line is traversed, yielding Eq.2.13. For each segment, the in-plane frequency(or the phase encoding location) is fixed, so they are pulled out of the integral and result in Eq.2.14. In Eq.2.14, the integral is basically one-dimensional Fourier transform of the basis pulse weighted by a scaler, $w(n)$. The integral term, $i\gamma \int_{T_n}^{T_{n+1}} b_n(t) e^{izkz_n(t)} dt$, reduces to $p(z)$ regardless of n, and thus the common slice profile is pulled out and finally we obtain Eq.2.15. Note that the summation is similar to 2D inverse Fourier transform. If the selected slice is thin enough to ignore the through-plane variation of the coil sensitivity, then the coil sensitivity $S(x, y, z)$ can be approximated as $S(x, y, z) \simeq S(x, y, z0) = S'(x, y)$ where $z0$ is the slice center. Then we can extend Eq.2.15 to the parallel excitation case as

$$\mathbf{M_{xy}}(x, y, z) = \mathbf{M_0}(\mathbf{x}, \mathbf{y}, \mathbf{z}) p(z) \sum_{l=1}^{L} S'_l(x, y) \sum_{n=1}^{N} w_l(n) e^{ixkx_n + iyky_n}, \tag{2.16}$$

where $S'_l(x, y)$ is the l-th coil's sensitivity and $w_l(n)$ is the weight of the n-th basis RF pulse transmitted from the l-th coil. This method was proposed to solve the B1 field inhomogeneity problem where the desired excitation pattern is a uniform thin slice. However, [34] did not provide a general strategy on how to optimize the phase encoding locations for a desired pattern with an arbitrary in-plane variation.

The optimization of PE locations in the EV k-space trajectory with parallel excitation was later presented by [16] based on the algorithm developed for the single coil excitation [14]. Suppose the desired excitation pattern $\mathbf{d}$ is a 3D thin volume expressed as $p(z)d_{in}(x, y)$ where $p(z)$ defines a slice profile along slice-select direction, and $d_{in}(x, y)$ defines the in-plane excitation profile. For example, in typical slice-selective excitation, $p(z)$ is a rect function and $d_{in}(x, y)$ is 1 in the Region Of Interest(ROI) and don't care outside the ROI as in Figure. 2.7

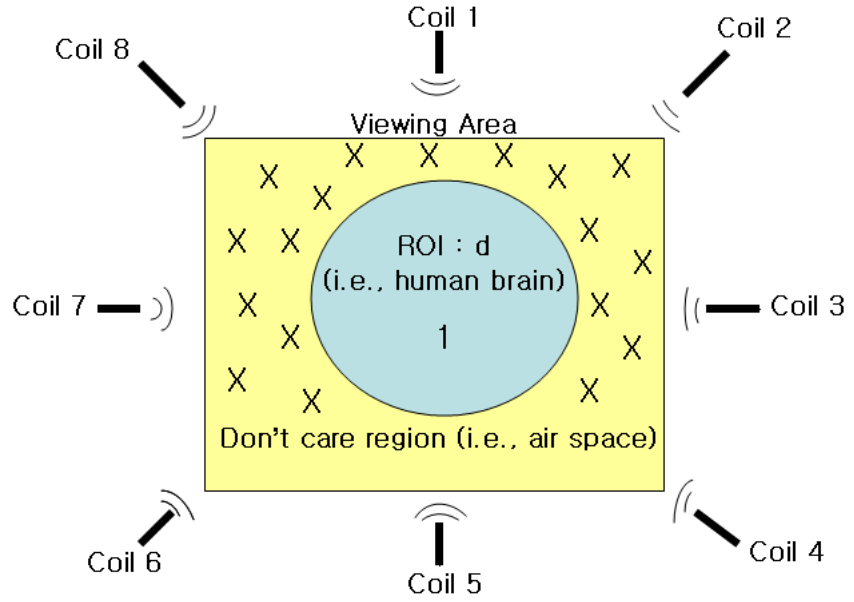

Figure 2.7: An example in-plane excitation pattern for a round-shaped object. There is no requirement for the excitation pattern outside the object support(ROI), so it's marked x meaning "Don't Care".

If the basis pulse is chosen to match the required slice profile, $p(z)$, the joint

optimization for both RF pulse weights and the PE locations can be formulated as

$$\begin{aligned}
&\min_{w_l(n),\, kx_n,\, ky_n} \|\mathbf{d} - p(z)\sum_{l=1}^{L} S'_l(x,y)\sum_{n=1}^{N} w_l(n)e^{ixkx_n+iyky_n}\|_2 \\
=&\min_{w_l(n),\, kx_n,\, ky_n} \|p(z)d_{in}(x,y) - p(z)\sum_{l=1}^{L} S'_l(x,y)\sum_{n=1}^{N} w_l(n)e^{ixkx_n+iyky_n}\|_2 \\
\equiv&\min_{w_l(n),\, kx_n,\, ky_n} \|d_{in}(x,y) - \sum_{l=1}^{L} S'_l(x,y)\sum_{n=1}^{N} w_l(n)e^{ixkx_n+iyky_n}\|_2
\end{aligned} \tag{2.17}$$

Because the cost function is not linear with respect to the phase encoding locations, performing continuous optimization on the phase encoding locations is a very tough problem as shown in [13]. One important conceptual contribution that [14] has made is to discretize the kx-ky space to form a set of candidate PE locations. The maximum frequency that a PE location may have can be limited by experimental results, so the number of candidates can be also limited accordingly. This process converts the continuous optimization of PE locations into optimal selection among a finite number of candidates. For example, in Eq.2.17, kx_n and ky_n belong to a infinite continuous set, $(-\infty, \infty)$, but in [14], (kx_n, ky_n) belong to $\{(kx, ky)|\, kx \in \{kx_1, kx_2, ..., kx_M\},\, ky \in \{ky_1, ky_2, .., ky_M\}\}$ where M is the number of candidates for kx and ky respectively.

In [14], they pointed out the length of the final RF pulse is dominated by the number of kz-lines, which is same as the number of phase encoding locations. Therefore, in the optimization of PE locations, it is also desirable to use as few PE locations as possible. In other words, N is a parameter to minimize in Eq.2.17 as well even though it does not appear explicitly. To enforce this constraint to use a minimal N, [14] proposed sparse selection of PE locations from the candidate PE locations as following.

Let's consider the single coil transmission case for simplicity. Suppose we used all the PE location candidates for Eq. 2.17 as following.

$$\min_{w(m,n),\, kx_n,\, ky_n} \|d_{in}(x,y) - \sum_{m=1}^{M}\sum_{n=1}^{M} w(m,n) e^{ixkx_m + iyky_n}\|_2 \tag{2.18}$$

In the minimization, we hope that the minimal number of phase encoding locations are used to approximate d_{in}. In terms of the pulse weights, $w(m,n)$, it means selected PE locations have non-zero weights while unselected have zero weights. This suggests that we can translate the condition whether one PE location is selected or not into the condition whether the associated pulse weight is zero or not. Furthermore, if the total number of PE location candidates, M^2, is far greater than the unknown, minimal number of phase encoding locations, enforcing sparsity on the $w(m,n)$ in the above minimization can be used to encourage the minimal selection of PE locations. Therefore the joint optimization of the RF pulse and the k-space trajectory can be recast into the optimization of the RF pulse with a sparsity constraint. Based on Eq.2.17, the optimization can be represented in a matrix-vector form as

$$\min \|\mathbf{w}\|_0 \quad \text{subject to} \quad \|\mathbf{d} - \mathbf{F}\mathbf{w}\|_2 < \epsilon \tag{2.19}$$

where $\mathbf{d}$ is a vector composed of spatial samples of the in-plane excitation pattern over a uniform sampling grid, $\mathbf{w}$ is a vector containing the complex pulse weights, ϵ is an allowed maximum excitation error, and $\mathbf{F}$ is a 2D inverse Fourier transform matrix where each column of $\mathbf{F}$ represents a candidate PE location, $e^{ixkx+iyky}$. The l_0 norm is used to measure the sparsity, the number of non-zero entries in the vector containing the pulse weights, and the minimization was subject to the condition that the excited pattern should accurately approximate the desired pattern. This type of

optimization is so called a sparse approximation problem in mathematics because it can be interpreted as approximating $\mathbf{d}$ with a sparse linear combination of columns of $\mathbf{A}$. Because $\mathbf{A}$ provides a collection of basis, it is often called a *dictionary matrix*. Basis pursuit [15] is a well know numerical approach for solving sparse approximation by substituting l_1 norm for l_0 norm, and was applied in [14]. Particularly in [14], the optimization with l_1 norm was later rewritten as a Second Order Cone Program(SOCP), which is a convex optimization for which many numerical solution packages are available.

However, for the parallel excitation, the sparsity should be jointly enforced between the pulses transmitted at the same phase encoding location. For example, if one phase encoding location is selected, it does not matter how many coils transmit a pulse for that phase encoding location whereas for an unselected phase encoding location, no coil can transmit a pulse for it. Therefore it was necessary to combine the pulse weights associated with the same phase encoding location to jointly enforce sparsity on them. For that purpose, [16] introduced a new vector, $\mathbf{p}_i$, composed of pulse weights that are from different coils but are associated with a common phase encoding location. For example, $\mathbf{p}_i = [\mathbf{b}_1(i), \mathbf{b}_2(i), \mathbf{b}_3(i), , \mathbf{b}_L(i)]$ where $\mathbf{b}_k(i)$ indicates the RF pulse weight from the k-th coil for the i-th candidate phase encoding location, and L is the number of coils. Then the minimization in Eq.2.19 is extended as following.

$$\min \|Z\|_0 \quad \text{subject to} \quad \|\mathbf{d} - \sum_{l=1}^{L} \mathbf{S}_l \mathbf{A} \mathbf{w}_l\|_2 < \epsilon \tag{2.20}$$

where $Z = [\|\mathbf{p}_1\|_\infty, \|\mathbf{p}_2\|_\infty, , \|\mathbf{p}_N\|_\infty]$, $\mathbf{S}_l$ is the l-th coil's sensitivity matrix, N is the number of candidate phase encoding locations, and w_l is a vector containing the l-th coil's basis pulse weights. However, both l_0 norm and l_∞ norm is very hard to handle

in numerical optimization, so they replaced l_∞ norm with l_2 norm and l_0 norm with l_1 norm. After replacing norms, the problem was again recast as SOCP, and solved using a numerical solution package, SeDuMi[http://sedumi.ie.lehigh.edu/].

Once phase-encoding locations are selected, the basis pulse weights were computed with a cost function modified to consider power regularization and B0 field inhomogeneity as in Eq.2.11. Here, reformulation of optimizing PE locations into a sparse approximation made a great conceptual improvement because it provided a new framework to formulate the problem and guide the direction for the optimization. However, this convex optimization using l_1 norm to enforce sparsity suffered from long computation time as many of optimizations using l_1 norm, which is a very critical disadvantage in the pulse design. We implemented their method, and observed that for an 8 coil excitation, it took 48 minutes to finish the pulse computation, which is obviously too long to be applied to practical scanning. Another issue with this convex optimization method is that it can not include off-resonance effects during excitation that distorts the linear phase induced by each PE location. If off-resonance frequency is considerable, ignoring such phase distortion can significantly downgrade the effectiveness of the chosen PE location, lowering the excitation accuracy unexpectedly. We developed a new fast algorithm considering off-resonance effects during PE location selection to choose more effective PE locations than the convex optimization approach in much less computation time. We developed a greedy algorithm based on Simultaneous Orthogonal Matching Pursuit [37] to accelerate the optimal PE selection process, and their applications are presented in chapter IV and V.

CHAPTER III

Spatially Selective PCASL with Parallel Excitation

This chapter is based on the abstract[38] presented in International Society for Magnetic Resonance in Medicine 19th annual meeting in 2011.

3.1 Introduction

Arterial Spin Labeling(ASL) [39] has become a popular tool for MR perfusion imaging by using blood water as a tracer, avoiding the administration of any exogenous contrast agents. While the original ASL technique consists of tagging all the blood spins entering the brain, several vessel-selective ASL(VSASL) schemes [40, 41, 42, 43] have been introduced to tag blood spins of selected vessels only. Their goal is to map the perfusion territories of specific vessels in the brain to detect abnormality in the vascular structure or to guide a surgical plan [44, 45, 46, 47, 48].

Recently, a few VSASL approaches [49, 50, 51, 52] based on Pseudo-Continuous Arterial Spin Labeling (PCASL) [53] have been proposed. They inherit the advantages of PCASL such as overcoming limitations imposed by magnetization transfer and excessive power deposition. In [49, 50, 51], they aimed to invert spins only on the selected vessels by inserting in-plane directional gradient pulses between individual tagging pulses. For their tagging sequence, they aimed to design in-plane gradient pulses such that the magnetization phase shift from the RF phase on the unselected

vessels is alternating between 0 and π while the magnetization phase on the selected vessels is coherent with the RF phase. Then, the blood spins on the unselected vessels essentially experience a control sequence instead of a tagging sequence such that their inversion is suppressed. On the other hand, the blood spins on the selected vessels are inverted as a conventional PCASL tagging sequence.

However, the applicability of these methods for tagging multiple vessels is strongly restricted by their geometry because of the dependence upon the linear gradient for vessel selectivity. To achieve the desired selectivity, the gradient-induced phase of the magnetization at the location of the selected vessels should be the same, while the phase-gain at the unselected vessel locations should be close to π radians relative to the selected vessels [49]. This can be easily achieved if the vessels are collinear (e.g. at neck area) but not otherwise (e.g. the cerebral arteries above the circle of Willis). In case of non- collinear vessel geometry, the tagging efficiency of these methods can be severely damaged.

We propose a novel PCASL scheme that uses parallel excitation to tag selected vessels. In parallel excitation, the pulses transmitted from each coil are weighted by the transmission sensitivity of the associated coil, creating a spatially varying RF field. We design RF pulses such that their superposition forms a train of pulses that achieve pseudo-continuous inversion only at locations of selected vessels. Our new technique maintains high inversion efficiency and superior spatial selectivity, and is less restricted by the geometry of the vessels than the conventional methods. At the time of this writing parallel excitation is not widely available, so our scope is limited to providing computer simulation results illustrating the effectiveness of parallel excitation for VSASL. Since the simulation was conducted for 3T, the change of B1 field map by loading a real object should be modest, and our simulation can

represent a realistic case.

3.2 Methods

3.2.1 RF pulse design outline

Our goal is to compute the RF pulses for each coil such that the sum of RF fields from all coils can produce a pseudo-continuous inversion [53] only at the selected vessels while the net RF field on the unselected vessel is close to zero, inverting no spins at both tagging and control sequence. In our pulse sequence, each coil transmits a train of Hanning pulses, which we weight by an independently controlled complex scalar. We optimize the scalar weight for each coil to have desired constructive or destructive summation of RF pulses at the vessels of interest. Note that static tissue locations can be ignored in the optimization, thus relaxing the problems constraints. For the control pulses needed for ASL, we use the same weights, but we alternate their signs between each pulse such that no inversion occurs, but the same amount of magnetization transfer (MT) is introduced.

3.2.2 RF pulse computation

Consider a PCASL tagging pulse train of unit RF pulses transmitted by multiple independent coils. The n-th unit pulse transmitted from the r-th coil can be described as follows.

$$b_r^n(x, y, t) = w_r s_r(x, y) h(t) \tag{3.1}$$

(x, y) indicates a 2D spatial coordinate, and $b_r^n(x, y, t)$ is the n-th RF pulse transmitted from the r-th coil observed at (x, y). $s_r(x, y)$ is the sensitivity of the r-th transmission coil at (x, y). $h(t)$ is the unit Hanning pulse in the pulse train as in [53]. We need to design w_r, the weight for the RF pulse transmitted from the r-th coil.

The net RF field observed at (x, y) consists of the superposition of all RF pulses across R coils as follows.

$$b^n_{net}(x, y, t) = \sum_{r=1}^{R} w_r s_r(x, y) h(t) = h(t) \sum_{r=1}^{R} w_r s_r(x, y) \tag{3.2}$$

Our goal is to find a set of the pulse weights, w_r that satisfy the following condition:

$$\sum_{r=1}^{R} w_r s_r(x, y) = \begin{cases} e^{i\theta(x,y)} \text{ for (x,y) in the selected vessel locations} \\ 0 \text{ for (x,y) in the unselected vessel locations} \\ \text{don't care otherwise} \end{cases} \tag{3.3}$$

$\theta(x, y)$ indicates the phase of the net RF pulse at (x, y), and it is a free parameter we may exploit to improve the optimality of the RF pulses. For example, relaxing the desired RF phase pattern has been investigated to improve the excitation accuracy [54]. In all of our simulation experiment, we observed smooth variation in $\theta(x, y)$ usually yielded a reasonably good result. Therefore, we fixed $\theta(x, y) = 1$ for all (x, y) of interest throughout the experiments . Using the above conditions, we formed the following minimization problem to determine our pulses.

$$\min_{w_r} \sum_{(x,y)\in I} \eta_{(x,y)} |d(x, y) - \sum_{r=1}^{R} w_r s_r(x, y)|^2 + \sum_{r=1}^{R} \lambda_r |w_r|^2 \tag{3.4}$$

Here, $d(x, y)$ is set as 1 or 0 according to Equation 3.3. $\eta(x, y)$ and λ_r are design parameters to balance the inversion efficiency and the pulse power deposition. For example, $\eta(x, y)$ helps suppress the excitation error at (x, y) described by the terms in the first summation in Equation 3.4. λ_r penalizes a large pulse weight for the r-th coil to control its peak RF pulse amplitude and the integrated pulse power [10]. I is a set of spatial coordinates for vessels of interest. We designed an RF pulse and measured its power as the norm of the pulse weight vector, namely, $\sqrt{\sum_{r=1}^{R} |w_r|^2}$. In

RF pulse computation, we tried different λ values to determine the RF pulse which achieves 99% accuracy with minimum power. For simplicity, all λ_r values were set to be equal to each other.

3.2.3 Simulation outline

We used Bloch equations to simulate the MR signals produced by our method and compared it to the conventional method [49] for multiple vessel selection. We conducted computer simulation studies using Matlab (MathWorks, Natick, MA) with a personal computer (Intel Q6600 CPU at 2.4 GHz and 4GB RAM). The sensitivity patterns of an 8 channel active rung transmit array [55] were obtained by Finite-Difference Time-Domain (FDTD) simulation at 3 Tesla [56]. In the FDTD simulation, we assumed a phantom of a 22cm diameter lossy cylinder with $\sigma = 0.3S/m$ and $\varepsilon_r = 80$. FOV of 24cm x 24cm over 64x64 sampling grid was used to obtain the initial transmission sensitivity patterns. Then it was interpolated to acquire a 192x192 sensitivity map shown in Figure 1. For the PCASL sequence, we used a 500 usec long Hanning pulse as a unit RF pulse denoted as $h(t)$ in Equation 3.1. The neighboring Hanning pulses were 1500 usec apart, and the amplitude of the slice-select gradient was 0.6 G/cm. The blood flow velocity is assumed to be 30cm/sec.

3.2.4 Simulation experiment

In [49], a scheme to tag multiple vessels with a Hadamard encoding pattern was proposed to improve SNR. However, the suggested encoding pattern is not always achievable as reported in [49, 50, 51], since it requires a phase shift between the selected vessels and unselected vessels with a linear gradient blip. To demonstrate that our method is less restricted by the vessel geometry than [49], we ran our method and [49] with a case where we have four non-collinear vessels. The experimented

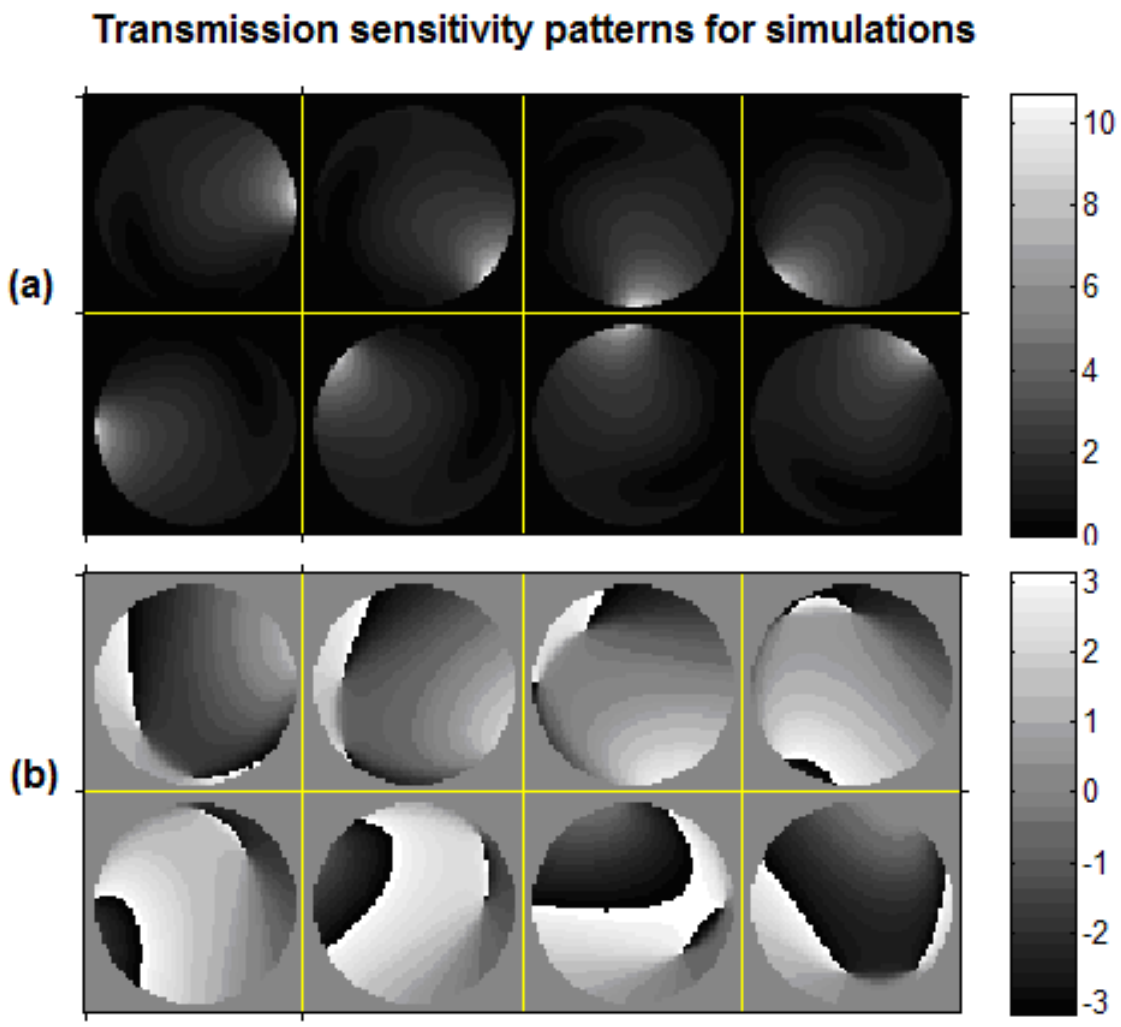

Figure 3.1: Magnitude(a) and phase(b) images of sensitivity patterns of 8 channel transmission coils used in simulation experiments. The unit of the phase is in radian.

vessel geometry is similar to the one presented in [50], as illustrated in Figure 3.2, and each vessel was set to occupy 3x3 voxels where each voxel size was 1.25mm x 1.25mm. We attempted to tag two vessels while not tagging the other two using two different excitation patterns, as shown in Figure 3.2 : pattern A tags the two vessels on the left side, and pattern B tags the two vessels on the top row. For the conventional method [49], we designed the in-plane gradient waveforms such that the π phase shift happens on the line which is parallel to the one connecting the selected vessels and pass the middle of the unselected vessels. We measured the inversion

efficiency for each vessel to evaluate our method compare it with [49].

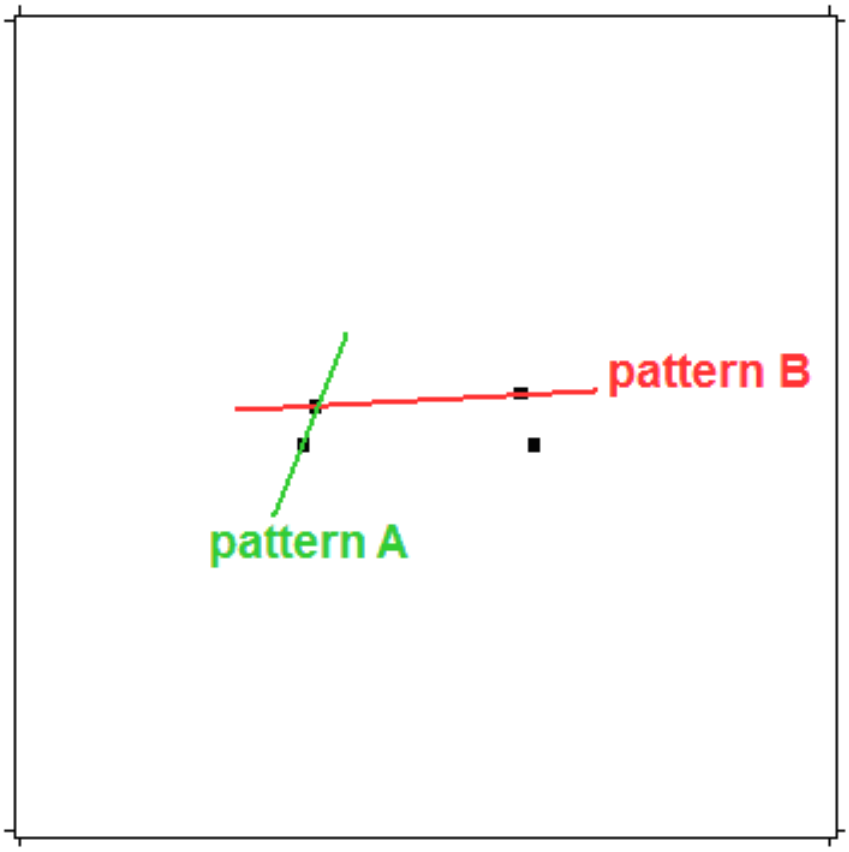

Figure 3.2: Locations of the vessels of interest for multiple vessel selection. Four vessels are placed in a geometry similar to the one experimented in [50]. Their geometry is not in a perfect rectangular shape such that the tagging scheme proposed in [49] is not ideal. Two experimented tagging patterns are shown above. In pattern A, we attempt to select the vessels on the left side (marked by the green vertical line), while the spins in other two vessels on the right are not inverted. In pattern B, we select the vessels on the top (marked by the red horizontal line) and do not perturb the spins in the two vessels on the bottom row.

3.3 Results

Figure 3.3 presents the average longitudinal magnetization (Mz) of spins in the vessels as they pass the tagging plane centered at z=0 cm for each method in the tagging sequence. The plot for the control sequence is not presented since the spin inversion was successfully suppressed with both methods. The blue line describes the trend of average Mz in the selected vessels whereas the red line does so for the

unselected vessels. In both selection pattern A and B, our method achieved the desired vessel selective tagging while effectively suppressing inversion for the control sequence. For example, the average inversion efficiencies for the selected vessels and the unselected vessels was about (83%, 0.5%) for the pattern A, and (83%, 4%) for the pattern B. However, the conventional method failed to obtain the desired vessel selectivity especially when the selected vessel was closely located to the unselected vessel (pattern B). For example, the average inversion efficiencies for the selected vessels and the unselected vessels was about (83%, 9%) for the pattern A, and (83%, 35%) for the pattern B. The inversion efficiency of the unselected vessels with the conventional method was about 8.8 times higher than that of our method.

Although the tagging results of our method were similar between the two selection patterns, the required powers were very different. We computed the normalized pulse power of the RF pulse for each pattern, $\frac{\sqrt{\sum_{r=1}^{R}|w_r|^2}}{\sqrt{\sum_{r=1}^{R}|w_r^{ref}|^2}}$, where w_r^{ref} is the pulse weight of a reference pulse tagging all the vessels. The reference pulse power here may be regarded as the RF pulse power deposited by the conventional method using parallel excitation. The normalized pulse power required for pattern A was 1.32. On the other hand, the normalized pulse power for pattern B was 5.67. In pattern A, the distance between the selected vessels and the unselected vessels is about 6 cm whereas it is 1.13 cm for the pattern B. Therefore, the excitation pattern defined in Equation 3.3 to implement pattern B required a rapid transition from 1 (selected vessel) to 0 (unselected vessel) than pattern A. Since the sensitivity maps of each RF transmission coil were smoother than the required excitation pattern, they had to be amplified such that the resulting excitation pattern formed by their weighted superposition could closely approximate the desired excitation profile.

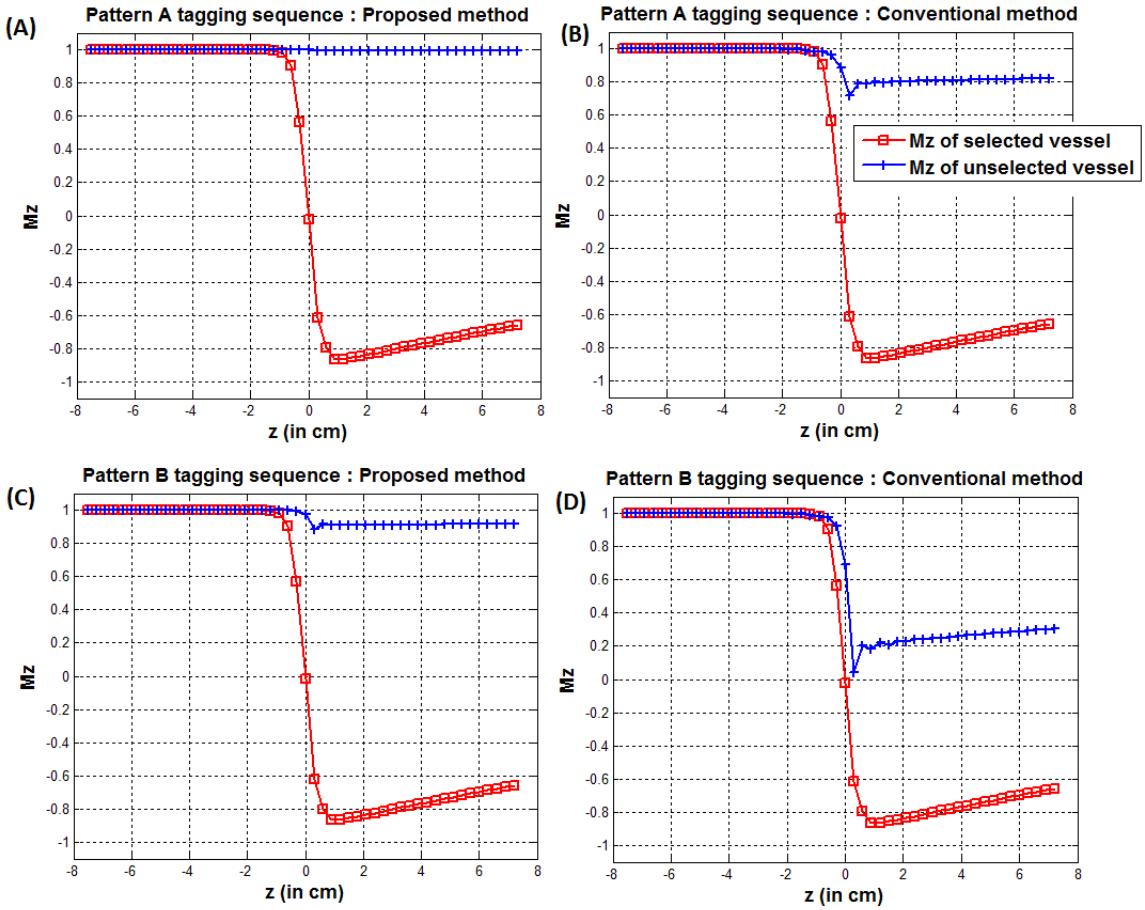

Figure 3.3: Tagging result for selecting vessels for the pattern A and the pattern B with different methods : (A) : tagging result for the pattern A with the proposed method, (B) : tagging result for the pattern A with the conventional method, (C) : tagging result for the pattern B with the proposed method, (D) : tagging result for the pattern B with the conventional method. The proposed method shows better vessel selectivity than the conventional method in both tagging patterns.

3.4 Discussion

In this report, we have proposed a novel vessel selective PCASL method using parallel excitation. Parallel excitation employs multiple RF transmission coils for which we can design and transmit independent RF pulses. The superposition of RF pulses weighted by the associated coils sensitivity forms the net RF field, which allows us to create a desired spatially varying RF field. We computed the complex scalar weight of the basis RF pulse in PCASL for each coil such that the resulting net RF

field closely approximates the desired excitation profile that achieves vessel selective tagging. In other words, we achieved the desired vessel selectivity by controlling the magnitude and phase of RF pulse applied on vessels of interest. A similar vessel selective tagging scheme was presented in [57] along with our own [38].

Previously developed methods achieved vessel selectivity by manipulating the phase coherence between the excited spins and the RF pulse by inserting gradient blips in the tagging pulse train. This limits the applicable geometry of the vessels since the phase induced from the linear gradients may not create desired spin phase patterns. For example, in the non-collinear vessel geometry introduced in Figure 3.2, the conventional method failed to accurately achieve the desired Hadamard encoding pattern. This suggests that when we separate the individual perfusion contribution for each vessel later, we may expect increased SNR with our approach by more accurate implementation of the Hadamard encoding pattern.

One potential drawback of our scheme may be the power deposition. If the desired excitation pattern has a sharp transition either by phase or magnitude change, it typically requires higher pulse amplitudes, aggravating the SAR issue. We may remedy this problem by relaxing the suppression condition of the unselected vessels. For example, it may be possible to allow a little excitation on the unselected vessels but to prevent the spins from becoming fully inverted by randomizing the RF pulse phases in the tagging sequence. In that case, we may relax the desired excitation pattern to be smoother. Another potential problem is the MT effect for the multiple vessel selection case. A different set of RF pulses are computed to obtain a different vessel selection pattern, so there is a chance that they may have different MT effects. In that case, there may not be a common control tagging sequence compensating the MT effect for all tagging patterns. In the worst case, a common MT effect can not

be assumed such that we need to run a separate control sequence for each selection pattern. However, this problem is totally dependent upon the RF transmission coil property and the hardware system setup. [43] presented a hardware configuration that employs a surface coil for tagging, and another coil for imaging a brain. In that case, localized sensitivity of the tagging coil caused no MT effect. Therefore, it may be possible to remove the MT effect issues above with using a parallel excitation coil with limited sensitivity only for the tagging purpose.

We note that in our simulations, we assumed that B0 field is homogeneous at the tagging plane, but in practice, it may not be so. This results in unwanted phase accumulation during the pseudo-continuous pulses and loss of efficiency, as reported in [58]. Given that parallel excitation allows us to control the phase pattern within the excitation plane, this method can be easily adapted to recover efficiency loss due to local B0 field inhomogeneity.

3.5 Conclusion

In conclusion, we presented the theoretical foundation and simulations in support of a novel approach using parallel excitation to perform spatially selective spin labeling. We demonstrated that our method can provide highly selective spin labeling with a wider range of vessel geometry than conventional methods. At the time of this writing, parallel excitation is not widely available, but there is great interest among the MR community in the development of this technology. Vessel selective ASL can thus provide one more exciting application motivating for the development of parallel excitation hardware. In future work, as the hardware becomes available, we plan to conduct in-vivo experiments to verify our method.

CHAPTER IV

Fast joint design method for parallel excitation RF pulse and gradient waveforms considering off-resonance

This chapter is based on the journal paper published in magnetic resonance in medicine [59].

4.1 Introduction

Trains of slice-selective pulses are useful for designing slice-selective parallel excitation RF pulses [12, 34]. This approach has been successfully applied to B1 field inhomogeneity correction [14, 16, 60], signal recovery for BOLD fMRI [28, 29, 61], spatial-spectral excitation [25], and large tip-angle multidimensional excitation [62, 63]. In this framework, each RF coil transmits a train of weighted slice-selective pulses interleaved by in-plane gradient blips to achieve a required in-plane excitation profile as shown in Figure 4.1. Determining the RF pulse requires computing only one scalar weight per slice-selective pulse for each transmission coil. Therefore, it significantly reduces the number of unknown RF parameters compared to conventional tailored RF pulse designs [10, 33] where the RF pulse is sampled finely in time (a few usec), yielding thousands of RF pulse samples to compute.

In the above pulse design approach, one must jointly compute the best pulse weights and in-plane gradient waveforms. The cost function for optimization often

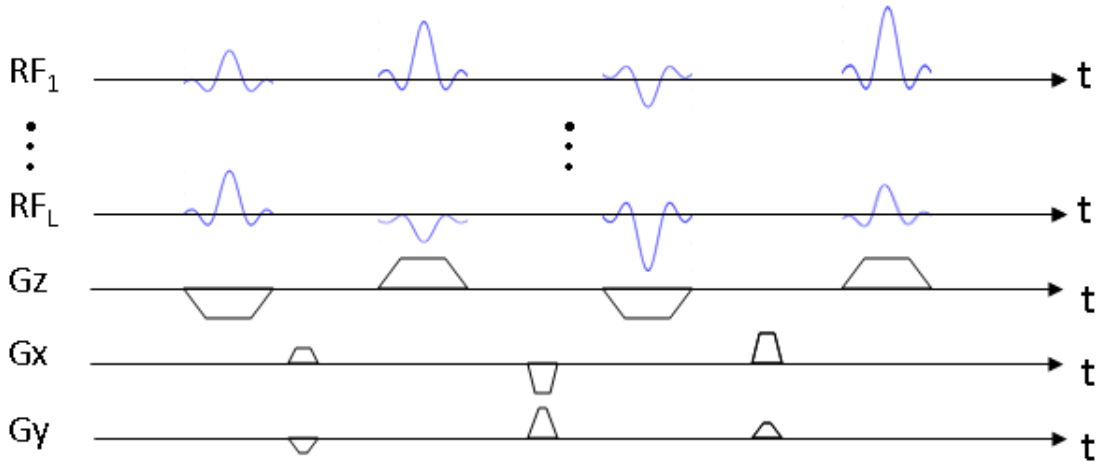

Figure 4.1: An example RF pulse sequence composed of trains of slice-selective RF pulses interleaved by in-plane gradient blips (Gx, Gy). This sequence is capable of exciting a thin slice with in-plane variation. In this chapter, we propose a fast joint design method to optimize the RF pulse weights and in-plane gradient blips for this sequence.

employs the excitation k-space analysis for the small tip-angle domain [6], where in-plane gradient waveform optimization becomes equivalent to optimizing Phase Encoding (PE) locations (also denoted as spokes) of an Echo-Volumar (EV) trajectory in excitation k-space [12]. Since the number of PE locations equals the number of slice-selective pulses in the resulting pulse train, sparse selection is crucial to limit the final RF pulse length. Recently, [14, 16] presented a convex optimization approach adopting an l1-norm based penalty to enforce sparsity of the selected PE locations. However, this method can be slow, so other schemes have been developed to accelerate PE location selection. For example, iterative greedy approaches [60, 64, 65] based on orthogonal matching pursuit [66] or sequential selection [67] achieved excitation accuracy similar to the convex optimization scheme with much less computation.

However, none of the aforementioned methods implemented PE location selection and ordering process considering off-resonance effects. In [60], a model considering off-resonance was suggested, but detailed implementation results were not provided.

In this chapter, we show via computer simulation that considering off-resonance when selecting PE locations can improve excitation accuracy. We demonstrate that heuristics for ordering PE locations, such as shortest-path [16, 60] or spiral-in [11, 28], can be quite suboptimal in some cases. We describe a novel greedy algorithm for determining PE locations that considers B0 field inhomogeneity during PE location selection. Our algorithm is a fast greedy selection process based on [65] that chooses PE locations sequentially in a time-reversed order, which naturally yields an effective ordering of the selected PE locations. In our PE location selection process, the basis signal associated with each PE location is modulated by the off-resonance phase accrual, allowing more accurate modeling than previous greedy methods [60, 64, 65]. Computer simulations show that our method achieves higher excitation accuracy than conventional methods in significantly less computation time. At the time of preparing this work, our parallel transmission hardware was not stable enough to run our pulse design, so our scope is limited to providing simulation data. At 3T where our simulation experiments are proposed, the shape of the B1 fields should not vary by large amount with different coil loading, so we believe that our results illustrate the potential benefits of our proposed algorithm.

4.2 Theory

4.2.1 Optimization formulation

We assume a small-tip angle RF pulse sequence where the RF pulse train is composed of M slice-selective RF pulses from L transmission coils. The mth slice selective pulse from the lth coil is a slice-selective basis pulse weighted by a complex scalar, $\alpha_l(m)$, that we determine through optimization. Using the excitation k-space analysis for a small-tip angle domain [6], we approximate the final excitation pattern

as follows:

$$(4.1)\quad d(x,y,z) \approx b(z)\sum_{l=1}^{L}\sum_{m=1}^{M} s_l(x,y)\alpha_l(m)e^{i2\pi(xk_x(m)+yk_y(m))}e^{i2\pi\Delta\omega(x,y)(t_m-T)}$$

Here, the excited pattern has a separable form. The through-plane excitation profile is $b(z)$ from the slice-selective basis pulse and the in-plane profile is determined by the terms in the double summation. $\Delta\omega(x,y)$ is the B0 fieldmap, t_m is the time corresponding to the middle of the m-th slice-selective pulse, and T is the end time of the RF pulse sequence. $(k_x(m), k_y(m))$ is the m-th PE location in the EV trajectory obtained by running time-reversed integral of the in-plane gradient waveforms. For optimization, we first design the PE locations and then derive corresponding gradient waveforms considering the hardware limitations. We assumed that the slice-profile is thin enough that the lth transmission coils sensitivity, $s_l(x,y)$, can be approximated as a 2D pattern (disregarding its through-plane variation). Note that a similar model was suggested in the Appendix of [60] without presenting implementation results.

The goal of our proposed RF pulse design algorithm is to jointly optimize RF pulse weights and PE locations to achieve a desired in-plane excitation pattern, $\theta(x,y)$. The cost function for our optimization problem is described as a following matrix-vector form:

$$\begin{aligned}&\min_{\alpha_l(m),\mathbf{f}_m} \|\boldsymbol{\theta} - \sum_{l=1}^{L}\sum_{m=1}^{M}\mathbf{S}_l\mathbf{W}_m\mathbf{f}_m\alpha_l(m)\|_2^2\\ &\equiv \min_{\boldsymbol{\alpha},\mathbf{f}_m} \|\boldsymbol{\theta} - \mathbf{A}\boldsymbol{\alpha}\|_2^2\end{aligned}\quad (4.2)$$

where $\mathbf{A} = [\mathbf{S}_1\mathbf{W}_1\mathbf{f}_1, ..., \mathbf{S}_L\mathbf{W}_1\mathbf{f}_1, \mathbf{S}_1\mathbf{W}_2\mathbf{f}_2, ..., \mathbf{S}_L\mathbf{W}_M\mathbf{f}_M]$, and $\boldsymbol{\alpha} = [\alpha_1(1), ..., \alpha_L(M)]^T$

$\boldsymbol{\theta}$ is a column vector containing the spatial samples of $\theta(x,y)$, $\mathbf{S}_l$ is a diagonal matrix of spatial samples of the lth coils sensitivity, $s_l(x,y)$, $\mathbf{W}_m$ is a diagonal matrix of spatial samples of the off-resonance phase, $e^{i2\pi\Delta\omega(x,y)(t_m-T)}$, and $\mathbf{f}_m$ is a column

vector of spatial samples of a 2D complex exponential, $e^{i2\pi(xk_x(m)+yk_y(m))}$. In this minimization problem, we attempt to choose optimal PE locations from a set of candidate PE locations formed by sampling 2D excitation k-space at Nyquist rate. The number of PE locations, M, should be limited to yield a RF pulse of reasonable length. For this purpose, we seek the minimum M having acceptable excitation accuracy. Therefore, M is not a prefixed parameter for the optimization though it does not explicitly appear in the optimization parameter set.

4.2.2 Optimization strategy

Our greedy algorithm is an iterative procedure where PE locations are selected in a time-reversed order. During the mth iteration, we select the mth from the last PE location. We use this order to determine the off-resonance phase accrual, $\Delta\omega(x, y, z)(t_m - T)$, without pre-specifying the number of selected PE locations, M, and the corresponding RF pulse train length, T. We increment the parameter M after each iteration in the optimization, so its final value is known only after the optimization is finished. However, the off-resonance phase accrual is well defined when we compute it in the time-reversed order regardless of M because $(t_m - T)$ becomes known instead. The reverse sequential selection also allows us to precisely control the trade-off between the number of selected PE location and the excitation accuracy.

Let E(N) denote the list of (ordered) PE locations, $\{(k_x(1), k_y(1)), (k_x(2), k_y(2)),$ ... , $(k_x(N), k_y(N))\}$, determined after N iterations in our algorithm. In the next iteration, we seek to choose from a discrete set of candidates the PE location that most reduces the cost function when added to the list E(N). The new PE location is added to the *front* of the list, yielding a new list E(N+1). For a given list of PE locations, E(N), we minimize the cost function in Equation 4.2 by performing the

orthogonal projection of the desired excitation pattern $\boldsymbol{\theta}$ onto the basis generated by the chosen PE locations, $\mathbf{S}_1\mathbf{W}_1\mathbf{f}_1, ..., \mathbf{S}_N\mathbf{W}_N\mathbf{f}_N$.

Whereas the method in [60] used orthogonal projection for every candidate, here we investigated a simple greedy method that uses significantly fewer orthogonal projections. In Equation 4.2, the in-plane variation of the excited pattern is synthesized linearly by the basis signals associated with the chosen PE locations. This implies that an effective candidate PE location has associated basis signals that are highly correlated with $\theta(x, y)$. With L transmission coils, selecting one frequency, $\mathbf{f}$ for the mth PE location produces L basis signals, $\mathbf{S}_1\mathbf{W}_m\mathbf{f}, , \mathbf{S}_L\mathbf{W}_m\mathbf{f}$. Inspired by the sum of correlations criterion presented in [37], we devised a cumulative correlation criterion to estimate how much one candidate PE location contributes to spanning the excitation pattern (or its projection residual after the first iteration). It is defined as a simple sum of squares of correlation values between the individual basis and the target pattern, $\mathbf{r}$, as follows :

$$\sum_{l=1}^{L} | < \mathbf{r}, \mathbf{S}_l\mathbf{W}_m\mathbf{f} > |^2. \tag{4.3}$$

We normalized each sensitivity pattern with respect to its $l2$ norm prior to computing the correlation to avoid any bias toward sensitivity patterns of higher norm. In using the cumulative correlation, we hope that the sensitivity patterns are reasonably localized such that they do not overlap too much. Then, summing the correlation with the basis signal for each coil can reasonably approximate the magnitude of the target pattern projected onto the range space of the basis signals. In the summation, we squared the absolute value of correlations, but other options may exist. For example, instead of using a sum of squares, a simple sum of absolute correlation values can be used. We experimented with different ways of summing, and the sum of the squares seemed to work as good as other options in most cases [65]. We compute this

cumulative correlation between each candidate and the projection residual from the previous iteration to cull only a few effective candidates for which we run orthogonal projections. The culling process greatly reduces the computation time spent in running orthogonal projections. To implement the orthogonal projection, we adopted the fast numerical scheme proposed in [60].

The details of our algorithm are presented in Table 4.1. At each iteration of our algorithm, the correlation test based on Equation 4.3 identifies p candidate PE locations that are added to a set of *effective* candidates denoted as C in Table 4.1. We select the design parameter p prior to the optimization; using a larger p may achieve better excitation accuracy at the expense of computation time. Before this addition, the set C already has p candidates retained from the previous iteration. For each of these $2p$ candidates in C, we run the orthogonal projection test by minimizing Equation 4.2. In other words, we compute the orthogonal projection of the desired excitation pattern onto the basis signals specified by the candidate and the previously established PE locations. We select the candidate PE location that best spans the desired excitation pattern and added it to the list of chosen PE locations. After that, we retain only the p candidates having the smallest projection errors and remove the rest from C. Selecting multiple candidates in the correlation test and passing some of them to the next iteration compensates for the imperfections in using the cumulative correlation as a measure of the effectiveness of one candidate for the subsequent orthogonal projection.

4.3 Methods

4.3.1 Test application description

We applied our algorithm to B1 field inhomogeneity correction [14, 16, 60]. The goal of the RF pulse design here is to compute an effective RF pulse that excites a

Problem Description
$\min_{\boldsymbol{\alpha},\mathbf{f}_m} \|\mathbf{r}\|_2^2$ where $\mathbf{r} = \boldsymbol{\theta} - \mathbf{A}\boldsymbol{\alpha}$, $\mathbf{A} = [\mathbf{S}_1\mathbf{W}_1\mathbf{f}_1, ..., \mathbf{S}_L\mathbf{W}_M\mathbf{f}_M]$, and $\boldsymbol{\alpha} = [\alpha_1(1), ..., \alpha_L(M)]^T$

Solution approach
No PE location is chosen initially. To try to minimize $\|\mathbf{r}\|$, the PE locations are chosen sequentially in a time-reversed order from a set of candidate PE locations.

Variable notation
For an ordered list of PE location, $E = (k_x(1), k_y(1)), (k_x(2), k_y(2)), ..., (k_x(N), k_y(N))$, a matrix $\mathbf{A}_E$ is defined as $\mathbf{A}_E = [\mathbf{S}_1\mathbf{W}_1\mathbf{f}_1, ..., \mathbf{S}_L\mathbf{W}_N\mathbf{f}_N]$ where $\mathbf{f}_n$ is a column vector of spatial samples of a 2D complex exponential, $e^{i2\pi(xk_x(n)+yk_y(n))}$). $\mathbf{S}$ and $\mathbf{W}$ are matrices containing the coil sensitivity and the off-resonance phase samples respectively as defined in Theory section.

Algorithm
Initialize the list of the chosen PE location, E, as an empty list.
Initialize the excitation residual, $\mathbf{r} = \boldsymbol{\theta}$, as the target in-plane excitation pattern.
Generate the set of all candidate PE locations, F, by sampling 2D k-space at Nyquist rate.
$\mathbf{f}_n$ vectors above will be instantiated from the candidate PE locations contained in F.
Initialize the set of culled candidate PE locations, C, as an empty set.
Initialize the reverse-order index of the PE location to select, m, as 1.

Loop until $\|\mathbf{r}\|$ is sufficiently small or the number of selected PE locations reaches a limit {
Step 1 : Cull effective PE locations from F, and add them to C.
Find p candidates in F having the highest correlation with $\mathbf{r}$ using Equation 4.3.
Add those p candidates to C.
Step 2 : Find the PE location in C that best reduces $\|\mathbf{r}\|$.
For each candidate in C, create a new list $\hat{E}$ by prepending it to E.
Compute the residual of orthogonal projection of $\boldsymbol{\theta}$ onto $\mathbf{A}_{\hat{E}}$, which is
$\boldsymbol{\theta} - \mathbf{A}_{\hat{E}}(\mathbf{A}_{\hat{E}}^h\mathbf{A}_{\hat{E}})^{-1}\mathbf{A}_{\hat{E}}^h\boldsymbol{\theta}$
Find the candidate with the minimum residual.
Step 3 : Set the PE location found in Step 2 as the m-th from the last PE location.
Add the candidate found in Step 2 to the front of E.
Step 4 : Update other parameters.
Pulse weights : $\boldsymbol{\alpha} = (\mathbf{A}_E^h\mathbf{A}_E)^{-1}\mathbf{A}_E^h\boldsymbol{\theta}$
$\mathbf{r} = \boldsymbol{\theta} - \mathbf{A}_E(\mathbf{A}_E^h\mathbf{A}_E)^{-1}\mathbf{A}_E^h\boldsymbol{\theta}$
m = m+1.
Discard PE locations in C except those with p smallest $\|\mathbf{r}\|$ values.
}
Our algorithm becomes equivalent to the modification of [60] if C is replaced with the set of entire candidates, F in Step 2.

Table 4.1: The detailed procedures of the proposed algorithm

uniform in-plane profile. The in-plane profile, θ, in Equation 4.2 is 1 in the excitation region of interest. In human brain scans, the air space outside the head corresponds to the dont care region, so the norm in Equation 4.2 is taken only within the head. For comparison with our proposed method, we implemented three other methods: the convex method [16], the greedy method [60], and the greedy method extended to consider off-resonance during PE location selection briefly suggested in [60]. Since the extension of [60] did not describe a specific ordering of the chosen PE locations, we implemented it with our sequential selection in a time-reversed order.

4.3.2 Assessment criteria

To investigate how much ordering can affect the excitation accuracy in the presence of high off-resonance, we first tried every possible ordering of selected PE locations from the convex method [16] and the greedy method [60] that employs a heuristic ordering scheme (shortest-path). We measured the Normalized Root Mean Squared Error (NRMSE) of the achieved in-plane excitation pattern. We compared these errors with those of our method and the aforementioned modification of [60]. Because the number of possible ordering is the factorial of the number of selected PE locations, we focused on the case that 5 PE locations are chosen. Also, we recorded the computation time of all methods to test whether they can satisfy practical on-line computation requirements.

4.3.3 Experiment parameters

We conducted simulation studies to compare aforementioned algorithms. They were implemented with Matlab (MathWorks, Natick, MA) on a computer with Intel Q6600 CPU at 2.4 GHz and 4GB RAM. The sensitivity patterns of an 8 channel active rung transmit array [55] were obtained by Finite-Difference Time-Domain

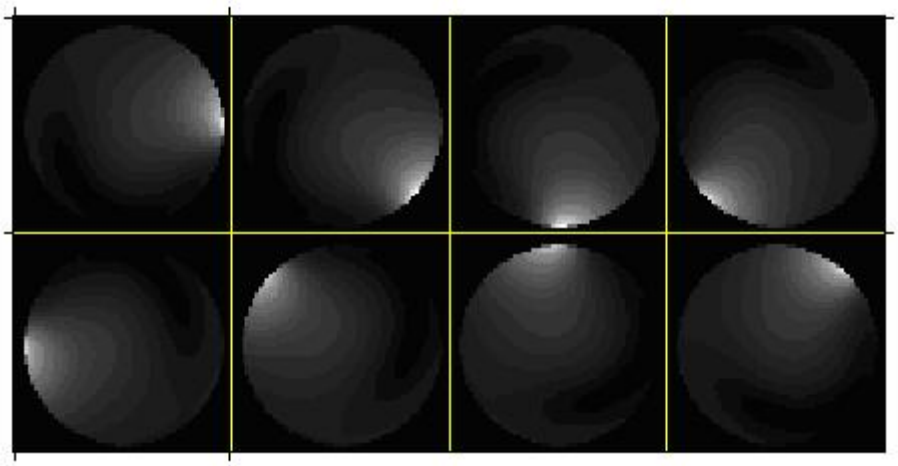

Figure 4.2: Magnitude images of sensitivity patterns of 8 channel transmission coils used in simulation experiments.

simulation [56] at 3 Tesla, where we assumed a phantom of a 22cm diameter lossy cylinder with $\sigma = 0.3$ S/m and $\varepsilon_r = 80$. Figure 4.2 shows the simulated transmission sensitivity patterns. The B0 fieldmap and the excitation ROI were acquired from in-vivo human brain scans for 2 subjects. We chose two 5mm thick axial slices of relatively high off-resonance for the RF pulse design. The excitation FOV was 24cm x 24cm with 64x64 uniform sampling grid specifying the desired excitation pattern. The candidate PE locations were formed by sampling the continuous in-plane frequency space at the Nyquist rate. For our proposed method, we used the full set of 64^2 candidates but only 19x19 low frequency candidates were used for the other methods as suggested in their original studies. The desired flip angle was 10 degree. A Hanning-windowed sinc pulse with one side lobe was used for the basis pulse, which was 0.75ms long due to the current gradient hardware limitations where the slew rate of the gradient was 150T/m/s and the maximum gradient amplitude was 4g/cm.

4.4 Results

4.4.1 Ordering of PE locations and excitation accuracy

Figure 4.3 illustrates the B0 fieldmaps and the excitation ROI of chosen brain slices. The air cavity regions in the slices caused high off-resonance frequencies ranging from -150Hz to 200Hz. Figure 4.4 plots the NRMSE of different PE location orderings for the convex method and for the greedy method along the associated EV trajectory length. The results from our method and the modification of [60] are marked as well. Note that our method and the modification of [60] do not use the same PE locations as the compared methods. Figure 4.4 demonstrates that our method and the modification of [60] generally have lower excitation error than any PE location ordering for the compared methods. There is no obvious relationship between the k-space trajectory length and the resulting excitation error. Even within the shortest orderings, there were considerable NRMSE variations in some cases. Also, connecting the PE locations in a spiral-in manner for the convex and the greedy method failed to achieve optimal excitation accuracy.

4.4.2 Uniformity of in-plane excitation profiles

To visually assess the uniformity of the excited in-plane profile, we ran the Bloch simulation of RF pulses computed for the slice 2, and plotted the resulting in-plane excitation patterns and the corresponding PE locations in Figure 4.5. To represent multiple shortest-path PE location orderings of the convex method and the greedy method, both the minimum NRMSE case and the maximum NRMSE case were displayed. The transverse magnetization profiles at the center of the slice (z=0) were simulated. To quantify the uniformity of the excitation profile, we calculated the mean and the standard deviation σ of the transverse magnetization magnitude

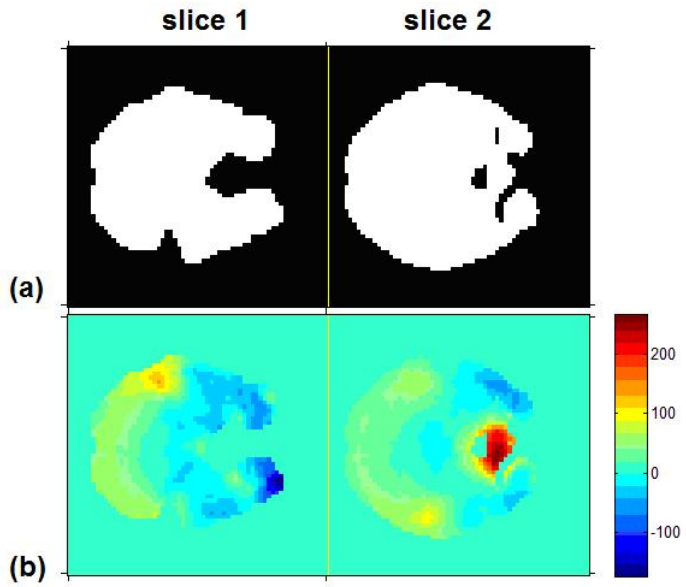

Figure 4.3: Excitation ROI (a) and B0 fieldmap (b) of 2 axial slices acquired from human scans. In the excitation ROI, the desired excitation pattern is set to be 1 in the white area, and dont care in the black area. The units of the fieldmap are Hz. The B0 fieldmaps shows very high off-resonance frequencies due to susceptibility difference around air cavity regions such as ear canals and a frontal sinus.

for each pulse design. The in-plane excitation patterns in Figure 4 show that our proposed method and the modification of [60] outperformed both the convex and the greedy method with respect to the uniformity. For example, σ of the minimum NRMSE case with convex method was the most uniform among the cases with the convex and the greedy method, but it was still 1.6 times larger than that of our method and the modification of [60]. The difference in the uniformity becomes even more dramatic when our method is compared to the maximum NRMSE case of the convex and the greedy method. In that case, their σs were 3 times and 2.6 times larger than that of our method respectively.

4.4.3 Computation time

Table 2 summarizes the computation time taken by each method for selecting PE locations. The convex optimization takes the longest time, as reported previously

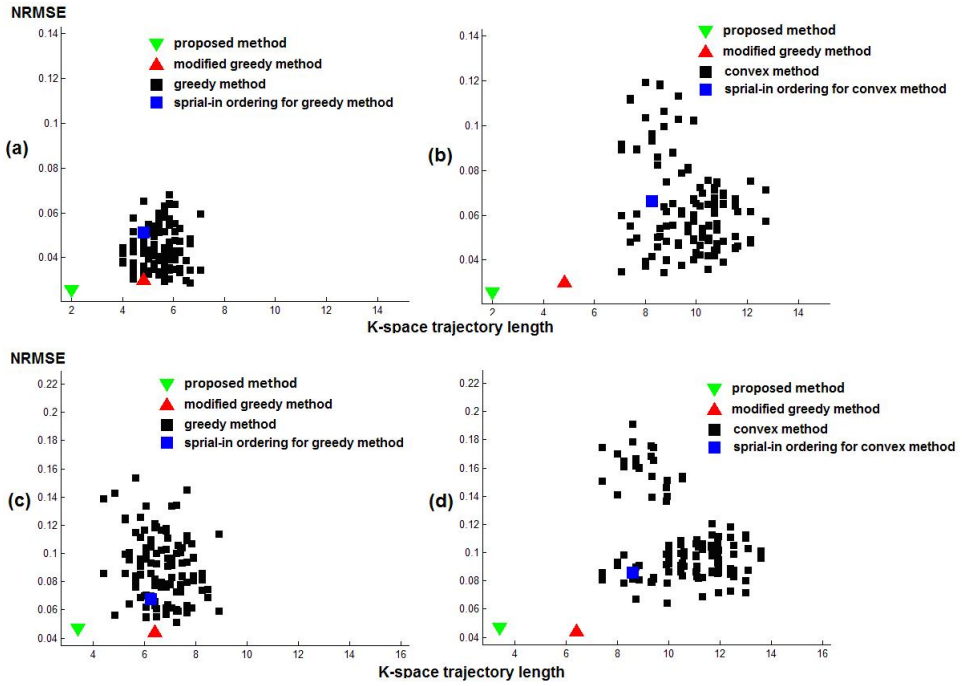

Figure 4.4: Scatter plots of NRMSE v.s. the length of EV k-space trajectory obtained with different PE location orderings. (a) and (c) are different orderings of PE locations with the greedy method applied for slice 1 and 2 respectively. (b) and (d) are with the convex method for slice 1 and 2 respectively. A black square mark indicates a PE ordering from the convex method or the greedy method. A Blue square mark is for the spiral-in ordering of PE locations obtained from the convex method or the greedy method. Conventional heuristic approaches to connect PE locations such as the shortest-path or the spiral-in did not show obvious optimal excitation accuracy. Our method and the modification of the greedy method consistently tend to show improved excitation accuracy than the compared conventional methods.

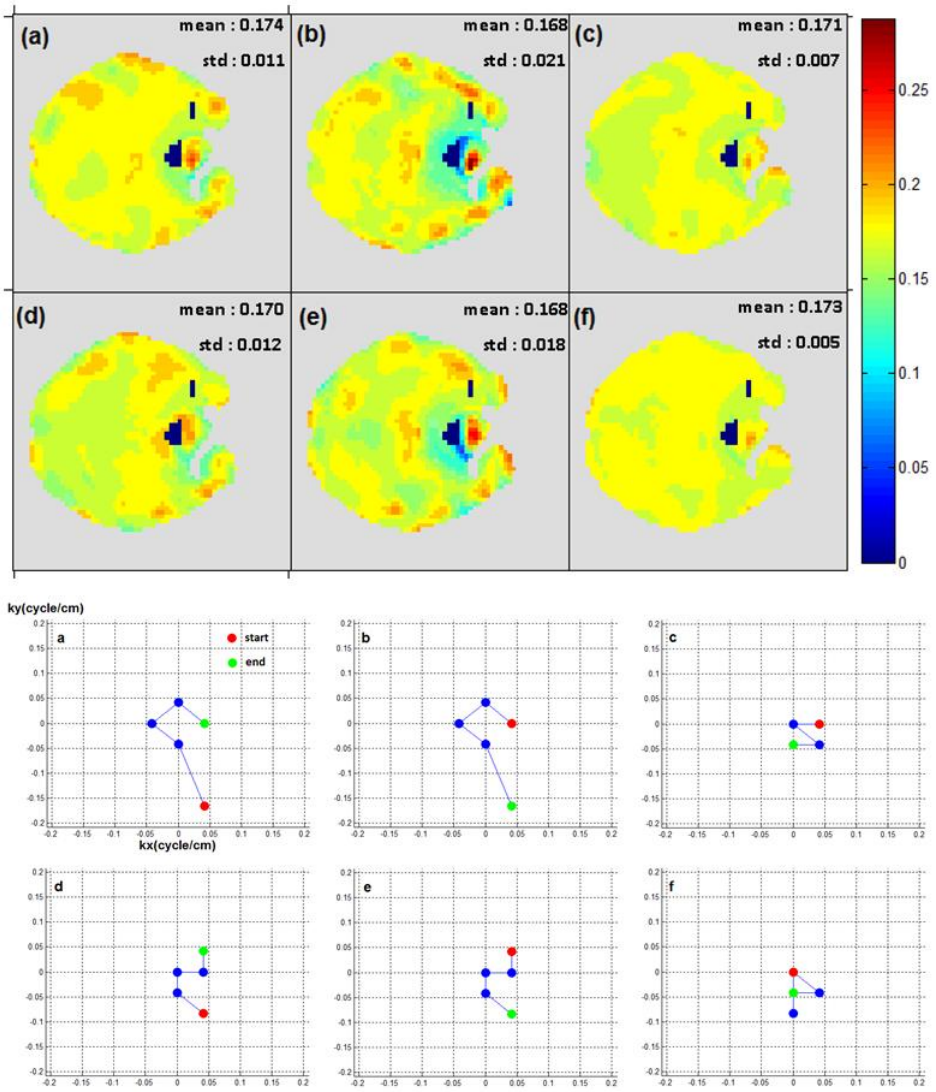

Figure 4.5: Uniformity of the in-plane excitation pattern simulated with different methods for slice 2. In-plane excitation profiles at z=0 and corresponding PE locations and their ordering. a) The minimum NRMSE case of the shortest-path ordering with the convex method, b) The maximum NRMSE case of the shortest-path ordering with the convex method, c) our proposed method, d) the minimum NRMSE case of the shortest-path ordering with the greedy method, e) the maximum NRMSE case of the shortest-path ordering with the greedy method, f) modification of the greedy method. Our proposed method and the modified greedy method show more uniform profiles than others.

[60, 64, 65]. The greedy method runs reasonably fast, but the proposed algorithm further accelerates the optimization by an order of magnitude. Note that we achieved this result while using an even larger set of candidates than the greedy method. For example, the set of candidates for our algorithm had 64^2 elements while the greedy method had 192, which is about a factor of 11 times fewer.

Slice	Convex method	Greedy method	Modified greedy method	Proposed method
1	1434.0 sec	5.7 sec	7.9 sec	0.9 sec
2	1729.4 sec	5.4 sec	5.3 sec	0.3 sec

Table 4.2: Computation time of different pulse design methods for each slice. We used each method to determine 5 PE locations to create a uniform excitation pattern for each slice. The computation time varies between different slices because depending on the size of the ROI, the number of spatial samples for the excitation pattern changes. Our method is by far the fastest method whereas the convex method is the slowest. The greedy method runs reasonably fast, but our method is still almost an order of magnitude faster.

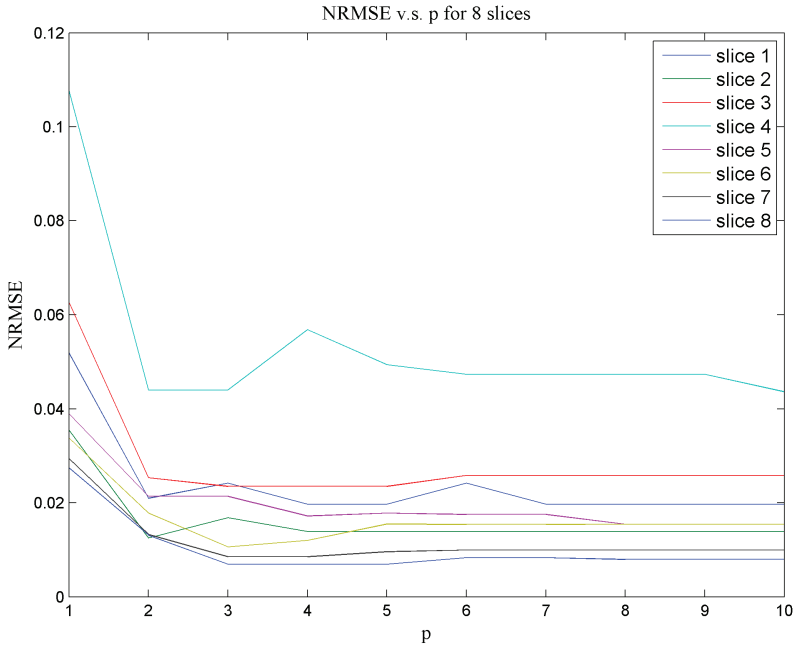

Figure 4.6: Normalized excitation errors that our pulse design achieved with different values of p for eight slices. Here, p indicates the number of candidates culled from the full set of candidates with the proposed cumulative correlation test. As the value of p grows, our method approaches to the greedy method sacrificing the computation time. The plot here shows an approximate L curve shaped form, suggesting that there may be an optimal point for p that has a good balance between computation time and excitation accuracy.

4.4.4 Speed vs. Accuracy tradeoff in our algorithm

The computation time of our algorithm depends on the choice of the parameter, p, the number of the PE location candidates selected by the cumulative correlation test. It determines the trade-off between the computation time and the excitation accuracy. Setting p to its largest value makes our method identical to the modification of the method by [60] and may yield higher excitation accuracy at the expense of computation time. However, we observed from experiments that increasing p above a certain threshold does not generally improve the excitation accuracy significantly. NRMSEs versus p for eight slices are plotted in Figure 4.6. A smaller p would reduce computation time but the curves show some oscillation for $p < 8$. We chose p conservatively ($p = 8$) to avoid exaggerating the computation acceleration of our method.

4.5 Discussion

In this chapter, we presented a fast greedy algorithm for parallel excitation RF pulse design to determine PE locations considering B0 field inhomogeneity. The original greedy method as implemented [60] and the convex optimization method [16] disregarded off-resonance in the model used for the PE location selection process, which raises two problems. First, it causes model mismatch, potentially selecting ineffective PE locations. In other words, the basis signals associated with the chosen PE locations may be less effective in approximating the desired excitation pattern accurately. Furthermore, it may exaggerate the predicted excitation accuracy estimated in the PE location selection stage, selecting too few PE locations. Secondly, it requires a heuristic to order the selected PE locations, which may lower excitation accuracy as illustrated in Figure 4.4. In contrast, our algorithm jointly determines

PE locations and their order by modeling the off-resonance effects during PE location selection, and achieved higher excitation accuracy than the conventional methods.

Our algorithm is also very computationally efficient. Both the greedy method [60] and our proposed method ran much faster than the convex method [16], but our method was almost an order of magnitude faster than the greedy method for comparable excitation accuracy. Instead of running orthogonal projections for every candidate PE location as in [60], we culled a few effective candidates with the cumulative correlation test, and performed the projection only for these candidates. This approach replaces numerous computationally demanding orthogonal projections with cumulative correlation tests, which are far less demanding because they use efficient operations such as FFT and diagonal matrix multiplications.

Our proposed algorithm is based on an iterative greedy selection procedure that may find a local minimum. The convex method can have an advantage over such greedy approaches from this perspective because it may have a wider search scope for optimal PE location combination. But the condition for finding the optimal solution is hard to meet and verify as pointed out in [60]. Also in the convex method, one can not control the computation time with respect to the number of selected PE locations because the termination of the optimization is not directly related to it. On the other hand, in our approach, we can simply terminate the optimization after the required number of PE locations is selected or the desired excitation accuracy is achieved. The convex method also requires a pruning technique to cull the specified number of PE locations from the solution. Typically, the locations with largest pulse weights are selected, but in parallel excitation, multiple pulse weights are associated with one PE location, therefore it is not so obvious how to sort them.

In Equation 4.1, the basis signal for the m-th PE location is modulated by the

off-resonance phase, $e^{i2\pi\Delta\omega(x,y)(t_m-T)}$. If the B0 fieldmap error is denoted as $\varphi(x,y)$, the actual phase modulation becomes $e^{i2\pi(\Delta\omega(x,y)+\varphi(x,y))(t_m-T)}$, whose first order approximation is $e^{i2\pi\Delta\omega(x,y)(t_m-T)}(1+i2\pi\varphi(x,y)(t_m-T))$. The term $2\pi\varphi(x,y)(t_m-T)$ gives the fractional error. For example, the error for the first PE location in a 5 msec pulse for a 5 Hz error is about 16%. The error is larger for PE locations visited earlier in the k-space. However, our greedy selection approach in a time-reversed order is likely to assign smaller pulse weights for the PE locations selected later (visited earlier in excitation k-space), and this may provide some robustness to B0 fieldmap errors.

Our cost function for PE location selection did not include a regularizer to control the pulse amplitude, so the pulse weights found during the PE location selection process may violate SAR constraints or the small-tip angle assumption. Our algorithm has not yet been validated with parallel transmit hardware, so it may need to be further limited by coupling between and changes to the B1 fields as well as restrictions on the peak RF amplitude. A future research topic is to develop methods considering these constraints in the PE location selection process. Also, we expect that greedy algorithms can be further improved by developing methods to refine previously selected PE locations, as suggested in [60] or [68].

4.6 Conclusion

We have introduced a fast greedy algorithm for determining effective PE locations and their order in the presence of B0 field inhomogeneity. Our proposed method achieved higher excitation accuracy and faster computation than previous methods. In future work, we plan to extend our method to more complicated applications such as signal recovery for BOLD fMRI [11, 28]. Also we will seek an efficient

way to incorporate a pulse power regularizer to consider the SAR issue during our optimization.

CHAPTER V

Signal Recovery for BOLD fMRI with Parallel Excitation

This chapter is based on the abstract [28] presented in International Society for Magnetic Resonance in Medicine workshop on parallel MRI in 2009

5.1 Introduction

T2* weighted imaging has been a dominant imaging technique in brain functional MRI for detecting functional activity. In T2* weighted imaging, the MR signal from a tissue is weighted by $e^{-\frac{TE}{T2*}}$, where TE is the echo time, and T2* indicates the signal decay rate of the tissue. In brain imaging, Ogawa et al [69] discovered that the T2* of a tissue is proportional to the blood oxygenation level. They suggested an application of T2* weighted imaging for tracking brain cell activity, for the activation status change of a cell may cause a change in the oxygen consumption and blood oxygenation level accordingly, leading to the contrast modulation in the T2* weighted MR image. Since then, T2* weighted imaging became the dominant brain functional MRI tool providing blood oxygenation level dependent (BOLD) contrast.

However, T2* weighted imaging has suffered from a serious signal loss problem around air cavity regions such as the frontal sinus and ears where brain tissues interface the air space. These two have a large magnetic susceptibility difference, causing the development of a rapid variation in the off-resonance frequency. Together with

a long echo time originally intended for building T2* based contrast, it gives rise to severe phase incoherence for magnetization within a voxel. The signal from a voxel is the sum of magnetization within the voxel, therefore the phase incoherence of magnetization results in signal loss. In the MR image, the signal loss artifact typically appears to be dark holes for the low signal amplitude as shown in Figure 5.1. Unfortunately, there are certain neuropsychiatric investigations that are considerably limited in fMRI because they need to study the brain activity around the regions suffering from this signal loss artifact. For example, obsessive compulsive disorder (OCD) and Tourette syndrome are mental disorders highly related with inferior frontal regions, signals from which are often impossible to detect with conventional T2* weighted imaging because of the extremely attenuated signal amplitude.

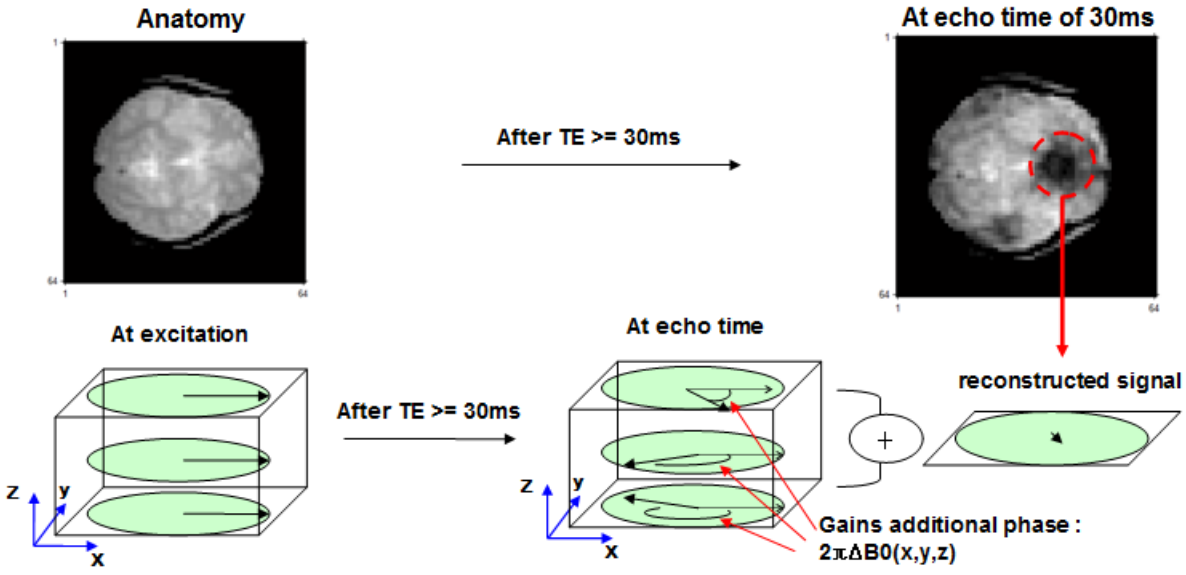

Figure 5.1: Signal loss in BOLD fMRI. The local through-plane gradient caused by air cavity brings about dephasing among the magnetizations, so the net magnetization in the unit volume decays quickly.

There have been many investigations attempting to solve the above signal loss issue. Direct off-resonance compensation with additional shimming hardware [70, 71, 72] may have the potential to achieve the ideal off-resonance correction performance,

but it required to place extra shimming hardware inside the subject's mouth, which was too uncomfortable for it to be practical. Various z-shimming approaches [73, 74, 75, 76] adopting z-shim gradient blips in EPI acquisition have been proposed to compensate for the through-plane local gradient. But with a limited number of z-gradient blips, they were not able to provide localized signal recovery, and often required multiple image acquisitions at the expense of temporal resolution. Slice-thickness reduction [77] may also provide reducing signal loss to some extent, but it increases the number of slices to cover a given volume, and thus impairs temporal resolution as well.

Signal loss correction with phase-precompensation using multi-dimensional RF excitation [11, 78, 79, 80] has a few advantages over the aforementioned approaches. This approach aims to excite the magnetization with a phase pattern that cancels the off-resonance induced phase at the echo time such that the magnetization is in phase along through-plane direction as shown in Figure 5.2. The idea of the phase-precompensation with RF excitation was proposed by [78, 79], and later implemented with a 3D tailored RF pulse design method with a stack of spiral k-space trajectory [80]. The 3D tailored RF pulse design was further improved with a more sophisticated spatial domain RF pulse design method adopting an echo volumar k-space trajectory [11]. In the 3D tailored RF pulse design methods, the desired excitation pattern is determined based on the measured B0 field map, so it can potentially achieve more localized signal recovery than previous methods. Also, the overhead of adding a multi-dimensional RF pulse to the pulse sequence is much less demanding than those methods requiring additional shimming hardware or multiple image acquisitions. However, the signal recovery performance of the 3D tailored RF pulse design with a single coil transmission was not sufficient enough for whole brain imaging because

it could not achieve the desired excitation pattern with high accuracy where off-resonance frequency is very rapidly varying. Also, the RF pulse calculation with the 3D tailored RF pulse design method was still computationally demanding, so it needs to be accelerated for routine fMRI studies.

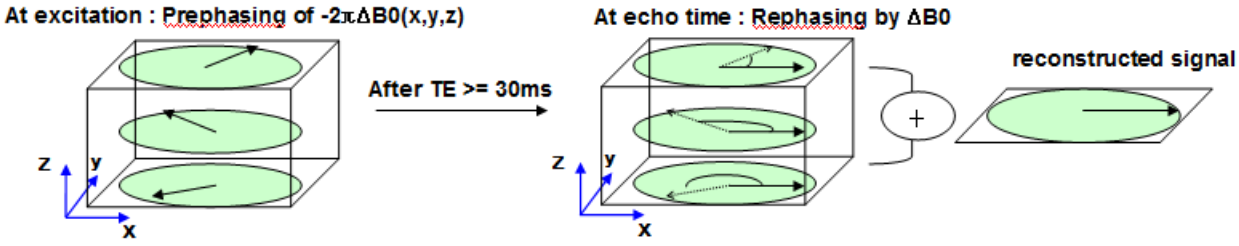

Figure 5.2: Signal recovery by exciting a pre-compensatory phase pattern. The phase of the excited pattern is designed to be in phase at echo time. The phase design is based on the measured fieldmap in a sub-voxel scale.

In this chapter, we introduce a novel, fast parallel excitation pulse design method combining a B1 field inhomogeneity correction[59] and a signal loss correction with time-shifted slice selective pulse design[29] to provide uniform signal recovery for T2* weighted imaging in BOLD fMRI. To achieve the desired excitation pattern, we transmit a linear combination of time-shifted(kz) slice-selective pulses together with phase-encoding in-plane (kx,ky) gradient waveforms to achieve uniform signal recovery over a specified region of interest. Adopting parallel excitation with multiple transmission coils with localized sensitivity, our method can tailor the excitation pattern more accurately to the off-resonance pattern than previous methods using single coil transmission [11, 78, 79, 80] and can thus obtain a better signal recovery performance. Also, our method provides a systematic scheme to compute the RF pulse and gradient waveforms based on B0 fieldmap(off-resonance frequency map) information , which can provide a more uniform signal recovery than [29] that needs manual selection for pulse weights by trial and error. We conducted computer simulations for parallel excitation to illustrate its potential effectiveness, and an in-vivo

experiment with a single coil transmission system to demonstrate the validity of our pulse design.

5.2 Theory

We assume a small tip-angle pulse sequence where a linear combination of time shifted slice-selective pulses forms a unit pulse segment of the pulse train, and in-plane gradient waveforms are transmitted between the unit pulse segments as shown in Fig 5.3. Such a sequence can create both in-plane and through-plane variations in the excitation pattern.

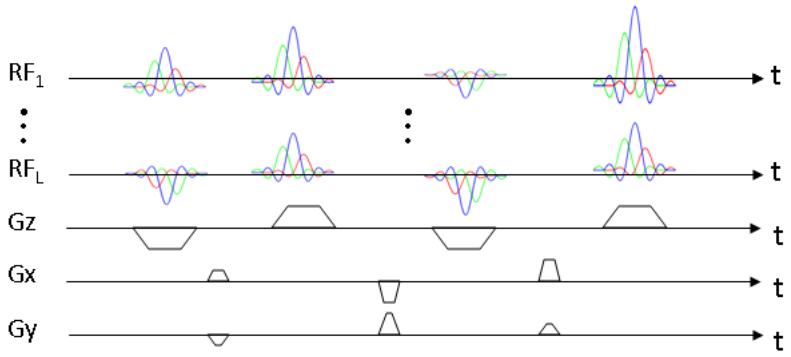

Figure 5.3: A pulse sequence composed of trains of time-shifted slice-selective pulses interleaved by in-plane gradient blips. This pulse sequence is capable of exciting a magnetization pattern with both in-plane and through-plane variation

5.2.1 Optimization formulation

We use the k-space analysis for a small-tip angle domain [6] to form the input-output relationship in our optimization as in Chapter IV. Now we consider a simple case where we shift in time a slice-selective pulse with respect to the slice-select gradient to develop a linear phase along the through-plane direction. We parameterize this effect in terms of the through-plane frequencies (k_z) and then later derive time-shifts from them for convenience. We form a set of N frequencies, $k_z(1), k_z(2), , k_z(N)$ by discretizing the continuous through-plane frequency space. If we deposit a linear

combination of time-shifted slice-selective pulses, each of which creates one of the above through-plane frequencies, then Equation 4.1 is modified as follows:

$$d(x,y,z) \approx b(z) \sum_{l=1}^{L} \sum_{m=1}^{M} \sum_{n=1}^{N} s_l(x,y)\alpha_l(m,n) e^{i2\pi(xk_x(m)+yk_y(m)+zk_z(n))} e^{i2\pi\Delta\omega(x,y,z)(t_m-T)} \tag{5.1}$$

In the above equation, each slice-selective pulse is weighted by a scalar, $\alpha(m,n)$, to be determined through optimization, where m and n index the PE locations and the through-plane frequencies. $\Delta\omega(x,y,z)$, t_m, T are the B0 fieldmap, the time corresponding to the middle of the m-th slice-selective pulse, and the end time of the RF pulse sequence, respectively. $b(z)$ is the through-plane profile of the basis pulse. In our problem, the desired excitation pattern is a thin-slice with pre-compensatory phase for off-resonance, which is modeled as $b(z)e^{i2\pi(\Delta\omega(x,y,z)\mathrm{TE}-\beta(x,y))}$. $\beta(x,y)$ is a in-plane phase relaxation term to subtract out a common phase variation from the desired phase pattern to smooth the in-plane phase of the desired pattern. $\Delta\omega(x,y,z)\mathrm{TE}$ typically shows a very rapid, local in-plane phase variation, which may require deposition of many PE locations as reported in [11]. Subtracting a common 2D phase pattern from each 2D subslice of $\Delta\omega(x,y,z)\mathrm{TE}$ does not change the phase coherence at echo time along the through-plane direction. Therefore, we can exploit it to smooth the in-plane variation of the desired excitation pattern in attempt to approximate it with fewer PE locations. This, in fact, greatly reduces the number of required PE locations, and we designed $\beta(x,y)$ following the heuristic suggested in [11]. For example, $\beta(x,y)$ is set by weighting $\Delta\omega(x,y,z)\mathrm{TE}$ with $b(z)$, the magnitude of the slice profile, and averaging it along the through-plane direction (z direction). The samples of $b(z)$ was obtained by running a Bloch simulation of

the basis slice-selective pulse.

Now, the cost function of our optimization can be set up as a following matrix-vector form.

$$\min_{\alpha_l(m,n),\mathbf{f}_m^n} \|\mathbf{B}\boldsymbol{\theta} - \mathbf{B}\sum_{l=1}^{L}\sum_{m=1}^{M}\sum_{n=1}^{N}\mathbf{S}_l\mathbf{W}_m\mathbf{f}_m^n\alpha_l(m,n)\|_2^2. \tag{5.2}$$

Here, $\mathbf{B}$ is a diagonal matrix containing the spatial samples of the slice profile, $b(z)$. $\mathbf{B}$ covers only the slice volume whose magnitude profile is above a certain threshold to exclude unselected volumes and thus to reduce the size of the problem. $\boldsymbol{\theta}$ is a column vector containing the spatial samples of $e^{i2\pi(\Delta\omega(x,y,z)\mathrm{TE}-\beta(x,y))}$, $\mathbf{S}_l$ is a diagonal matrix of spatial samples of the l-th coils sensitivity, $s_l(x,y)$, $\mathbf{W}_m$ is a diagonal matrix of spatial samples of the off-resonance phase, $e^{i2\pi\Delta\omega(x,y,z)(t_m-T)}$, and $\mathbf{f}_m^n$ is a column vector of spatial samples of a 3D complex exponential, $e^{i2\pi(xk_x(m)+yk_y(m)+zk_z(n))}$.

5.2.2 Optimization strategy

As presented in the Equation 5.2, our goal is to jointly compute optimal pulse weights and phase encoding locations. We extended our joint optimization algorithm introduced in Chapter IV to solve this problem based on the following observation. In Equation 5.2, the in-plane variation of $\mathbf{B}\boldsymbol{\theta}$ for any given slice index z is controlled by the basis signals associated with the chosen PE locations. In other words, if we view $\mathbf{B}\boldsymbol{\theta}$ as a stack of 2D subslices, $\boldsymbol{\theta}_z(x,y)$, as illustrated in Figure 5.4, we must linearly approximate all of them with the bases generated by a common set of PE locations. This implies that an effective candidate PE location creates bases that would be highly correlated with all 2D subslices, $\boldsymbol{\theta}_z(x,y)$. With L transmission coils, selecting one frequency, $\mathbf{f}$ for the m-th PE location would produce L bases, $\mathbf{BS}_1\mathbf{W}_m\mathbf{f}, ..., \mathbf{BS}_L\mathbf{W}_m\mathbf{f}$ to be used for approximating each 2D subslice. We extended sum of correlations in Equation 4.3 as following by adding a summation over this

subslice dimension to estimate how much one candidate PE location contributes to spanning all the subslices.

$$\sum_{k=1}^{N_z}\sum_{l=1}^{L} | < \mathbf{r}_k, b(k)\mathbf{S}_l\mathbf{W}_m^k\mathbf{f} > |^2. \tag{5.3}$$

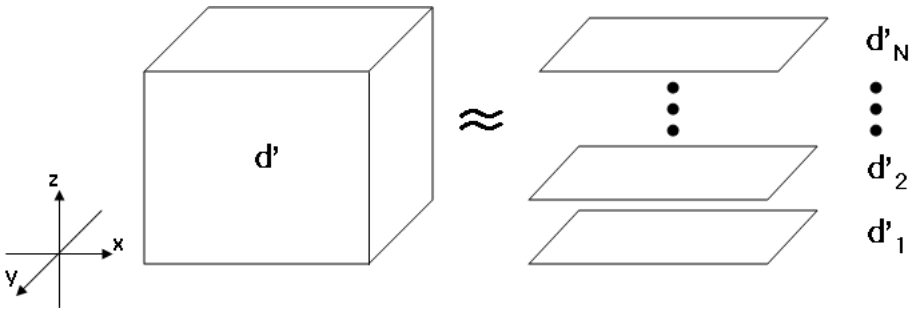

Figure 5.4: The 3D desired pattern $\mathbf{d}'$ can be viewed as a stack of 2D planes $\mathbf{d}'_1$ to $\mathbf{d}'_N$ after spatial sampling along the through-plane direction

Here k is the slice index, $b(k)$ is the magnitude of the slice profile at k, N_z is the number of subslices composing the 3D target pattern $\mathbf{r}$, $\mathbf{r}_k$ is the k-th slice in $\mathbf{r}$, and $\mathbf{W}_m^k$ is the k-th slice of $\mathbf{W_m}$. By simply extending the definition of cumulative correlation in Equation 4.3 to Equation 5.3, we could reuse the algorithm in Chapter IV to determine the PE locations.

Pulse weight computation stage had to be changed to compensate for the off-resonance effect because it became more complicated than the case introduced in Chapter IV due to the modification in the pulse sequence. In our pulse sequence, we found out that each time-shifted pulse would produce an excitation profile with a significantly different phase pattern where off-resonance was relatively high. This is because each time-shifted pulse tips magnetization at slightly different times such that the transverse magnetization tipped by different pulses will have different free precession time. Also, the fact that the basis pulses to create the same through-plane frequency are shifted in the opposite direction in time depending on the polarity of

the slice-select gradient made the off-resonance artifact more complicated, leading to a worse model mismatch. Since exciting the magnetization with a desired phase pattern is very critical in our solution approach, we could no longer ignore the off-resonance effect during the period that each basis pulse is transmitted as in Equation 5.2. We attempted to compensate this artifact in pulse weight computation stage. After we finished determining the PE locations, we computed the pulse weight for each time-shifted pulse using a slice profile considering off-resonance. We also learned empirically that the pulse weight should be explicitly regularized. We observed that as the desired pattern shows more localized and complex variation, the pulse weights tend to increase. This would definitely cause high power deposition into the object, and violate the small-tip angle assumption, resulting in a much poorer result than expected.

Considering the above two factors, we modified the Equation 5.2 as following to include a Tikhonov norm of pulse weights for regularization, and the slice-profile reflecting off-resonance.

$$\min_{\alpha_l(m,n),\mathbf{f}_m^n} \|\mathbf{B}\boldsymbol{\theta} - \sum_{l=1}^{L}\sum_{m=1}^{M}\sum_{n=1}^{N}\mathbf{B}_m^n\mathbf{S}_l\mathbf{W}_m\mathbf{f}_m^n\alpha_l(m,n)\|_2^2 + \lambda\sum_{l=1}^{L}\|\mathbf{a}_l\|_2^2. \tag{5.4}$$

B_m^n is the slice profile of the basis pulse associated with the m-th PE location and the n-th time shift. $\mathbf{a}_r$ is a column vector composed of scalar pulse weights for the r-th coil, $\alpha_l(m,n)$ in Equation 5.4. We may include the pulse power regularization during PE location selection as in [60], but that would require rerunning the entire optimization of PE locations and pulse weights every time we modify the weight for the Tikhonov norm to find an optimal trade-off point between the excitation accuracy and RF power deposition. Therefore, in order to reduce computation time, we chose to consider the pulse power deposition only in the pulse weight computation

after the PE locations are established. For each pulse design, λ was searched in a set 10, 20, 30, 40, .., 390, 400 and the minimum λ that does not tip magnetization over 90 degree during the entire pulse train was chosen.

5.3 Methods

5.3.1 Computer simulation

We implemented our pulse design method and ran Bloch-simulation to estimate the magnetization at the assumed echo time using the B0 fieldmap data we collected from in-vivo scans. We chose one slice where severe signal loss artifacts were observed, and computed RF pulses for 8 transmission coils with simulated sensitivities shown in Figure 4.2. We also computed the RF pulse for a single transmission coil with uniform sensitivity to verify the validity of our assumed pulse sequence and our RF pulse design. The target slices were 5 mm thick and B0 fieldmap data was acquired from 1mm-thick sub-slices. The excitation field of view was 24cm x 24cm x 7mm, and a 64x64x7 (x-y-z dimension) uniform spatial sampling grid was applied to obtain the samples of the desired excitation pattern. The candidates for the PE locations are formed in the same manner as in the Chapter IV. The through-plane frequencies were uniformly sampled from -2 cycle/cm to 2 cycle/cm and yielded 5 candidate frequencies. Each kz-line in the EV trajectory was set to cover the through-plane frequencies ranging from -6 cycle/cm to 6 cycle/cm. The sinc pulse with one side lobe was employed for a basis slice-selective pulse. For each method, an RF pulse was designed using 10 PE locations, which yield an RF pulse about 11.8ms long.

5.3.2 In-vivo experiment

At the time of writing this report, our parallel excitation hardware was not stable enough to run and test our pulse design method, so we could not conduct in-vivo

experiments to test our parallel excitation RF pulse design algorithm. Instead, we applied our algorithm to compute an RF pulse for single coil transmission, and performed a human brain scan with it. Though this is limited, we hope that this experiment still demonstrate validity of the concept in our pulse design algorithm. We ran a gradient recalled echo sequence with a spiral-in acquisition k-space trajectory. TE = 30ms, TR = 1s, the image size was 64x64, and the nominal flip-angle was 30 degree. The image was reconstructed with an iterative method with off-resonance correction [81]. The B0 fieldmap data was obtained with a spin-warp sequence with two different echo time, 5ms and 7ms. The B0 fieldmap was later estimated using a regularized fieldmap estimation in image domain [82]. The RF pulse design parameters were same as in section 5.3.1.

5.4 Results

5.4.1 Computer simulation

Figure 5.5 shows the excitation regions of interest, the B0 fieldmap of the center subslice, and the through-plane gradient map computed using the top and the bottom subslices. The selected slices are closely located to the air cavity regions of the human head, and typically show multiple regions of severe signal loss in a T2* weighted image due to the strong, localized through-plane gradient. The severity of signal loss can be roughly estimated by the through-plane gradient map. The slice-thickness is thin enough (5mm) to approximate through-plane gradient as a linear function, so we may assume that the through-plane phase variation is linear as well. If we also suppose the density is constant within a voxel, then the net magnetization over a voxel can be modeled with a sinc function of the through-plane gradient. The through-plane gradient map in Figure 5.5 shows high amplitude around regions close to air cavity such as ears and a frontal sinus. For the through-plane gradient of ± 0.016g/cm, a

2π linear phase is created along the slice-select direction for a 5mm slice, leading to almost complete signal loss.

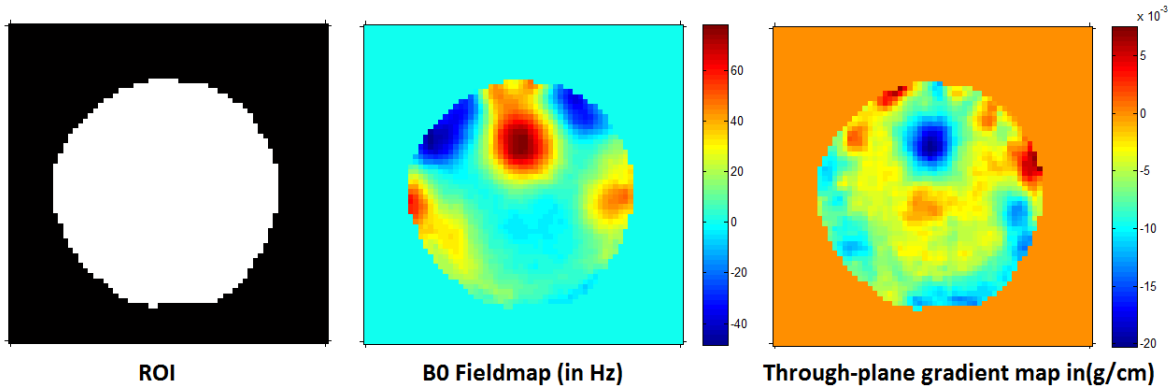

Figure 5.5: Excitation region of interest, B0 fieldmap and through-plane phase gradient map of the simulated slice for which we designed RF pulses. The B0 fieldmap is taken from the subslice in the center, and the through-plane phase variation was computed from the off-resonance frequency difference between the top and the bottom subslices. In 30ms echo time, The through-plane gradient of 0.016g/cm creates a 2π linear phase for the 5mm thick slice, leading to a complete signal loss.

The signal recovery result with our pulse design using 8 transmission coils and a single coil is displayed in Figure 5.6. The conventional single sinc pulse transmission shows a serious signal loss around the ears and a frontal sinus, which is expected from the through-plane gradient map. The results with our pulse design shows a large reduction in the signal loss regions. The RF pulse with 8 transmission coils show better signal recovery performance than the signal transmission case as expected. The normalized excitation error of the RF pulse decreased from 42% to 29% when we used 8 coil parallel transmission instead of a single coil transmission, which lead to the improved signal recovery performance.

5.4.2 In-vivo experiment

Figure 5.7 displays the T2* weighted images of an axial slice of a human brain acquired with our pulse design and a conventional sinc pulse. Both pulses are transmitted using a single coil. In the conventional sinc pulse case, severe signal loss is

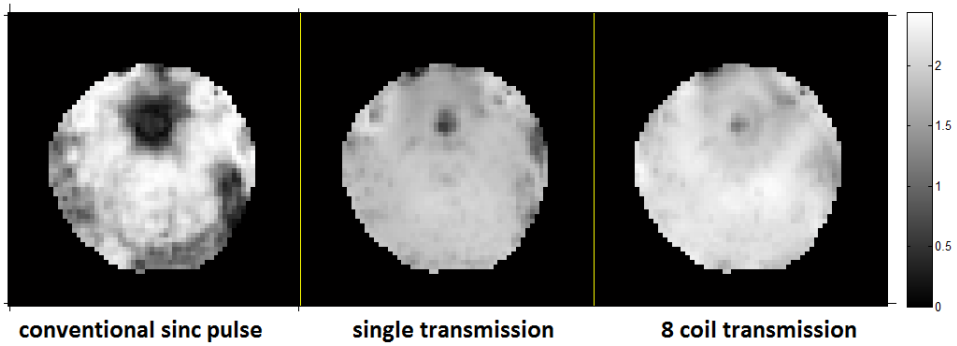

Figure 5.6: Simulated transverse magnetization at echo time with different RF pulses. The magnetization with the conventional single sinc pulse shows typical signal loss pattern around the ear and the frontal sinus, while the RF pulses with our pulse design show improved signal recovery pattern. The RF pulse with 8 transmission coils achieved higher excitation accuracy than the RF pulse with single transmission, and could obtain higher signal amplitude over most of regions.

observed in the inferior frontal cortex region located right above the frontal sinus. As we see from the B0 fieldmap in Figure 5.7, a very strong off-resonance frequency is developed, leading to considerable signal loss in the conventional T2* weighted imaging. On the other hand, the T2* weighted image with our pulse in Figure 5.7 illustrates that the most of dark holes observed in the conventional image are removed, demonstrating that we could achieve desired signal recovery with our pulse design.

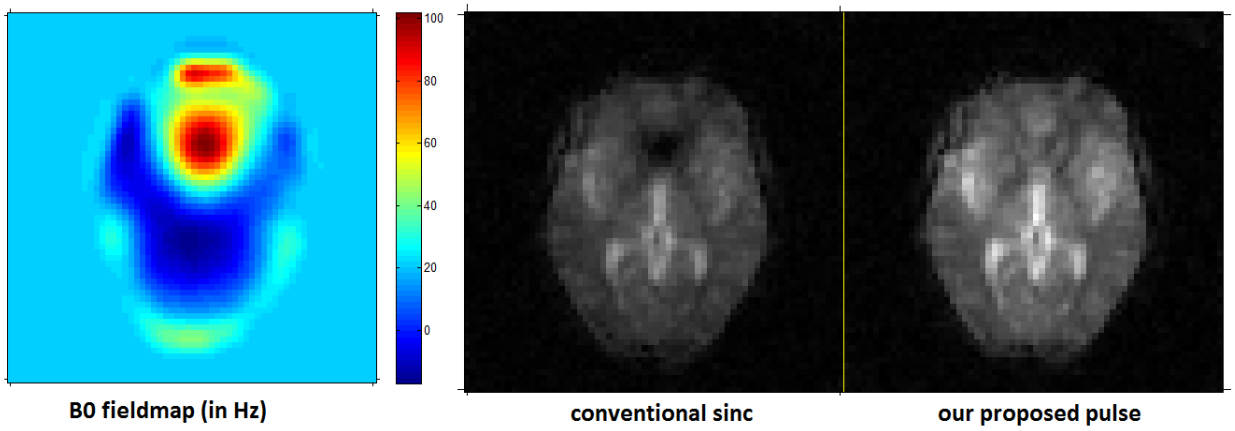

Figure 5.7: B0 fieldmap of the subslice at the center and T2* weighted images acquired with a conventional sinc pulse and our proposed pulse. Our pulse design shows a large reduction of signal loss regions and overall improvement in the signal magnitude

5.5 Discussion

In this chapter, we proposed a novel parallel excitation pulse design algorithm for jointly designing the gradient waveforms and RF pulse waveforms to solve a signal loss problem in BOLD fMRI. We demonstrated with computer simulation that with parallel excitation, we could achieve better signal recovery performance than single coil excitation. We also conducted an in-vivo experiment with our algorithm applied to single coil transmission as a proof of concept. Both simulation and in-vivo experiment results show that our algorithm can effectively correct for the signal loss in T2* weighted imaging for brain fMRI.

Even though the parallel excitation does achieve better excitation accuracy than the signal coil excitation, it did not make a sufficiently large difference in the signal recovery performance in our experiments. One reason is that the required excitation pattern is very complicated, and locally varying such that it may not be so accurately approximated with a limited number of PE locations. In that case, the excitation error may decrease slowly as we use more transmission coils or more PE locations. Another reason is that the greedy algorithms tested above tend to choose PE locations that entail a very large pulse weight, which, after regularization, does not achieve improved excitation accuracy as predicted initially in PE location selection. For example, in our simulated case, the normalized excitation error predicted to be 20% without pulse power regularization, but after the regularization to avoid small-tip angle violation, it creased to 29%. Therefore we may need to modify PE location selection algorithm to suppress large pulse weights in order to observe the small-tip angle assumption and to fully exploit the potential benefit of joint optimization for gradient and RF waveforms. The current optimization scheme, in fact, separately

optimize the PE locations and the pulse weights, so this may be another cause of potential ineffectiveness.

One may question if our approach of decomposing the RF pulse with basis pulses can achieve as high excitation accuracy as the approach discretizing the RF pulses into fine time samples[33]. The latter approach definitely gives more freedom in determining the RF pulses, which probably include the RF pulse computed with our proposed method in its potential solutions. We may support our RF pulse decomposition approach in the small tip-angle domain as following. Suppose the desired excitation pattern is expressed as $b(z)\theta(x,y,z)$ where $b(z)$ is the through-plane slice profile indicating that the desired RF pulse should be slice-selective, and $\theta(x,y,z)$ describes the desired magnetization pattern within the selected volume. In our experiment $\theta(x,y,z)$ was the pre-phasing pattern compesating the off-resonance phase accural at echo time. Since the support of $\theta(x,y,z)$ is limited by $b(z)$ for the through-plane dimension (z axis) and by the finite size of the excited object for the in-plane dimension(x-y axis), we can create $\hat{\theta}(x,y,z)$, a periodic repetition of $\theta(x,y,z)$, and substitute it for $\theta(x,y,z)$ in the desired excitation pattern. For example $b(z)\theta(x,y,z) \equiv b(z)\hat{\theta}(x,y,z)$. Now we take Fourier series of $\hat{\theta}(x,y,z)$ to represent it as a sum of weighted complex exponentials and represent the desired pattern as following :

$$b(z)\hat{\theta}(x,y,z) = b(z)\sum_{m=-\infty}^{\infty}\sum_{n=-\infty}^{\infty}\sum_{l=-\infty}^{\infty} c_{m,n,l}e^{i2\pi\frac{m}{XFOV_x}x}e^{i2\pi\frac{m}{XFOV_y}y}e^{i2\pi\frac{m}{XFOV_z}z}. \tag{5.5}$$

$c_{m,n,l}$ is the Fourier series coefficent for the complex exponential whose frequency is indexed by (m,n,l). $XFOV_x$, $XFOV_y$, and $XFOV_z$ is the period of $\hat{\theta}(x,y,z)$

along x, y, and z axis respectively, which is equivalent to the excitation field of view (XFOV) size for each dimension. Equation 5.5 is very similar to Equation 5.1 that describes the excited pattern from our pulse design if we reduce it to a single coil transmission case. In fact, Equation 5.5 can approximate Equation 5.1 reasonably well if $\hat{\theta}(x, y, z)$ can be represented with a limited number of sinusoids with high accuracy. Therefore, we may claim that the our pulse design approach adopting basis pulse decomposition may be sufficient enough to compute RF pulses to excite the desired excitation pattern.

For our future work, we will further evaluate our algorithm with fMRI studies to find whether the signal recovery from our pulse design makes statistically significant changes in detecting brain activations, especially on the brain regions suffering from considerable signal loss. Implementing our algorithm with parallel excitation hardware and comparing its performance with single coil excitation is another topic to work on. For pulse design perspective, we plan to investigate an optimization scheme to determine PE locations considering constraints for the pulse weight to observe the small-tip angle domain assumption. Also, we will develop a fast optimization scheme to jointly optimize the in-plane phase relaxation pattern with the gradient and RF waveforms and evaluate its practicality.

5.6 Conclusion

We have introduced a parallel excitation RF pulse design method to compute RF pulse and gradient waveforms to mitigate signal loss in BOLD fMRI. We designed our RF pulse to excite the magnetization with pre-compensatory phase to cancel the off-resonance phase along the through-plane direction at echo time. With computer simulation and in-vivo experiment, we demonstrated effectiveness of our pulse design

algorithm. In future work, we plan to conduct fMRI experiments to further verify the signal recovery in terms of brain activation detection. Also, we will investigate an efficient way to incorporate a pulse power regularization in our PE location selection procedure.

CHAPTER VI

Joint design method for parallel excitation RF pulse and gradient waveforms for large tip-angles

6.1 Introduction

Many RF pulse design methods have been proposed for parallel excitation since its invention [1, 2], but most of them have focused on optimizing RF pulses for predetermined gradient waveforms. Typically, these predetermined gradient waveforms were not chosen with any optimization criteria, so there can be a good chance for further improving the excitation accuracy or reducing pulse power deposition by jointly optimizing RF pulse and gradient waveforms. Recently, several joint optimization methods have been proposed to improve excitation accuracy [16, 60, 59, 83], all of which were limited in a small-tip angle domain. In a large tip-angle domain, many parallel excitation RF pulse design algorithms were published [84, 85, 86, 87, 88, 89], but none of them were considering joint optimization of RF pulse and gradient waveforms. The results from the joint optimization methods for a small tip-angle domain [16, 60, 59, 83] showed that there exist certain cases that excitation accuracy can be significantly improved with a joint optimization. These results definitely encourage the development of joint design method for the RF pulse and gradient waveforms to achieve arbitrary tip-angle excitation.

In this chapter, we present a preliminary work on the joint design of RF and

gradient waveforms for parallel excitation in an arbitrary tip-angle domain. Our method assumes the pulse sequence presented in Chapter IV, which is composed of trains of weighted slice-selective pulses interleaved by in-plane gradient blips. Our goal here is to determine the RF pulse weights and in-plane gradient blips to achieve the desired excitation pattern with an arbitrary tip-angle. We used the excited magnetization pattern at the slice-center to guide the optimization of pulse weights and gradient waveforms for simplicity of optimization. In the optimization, we first initialize the RF pulse weights and gradient waveforms with a greedy method, which will be presented in detail later in Theory section. Then for each unit RF pulse segment in the pulse train, we locally update the RF pulse weight and the gradient waveforms. We sequentially update each pulse segment, and repeat the whole process until there is no significant improvement. In the local update for the RF pulse weight, we adopted the method proposed by [89], which linearizes the Bloch-equation for a small RF pulse update. Our method still provides the slice-selectivity because each basis pulse in the pulse train is slice-selective, but does not guarantee the ideal through-plane slice profile because it is not explicitly considered in the optimization. However, with computer simulation, our proposed pulse design demonstrates that the computed RF pulse and gradient waveforms achieve a reasonable slice profile and significantly improved excitation accuracy over a solution obtained by scaling RF pulses computed with a small tip-angle domain method [59].

6.2 Theory

6.2.1 Optimization formulation

Our proposed pulse design uses the pulse sequence briefly illustrated in Fig 6.1. Trains of slice-selective RF pulses each of which is weighted by a complex weight are transmitted, and the unit RF pulses are interleaved by in-plane gradient blips.

The benefits of this RF pulse sequence were explained in Chapter IV, which can be summarized as guaranteed slice-selectivity and a large reduction of the number of parameters to optimize. In our algorithm, we do not limit the desired tip-angle to be in a small tip-angle domain [6], so there is no simple linear relationship between the input RF and gradient waveforms and the output excitation pattern. Therefore, we should directly use the original non-linear input-output relationship, the Bloch-equation, for our optimization.

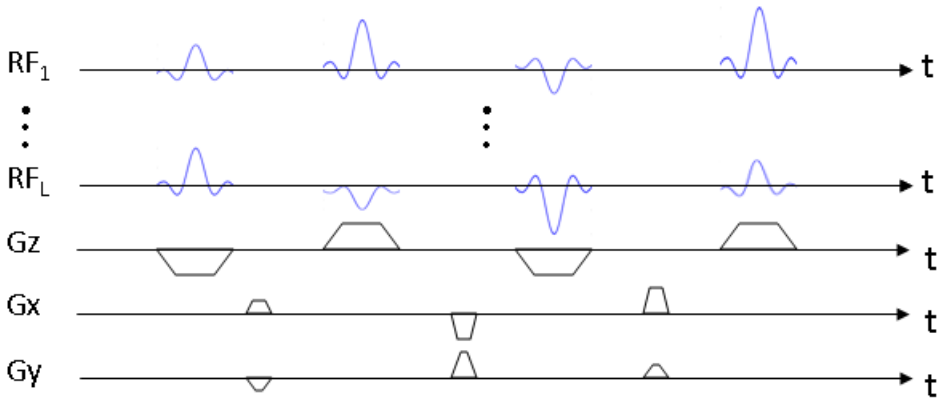

Figure 6.1: The target pulse sequence to optimize. The pulse sequence consists of trains of weighted basis RF pulses interleaved by in-plane gradient blips. Because each basis RF pulse is slice-selective, this pulse sequence provides inherent slice-selectivity.

In essence, the Bloch-equation describes that magnetization rotates around the applied magnetic field. In general excitation process, the applied magnetic field is sum of the gradient field and the RF field that can be time-varying, so this makes the estimation of the resulting excitation pattern very complicated. However, if the direction of the net magnetic field experiences only sign alternation, the effect of the magnetic field can be modeled as a simple rotation where the axis of the rotation is the direction of the magnetic field, and the rotation angle is determined from the time-integral of the magnetic field. This observation can be used to simplify the estimation of the magnetization change at $z = 0$ during each unit RF pulse.

Because the slice-select gradient field (z-gradient field) becomes zero at $z = 0$, the only effective field there is the RF field. In our assumed pulse sequence, the total RF field at $(x, y, z = 0)$ formed by the n-th RF pulse segment is $b(t) \sum_{l=1}^{L} s_l(x, y) w_l(n)$, where $b(t)$ is the basis sinc pulse, l is the coil index, L is the number of coils, $s_l(x, y)$ is the l-th coil's sensitivity, and $w_l(n)$ is the pulse weight of the n-th basis pulse for the l-th coil. The above model shows that the net RF field is still a sinc RF pulse scaled by a weighted combination of the sensitivity patterns, which implies that the rotation from the net RF field is determined from the term, $\sum_{l=1}^{L} s_l(x, y) w_l(n)$. For example, the direction of the rotation axis is determined as $\angle(\sum_{l=1}^{L} s_l(x, y) w_l(n))$, and the rotation angle (following a left-hand rule) is $\theta|\sum_{l=1}^{L} s_l(x, y) w_l(n)|$, where θ is the tip-angle of the basis pulse. On the other hand, when each in-plane gradient blip is transmitted, there is no RF field turned on, so it is the only magnetic field determining the rotation of the magnetization. Its rotation effect is to simply add a linear phase to the transverse magnetization. The spatial frequency of the linear phase is determined from the integral of the gradient blip. In our optimization, we first compute the spatial frequency for the n-th gradient blip, and then derive the gradient waveform subject to the hardware capability constraints. Combining the aforementioned rotation models for both RF pulse and gradient waveforms, we could set up a cost function as following for the optimization of the RF pulse and gradient waveforms.

$$\min_{\forall w_l(n), \forall k_x(n), \forall k_y(n)} \sum_{\forall \mathbf{r}} \|\mathbf{d_r} - \mathbf{W_r}^N \mathbf{G_r}^N \mathbf{B_r}^N ... \mathbf{W_r}^1 \mathbf{G_r}^1 \mathbf{B_r}^1 \mathbf{m_r}\|_2^2 \tag{6.1}$$

$\mathbf{r}$ is a vector containing spatial coordinates. $\mathbf{d_r}$ and $\mathbf{m_r}$ are 3x1 column vectors specifying the x, y, and z component of the desired magnetization and the initial magnetization at $\mathbf{r}$ respectively. $\mathbf{B_r}^n$ is the 3x3 rotation matrix determined by the n-th

Optimization procedure outline
Initialize the pulse weights, $w_l(n)$, and the 2D linear frequencies, $(k_x(n), k_y(n))$.
Loop until the cost function value in Equation 6.1 does not decrease significantly
for n = N : 1
Minimize Equation 6.1 w.r.t $(k_x(n), k_y(n))$
update $(k_x(n), k_y(n))$ with the minimizer found above
Minimize Equation 6.1 w.r.t $w_l(n)$ for l = 1, 2, ..., L
update $w_l(n)$ with the minimizer found above
end
end

Table 6.1: The outline of our optimization procedure

RF pulse, $\mathbf{G_r}^n$ is the 3x3 rotation matrix by the n-th gradient blip characterized by the associated 2D spatial frequency, $k_x(n)$ and $k_y(n)$. $\mathbf{W_r}^n$ is the 3x3 rotation matrix indicating off-resonance phase accrual to the transverse magnetization between n-th and n+1-th pulse segment. Note that $k_x(n)$ and $k_y(n)$ are not the reverse time integral of the gradient waveforms as defined in [6]. Here they are $k_x(n) = \gamma \int g_x^n(t)dt$, $k_y(n) = \gamma \int g_y^n(t)dt$, where $g_x^n(t)$ and $g_y^n(t)$ are the n-th x and y gradient blips respectively. As described above, $\mathbf{B_r}^n$ is a function of $w_l(n)$ and $\mathbf{G_r}^n$ is a function of $k_x(n)$ and $k_y(n)$, and our purpose is to find optimal $w_l(n), k_x(n), k_y(n)$ such that the resulting rotation operations can accurately map the initial magnetization $\mathbf{m_r}$ onto $\mathbf{d_r}$.

6.2.2 Optimization strategy

Our optimization strategy here is to sequentially update the pulse weights and the gradient waveforms for each pulse segment by fixing every other pulse segment but the one being updated. The update happens from the last pulse segment, and after finishing updates of all pulse segments, then we repeat the whole cycle until there is no significant improvement in the cost function. Table 6.1 summarizes our optimization procedures.

6.2.3 Initialization of RF pulse weights and gradient blips

We initialized the pulse weights and gradient blips by determining the pulse segment from the last in a greedy manner as in [59] presented in Chapter IV. In this case, we can assume that whenever we add a new pulse segment, it always operates on the fully relaxed initial magnetization, which has no transverse components. One advantage of this approach is that we can treat the effect of the gradient field as the linear RF phase variation such that we can merge the RF field and gradient field together. For example, if the RF field is $\sum_{l=1}^{L} s_l(x,y)w_l$ and the gradient field is creating a linear phase of $e^{i2\pi(xk_x+yk_y)}$, then the sequential application of these two to the initial magnetization is equivalent to applying an RF filed, $\sum_{l=1}^{L} s_l(x,y)w_l e^{i2\pi(xk_x+yk_y)}$. We use this formula to determine optimal w_l, k_x, and k_y that best fits the corresponding RF field, $\sum_{l=1}^{L} s_l(x,y)w_l e^{i2\pi(xk_x+yk_y)}$, into the ideal RF field rotating the initial magnetization onto the desired magnetization.

Suppose we are adding the n-th from the last pulse segment. We first determine new desired magnetization pattern for the n-th pulse segment by applying the inverse rotations of the pulse segments following the n-th pulse segment to the original desired magnetization pattern. For example, the new desired magnetization pattern, $\hat{\mathbf{d}}_{\mathbf{r}}$, is defined as $\left(\mathbf{W_r}^N\mathbf{G_r}^N\mathbf{B_r}^N...\mathbf{W_r}^{n+1}\mathbf{G_r}^{n+1}\mathbf{B_r}^{n+1}\right)^{-1}\mathbf{d_r}$. Then, for each spatial location, $\mathbf{r}$, we compute an ideal RF field, $\mathbf{b_r}$, that rotates the initial magnetization $\mathbf{m_r}$ onto the desired magnetization $\hat{\mathbf{d}}_{\mathbf{r}}$. The ideal RF field can be derived by computing an axis of rotation and a rotation angle that is needed to rotate $\mathbf{m_r}$ onto $\hat{\mathbf{d}}_{\mathbf{r}}$. Finally we compute the $w_l(n)$, $k_x(n)$, $k_y(n)$ by minimizing the $l2$ distance between the combined RF field describe above and the ideal RF field as following. We assume here $\mathbf{r} = (x,y)$.

$$\min_{w_l(n),k_x(n),k_y(n)} \sum_{\forall x,y} \|b_{x,y} - \sum_{l=1}^{L} s_l(x,y) w_l(n) e^{i2\pi(xk_x(n)+yk_y(n))}\|_2^2 \tag{6.2}$$

This minimization is exactly same as what we solved in Chapter IV when the number of PE location is one. Therefore, we can reuse our previous algorithm to solve this problem. One difference here is that the distance measured in the cost function is in the RF field domain, not in the magnetization domain as in Chapter IV. Therefore, the minimizer may not be optimal for our final cost function in Equation 6.1 that measures the difference in the magnetization domain. However, we learned from simulation experiments that the initial solution found with this approach has a better result than a scaled version of a small tip-angle solution, which is a typical initializer for most of large tip-angle RF pulse design methods.

6.2.4 Update of RF pulse weights

In updating RF pulse weights for the n-th pulse segment, $w_1(n)$, ..., $w_L(n)$, we fix all other parameters and minimize the cost function in Equation 6.1 with respect to them as following.

$$\begin{aligned}
& \min_{w_l(n)} \sum_{\forall \mathbf{r}} \|\mathbf{d_r} - \mathbf{W_r}^N \mathbf{G_r}^N \mathbf{B_r}^N ... \mathbf{W_r}^n \mathbf{G_r}^n \mathbf{B_r}^n ... \mathbf{W_r}^1 \mathbf{G_r}^1 \mathbf{B_r}^1 \mathbf{m_r}\|_2^2 \\
\equiv & \min_{w_l(n)} \sum_{\forall \mathbf{r}} \| \left(\mathbf{W_r}^N \mathbf{G_r}^N \mathbf{B_r}^N ... \mathbf{W_r}^n \mathbf{G_r}^n\right)^{-1} \mathbf{d_r} - \mathbf{B_r}^n ... \mathbf{W_r}^1 \mathbf{G_r}^1 \mathbf{B_r}^1 \mathbf{m_r}\|_2^2 \\
\equiv & \min_{w_l(n)} \sum_{\forall \mathbf{r}} \|\hat{\mathbf{d}}_\mathbf{r} - \mathbf{B_r}^n \hat{\mathbf{m}}_\mathbf{r}\|_2^2, \qquad (6.3)
\end{aligned}$$

where $\hat{\mathbf{d}}_\mathbf{r} = \left(\mathbf{W_r}^N \mathbf{G_r}^N \mathbf{B_r}^N ... \mathbf{W_r}^{n+1} \mathbf{G_r}^{n+1} \mathbf{B_r}^{n+1} \mathbf{W_r}^n \mathbf{G_r}^n\right)^{-1} \mathbf{d_r}$, and $\hat{\mathbf{m}}_\mathbf{r} = \mathbf{W_r}^{n-1} \mathbf{G_r}^{n-1} \mathbf{B_r}^{n-1} ... \mathbf{W_r}^1 \mathbf{G_r}^1 \mathbf{B_r}^1 \mathbf{m_r}$. Note that the equivalence between the first and the second line of Equation 6.3 is valid because rotation operations are norm-preserving and composite rotations and inverse rotations are still rotations.

The main difficulty in minimizing Equation 6.3 is that the mapping from the pulse weights to the corresponding rotation matrix is non-linear and very complicated, so it is not easy to find a simple relationship between the pulse weights and the rotated magnetization. Instead of relating the rotated magnetization with the pulse weights through the rotation matrix, $\mathbf{B_r}^n$, we use locally linearized Bloch-equation to find a local linear relationship between small updates of RF pulse weights and the transverse component of the rotated magnetization. This approach is inspired by the method proposed by Zheng et al. [89]. The integral form of the Bloch equation to model the transverse magnetization change for $\mathbf{B_r}^n\hat{\mathbf{m}}_\mathbf{r}$ is as following :

$$
\begin{aligned}
M_{tv}(x,y,T) &= M_{tv}(x,y,0) + i\gamma \int_0^T M_z(x,y,t)b(x,y,t)dt \\
M_{tv}(x,y,T) &= M_{tv}(x,y,0) + i\gamma \int_0^T M_z(x,y,t)b(t) \sum_{l=1}^{L} s_l(x,y)w_l(n)dt \\
&= M_{tv}(x,y,0) + \left\{ i\gamma \int_0^T M_z(x,y,t)b(t)dt \right\} \sum_{l=1}^{L} s_l(x,y)w_l(n) \qquad (6.4)
\end{aligned}
$$

$M_{tv}(x,y,t)$ is the transverse magnetization at a spatial coordinate (x,y) at time t. $M_z(x,y,t)$ is the longitudinal magnetization at (x,y,t). Without loss of generality, we can set the time 0 as the beginning of the n-th RF pulse, and T as the end of the RF pulse segment. In our pulse sequence, $b(t)$ is the basis sinc pulse, but for the sake of optimization, we can replace it with a simple hard pulse achieving a small tip-angle since we only use the magnetization at z=0. In fact, we can replace the basis sinc pulse with any pulse achieving the same tip-angle for our optimization, but we chose the hard pulse because it is not time-varying and thus most simple.

Suppose we have a small update $\Delta w_l(n)$ for each $w_l(n)$. Then the resulting transverse magnetization $\hat{M}_{tv}$ and the longitudinal magnetization $\hat{M}_z$ can be modeled using Equation 6.4 as following :

$$\hat{M}_{tv}(x,y,T) = M_{tv}(x,y,0) + \left\{ i\gamma \int_0^T \hat{M}_z(x,y,t)b(t) \right\} \sum_{l=1}^{L} s_l(x,y)(w_l(n) + \Delta w_l(n))dt. \quad (6.5)$$

If we assume $\hat{M}_z(x,y,t) \approx M_z(x,y,t)$ because $\Delta w_l(n)$ is small, then we can further approximate Equation 6.5 as following :

$$\hat{M}_{tv}(x,y,T) \approx M_{tv}(x,y,T) + \left\{ i\gamma \int_0^T M_z(x,y,t)b(t) \right\} \sum_{l=1}^{L} s_l(x,y)\Delta w_l(n)dt. \quad (6.6)$$

Equation 6.6 shows a linear relationship between the pulse update and the resulting transverse magnetization. Using this, we compute the optimal pulse weight update by minimizing $l2$ distance between the desired transverse magnetization, $\hat{d_{tv}}(x,y,T)$, and the excited transverse magnetization, $\hat{M}_{tv}(x,y,T)$ as following :

$$\begin{aligned} & \min_{\Delta w_1(n), \Delta w_2(n), \ldots \Delta w_L(n)} \sum_{\forall x,y} \|\hat{d_{tv}}(x,y,T) - \hat{M}_{tv}(x,y,T)\|_2^2 \\ \equiv & \min_{\Delta \mathbf{w}} \|\mathbf{d_{tv}} - \mathbf{m_{tv}} - \mathbf{A}\Delta\mathbf{w}\|_2^2. \end{aligned} \quad (6.7)$$

$\mathbf{r} = (x,y)$, and $\hat{M}_{tv}(x,y,T)$ is a function of $\Delta w_l(n)$ as shown in Equation 6.6. The second line of Equation 6.7 is rewriting of the first line in a matrix vector form. $\Delta\mathbf{w}$ is a Lx1 column vector containing pulse weights for each coil, and its l-th element is $\Delta w_l(n)$. $\mathbf{d_{tv}}$ and $\mathbf{m_{tv}}$ are column vectors containing spatial samples of $\hat{d_{tv}}(x,y,T)$ and $M_{tv}(x,y,T)$. $\mathbf{A}$ is a matrix of L columns where the l-th column has spatial samples of $\left\{ i\gamma \int_0^T M_z(x,y,t)b(t) \right\} s_l(x,y)$. The minimizer of the cost function in Equation 6.7 is $\left(\mathbf{A}^h\mathbf{A}\right)^{-1}\mathbf{A}^h\left(\mathbf{d_{tv}} - \mathbf{m_{tv}}\right)$. The pseudo-inverse of

$\mathbf{A}$, $\left(\mathbf{A}^h\mathbf{A}\right)^{-1}$ is a LxL matrix where L is a number of transmission coils. The typical number of the coils is usually less than 8 in the current technology, so computing the pseudo-inverse matrix can be done very quickly. In populating the $\mathbf{A}$ matrix, one should know $\left\{i\gamma\int_0^T M_z(x,y,t)b(t)\right\}$, where figuring out $M_z(x,y,t)$ may require Bloch simulation of $b(t)$, which can be very demanding computationally. However, the integral does not have to be directly evaluated. Since we know every terms in Equation 6.4 except the integral term, it can be simply computed as $\left\{i\gamma\int_0^T M_z(x,y,t)b(t)\right\} = \frac{M_{tv}(x,y,T)-M_{tv}(x,y,0)}{\sum_{l=1}^{L} s_l(x,y)w_l(n)}$. We keep updating the pulse weights until there is no significant update. For the initial solution for the pulse weights $w_l(n)$, we can use the pulse weights determined in the previous cycle or compute it based on the ideal RF field fitting we used for initializing the whole pulse segment in the beginning of the optimization. We computed both of them, and chose the one with less cost function value.

6.2.5 Update of $(k_x(n), k_y(n))$

In computing $(k_x(n), k_y(n))$, we take the same approach with the pulse weight update. We fix all other input parameters, and rewrite the initial cost function in Equation 6.1 as we did to derive Equation 6.3. The result of rewriting is as following:

$$
\begin{aligned}
& \min_{k_x(n),k_y(n)} \sum_{\forall \mathbf{r}} \|\mathbf{d_r} - \mathbf{W_r}^N\mathbf{G_r}^N\mathbf{B_r}^N ... \mathbf{W_r}^n\mathbf{G_r}^n\mathbf{B_r}^n ... \mathbf{W_r}^1\mathbf{G_r}^1\mathbf{B_r}^1\mathbf{m_r}\|_2^2 \\
\equiv & \min_{k_x(n),k_y(n)} \sum_{\forall \mathbf{r}} \| \left(\mathbf{W_r}^N\mathbf{G_r}^N\mathbf{B_r}^N ... \mathbf{W_r}^n\right)^{-1} \mathbf{d_r} - \mathbf{G_r}^n\mathbf{B_r}^n ... \mathbf{W_r}^1\mathbf{G_r}^1\mathbf{B_r}^1\mathbf{m_r}\|_2^2 \\
(6.8) \equiv & \min_{k_x(n),k_y(n)} \sum_{\forall \mathbf{r}} \|\hat{\mathbf{d}}_\mathbf{r} - \mathbf{G_r}^n\hat{\mathbf{m}}_\mathbf{r}\|_2^2,
\end{aligned}
$$

$\hat{\mathbf{d}}_\mathbf{r}$ is $\left(\mathbf{W_r}^N\mathbf{G_r}^N\mathbf{B_r}^N ... \mathbf{W_r}^n\right)^{-1}\mathbf{d_r}$, and $\hat{\mathbf{m}}_\mathbf{r}$ is $\mathbf{B_r}^n ... \mathbf{W_r}^1\mathbf{G_r}^1\mathbf{B_r}^1\mathbf{m_r}$. $\mathbf{G_r}^n$ only add phase to the transverse component of $\hat{\mathbf{m}}_\mathbf{r}$, so from now on, we will consider evaluating

the cost function value only for the transverse component of $\hat{\mathbf{m}}_\mathbf{r}$ and $\hat{\mathbf{d}}_\mathbf{r}$. Suppose we sampled the transverse component of $\hat{\mathbf{d}}_\mathbf{r}$ with a P X Q sampling grid to form a P x Q matrix, $\hat{\mathbf{d}}$, and the same sampling grid was applied to $\hat{\mathbf{m}}_\mathbf{r}$ to form a P x Q matrix, $\hat{\mathbf{m}}$. Then, Equation 6.8 can be rewritten as following:

$$\min_{\hat{k}_x(n),\hat{k}_y(n)} \sum_{p=1}^{P}\sum_{q=1}^{Q} \|\hat{d}(p,q) - \hat{m}(p,q)e^{i2\pi(\frac{p\hat{k}_x(n)}{P}+\frac{q\hat{k}_y(n)}{Q})}\|_2^2. \tag{6.9}$$

Here $\hat{k}_x(n) = \text{XFOV}_x \cdot k_x(n)$ and $\hat{k}_y(n) = \text{YFOV}_y \cdot k_y(n)$. If we limit $\hat{k}_x(n)$ and $\hat{k}_y(n)$ to be DFT frequencies, which are integers, then there exists an analytical solution for the optimal $\hat{k}_x(n)$ and $\hat{k}_y(n)$ as following.

$$\arg\max_{\hat{k}_x(n),\hat{k}_y(n)} Re\left(DFT_{2D}\left\{\hat{d}(p,q).*\text{conj}\{\hat{m}(p,q)\}\right\}\right) \tag{6.10}$$

$Re\{\cdot\}$ means taking the real part of the argument, and $DFT_{2D}\{\cdot\}$ is the 2D DFT. conj$\{\cdot\}$ is the operation taking the complex conjugate of the argument. In short, we form a new 2D matrix by taking an element-wise product between $\hat{d}(p,q)$ and the conjugated $\hat{m}(p,q)$ and take 2D DFT of it, and find the 2D DFT frequency with the largest real 2D DFT value. Since DFT is a very fast operation, computing the optimal 2D frequency can be performed very quickly.

6.3 Method

We implemented our pulse design method and tested it with Bloch-simulation on a computer with Intel Q6600 CPU at 2.4 GHz and 4GB RAM. The simulation was implemented with Matlab (MathWorks, Natick, MA). We designed two types of large tip-angle RF pulses: a 90 degree excitation pulse, and 180 degree inversion pulse for a 5mm-thin slice. For 90 degree excitation pulse design, the phase of the desired excitation pattern was set to 0, attempting to perfectly uniform excitation.

In testing our 90 degree excitation pulse, we measured the transverse magnetization at z=-5mm, -4mm, ... 5mm to check the uniformity of the in-plane slice profile and the through-plane slice profile. We ran the same test for our 180 degree inversion pulse, but measured the longitudinal magnetization instead. Our pulse design was compared with a scaled version of our small tip-angle RF pulse introduced in Chapter IV. The small tip-angle pulse achieving 10 degree flip angle was designed and scaled to match the new target tip-angle. For example, for the 90 degree tip-angle pulse, it was scaled by 9, and for the 180 degree tip-angle pulse, it was scaled by 18.

The excitation region of interest and B0 fieldmap data for our RF pulse simulation were obtained with in-vivo human scans. They were used to test our small-tip angle RF pulse design method introduced in Chapter IV, and are displayed in Figure 6.2. The dimension of the excitation field of view was 24cm x 24cm, and a 64x64 sampling grid was applied to sample the desired excitation pattern. The dimension of the B0 fieldmap was same as that of the excitation field of view.

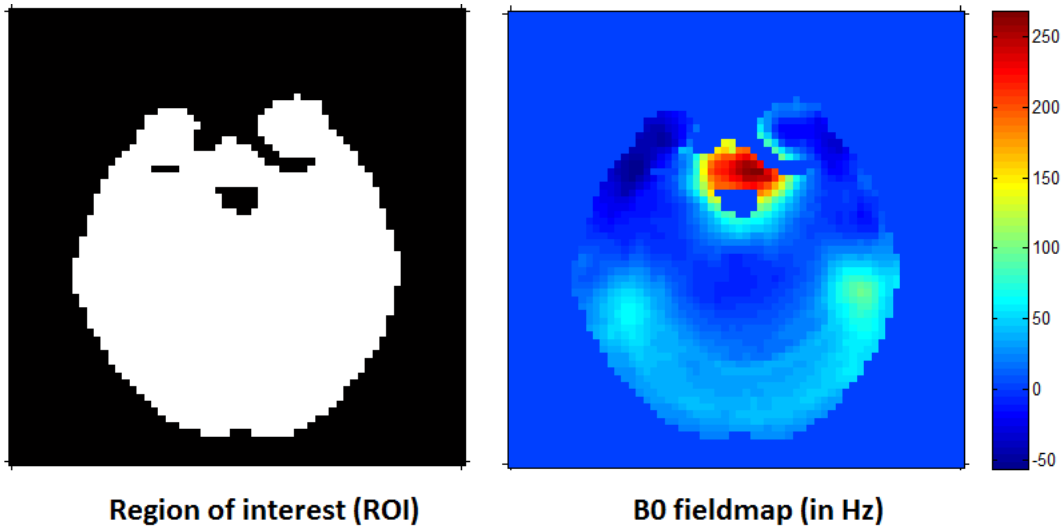

Figure 6.2: Region of interest and B0 fieldmap used in our RF pulse design.

8 transmission coils were used for the RF pulse design, and their sensitivity map was acquired with the same simulation presented in Chapter IV. Their sensitivity

map is shown in Figure 4.2. The target slice was 5 mm thick, and a sinc pulse with one side lobe exciting 10 degree tip-angle was used as a basis slice-selective pulse. The number of phase encoding locations in the simulation was set to be 5.

6.4 Results

6.4.1 90 degree tip-angle excitation

Figure 6.3 shows the magnitude of the transverse magnetization at different z-locations by different pulse designs. Figure 6.4 displays the phase of the transverse magnetization normalized by the phase at z=0 at different z-locations from two pulses. In other words, the phase at each z location is subtracted by the phase at z=0 to evaluate the through-plane phase variation, which can cause signal loss in the reconstructed image if it is very rapid as we discussed in Chapter V. The magnetization at $|z| > 5mm$ was not plotted because its magnitude was negligible. The scaled version of small tip angle pulse shows very irregular magnitude and phase whereas the proposed large tip-angle pulse design shows much better uniformity in both magnitude and phase of the excited transverse magnetization. The uniformity of transverse magnetization becomes deteriorated as the subslice location becomes farther from the slice center. For example, at the magnitude uniformity at z = $\pm$2mm is not as good as that at z = 0mm or $\pm$1mm. However, considering our pulse design does not explicitly regulate the through-plane slice profile, this result is surprisingly better than what we expected. We experimented with other slices and found that results from other slices have reasonably uniform through-plane magnitude and phase profiles though they are not presented here.

Figure 6.5 and Figure 6.6 show the k_x and k_y locations and the RF pulse weights before and after the proposed optimization. The normalized root mean squared error (NRMSE) of the excited transverse magnetization pattern decreased from 19%

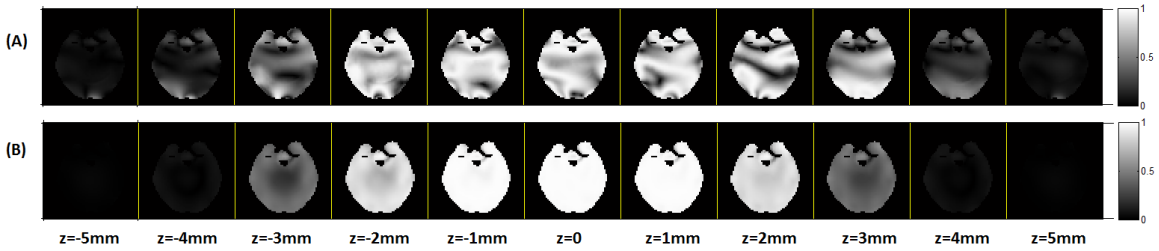

Figure 6.3: Transverse magnetization magnitude along z axis by different RF pulses. Top row (A) shows the transverse magnetization from the scaled version of a small tip-angle pulse, and the bottom row (B) shows our proposed large tip-angle RF pulse design. The large tip-angle design method shows significantly improved uniformity in the in-plane excitation pattern at each sub-slice location.

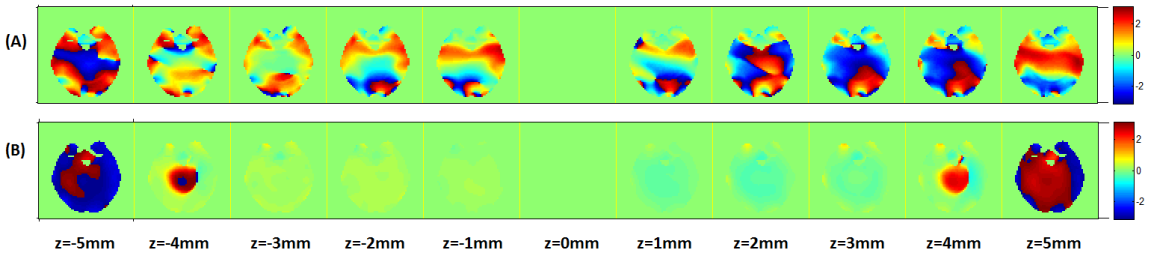

Figure 6.4: Transverse magnetization phase along z axis by different RF pulses. Top row (A) shows the transverse magnetization from the scaled version of a small tip-angle pulse, and the bottom row (B) shows our proposed large tip-angle RF pulse design. The large tip-angle design method shows much smaller phase variation, implying less signal loss in the reconstructed image.

to 17%. There is not much update for both the k_x and k_y locations and the RF pulse weights, explaining the small improvement in the excitation error. However, note that the error is quite larger than expected from the in-plane excitation profile displayed in Figure 6.3, because of the phase discrepancy between the excited pattern and the desired pattern. The NRMSE in the magnitude domain is in fact about 3%, suggesting that the excitation phase relaxation may help assessing the quality of the excited pattern in a fairer manner.

6.4.2 180 degree tip-angle inversion

The longitudinal magnetization from different pulse designs are presented in Figure 6.7. Our proposed method shows a significantly better uniform inversion pattern

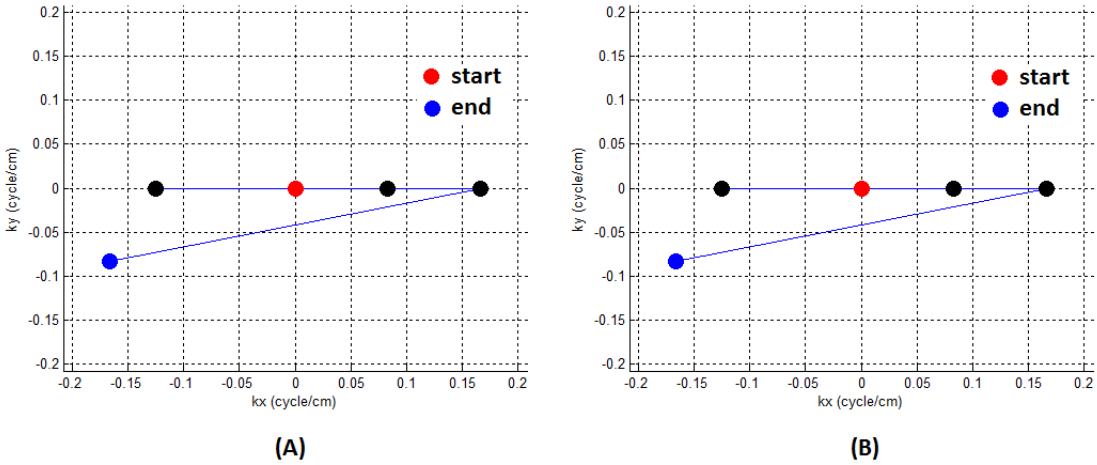

Figure 6.5: $k_x(n)$ and $k_y(n)$ comparison between before (A) and after (B) optimization for 90 degree excitation. In this case, k_x and k_y locations after the optimization did not change from the initializer.

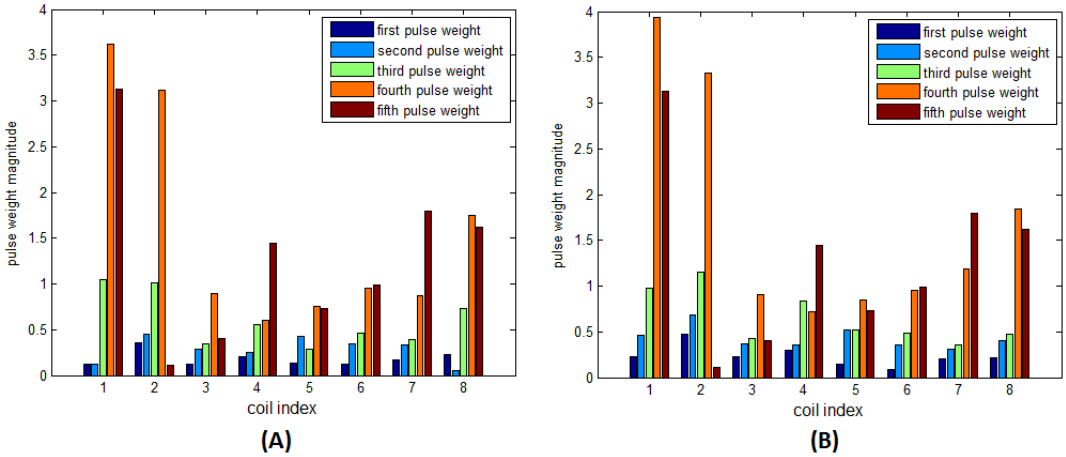

Figure 6.6: Magnitudes of RF pulse weights before (A) and after (B) the optimization. Only minor updates occurred.

at different subslice locations than the scaled small tip-angle RF pulse design. However, compared with the 90 degree excitation pattern, the through-plane slice profile of the longitudinal magnetization became thinner. The slice uniformity became notably degraded around z = ±2mm for the 90 degree excitation, but we could identify non-uniformity of the inverted magnetization started to become more visible from z = ± 1mm with our inversion pulse design.

Figure 6.8 and Figure 6.9 show the k_x and k_y locations and the RF pulse weights

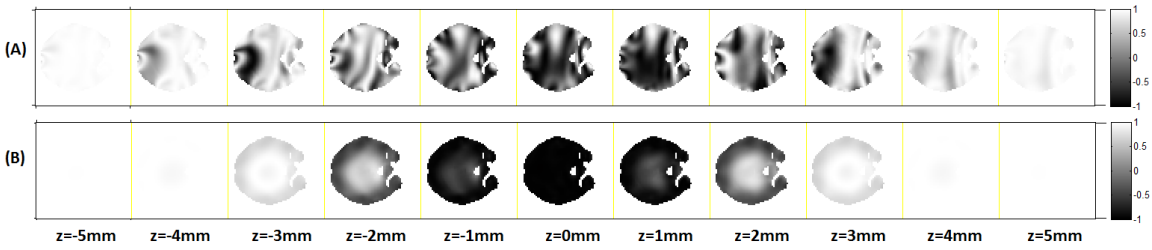

Figure 6.7: Longitudinal magnetization phase along z axis by different inversion pulse designs. Top row (A) displays the longitudinal magnetization from the scaled small tip-angle pulse, and the bottom row (B) presents our proposed large tip-angle RF pulse design. Our pulse design demonstrates a much more uniform longitudinal magnetization pattern.

before and after the proposed optimization for the inversion pulse design. The NRMSE of the excited longitudinal magnetization pattern reduced from 11% to 3%, which is a larger change than that of the 90 degree excitation pulse. The RF pulses show a larger update than k_x and k_y locations.

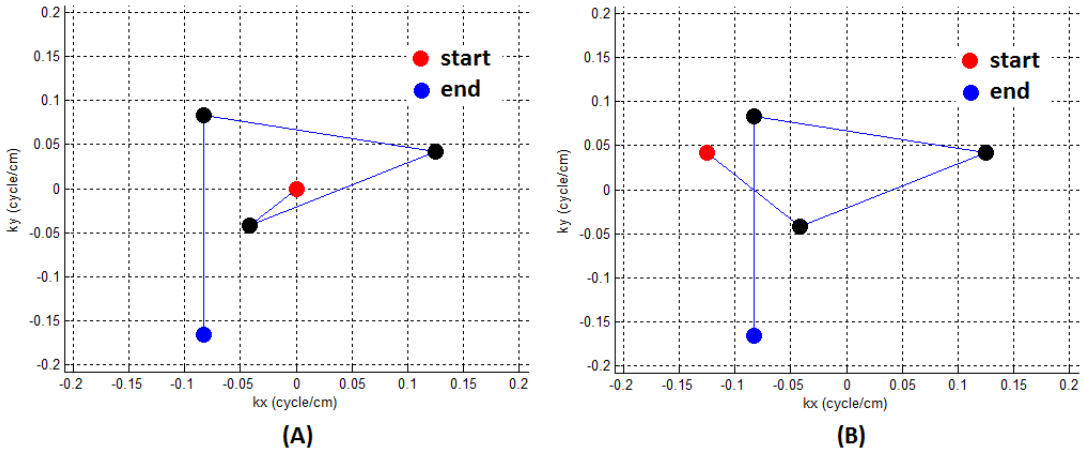

Figure 6.8: $k_x(n)$ and $k_y(n)$ comparison between before (A) and after (B) optimization for 180 degree excitation. In this case, only $(k_x(1), k_y(1))$ is updated.

6.5 Discussion

In this chapter, we introduced a joint design method for RF and gradient waveforms to obtain arbitrary tip-angle excitation with parallel excitation, and demonstrated its preliminary simulation results. To our knowledge, there was no previous journal article presenting a jointly optimization method for the RF and gradient

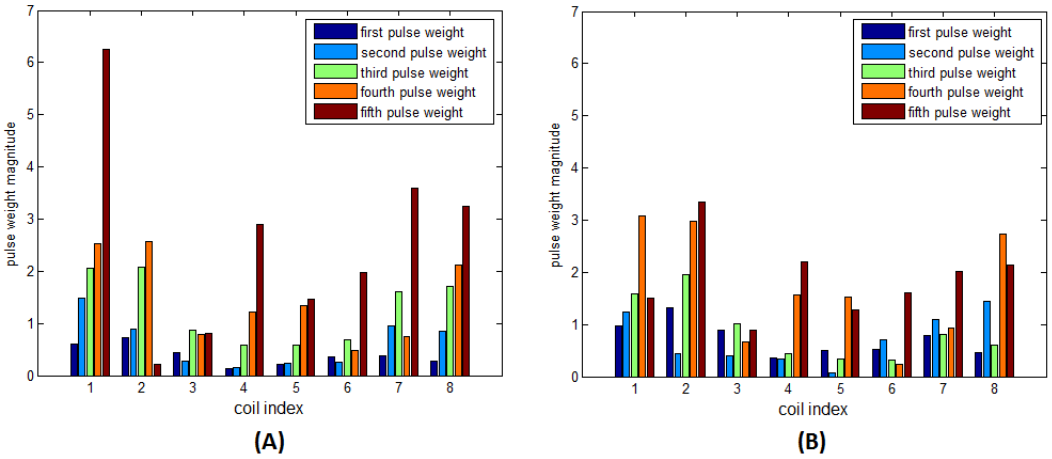

Figure 6.9: Magnitudes of RF pulse weights before (A) and after (B) the optimization. Compared to the case of the 90 degree excitation pulse design, a more major update occurred, resulting a larger improvement in the final RF pulse accuracy

waveforms in parallel excitation using our assumed pulse sequence, which is composed of trains of slice-selective RF pulses interleaved by in-plane gradient blips. We attempted to compute optimal RF pulse weights and gradient blips by locally refining an initial solution. In our optimization, we sequentially updated each basis RF pulse segment by fixing other parameters, and minimized our cost function with respect to the parameter chosen to be optimized. We repeated this process until there is no considerable improvement in the cost function value. The comparison with a scaled version of our previous small tip-angle design method shows that our new large tip-angle design method can achieve much higher excitation accuracy in both 90 degree excitation and 180 degree inversion RF pulse designs.

The minimizer found with our optimization algorithm converges to a local minimum around the initial solution, so it might be quite advantageous if we can find a good initializer. We have proposed a method to initialize the RF pulse weights and gradient waveforms by fitting them to the ideal B field in a greedy fashion. Another natural choice for the initializer may be the scaled version of the small tip-angle RF pulse, which we used as a reference to compare our design with. However, with our

experiments, the excitation error of the scaled small tip-angle RF pulse was much higher than that of our proposed initializer. For example, the normalized root mean squared error (NRMSE) of the excited pattern by the scaled small tip-angle RF pulse for the 90 degree excitation was about 71%, while the normalized excitation error by our proposed initializer was about 18%. The NRMSE of the small tip-angle RF pulse initializer after the RF pulse and gradient waveform update was about 31%, whereas that of our proposed initializer was about 12%. The reason for such high excitation error by the scaled small-tip pulse was that the magnetization became seriously overtipped in some regions. This may be avoided if we reduce the scaling factor, but upto now, we could not find any obvious way to determine it in an better way.

Experimentally, we learned that our RF pulse achieves a reasonable magnitude slice profile at different subslice location as show in Figure 6.4. However, the phase profile was harder to characterize than the magnitude profile. Figure 6.10 (A) illustrates the through-plane phase difference between z = -2mm to +2mm. It shows mostly moderate phase evolution, so it would not create serious signal loss. We can confirm this by comparing Figure 6.10 (B) and (C) where the sum of magnitude of transverse magnetization along z direction and the sum of complex transverse magnetization are displayed respectively. The complex sum image in Figure 6.10 shows slightly reduced amplitude overall, but it does not have regions with severe signal amplitude reduction. The signal loss from the through-plane phase variation was relatively moderate. But unfortunately, it could not be corrected by modifying the rephaser gradient at the end of the RF pulse sequence because the rate of the through-plane variation and its sign were spatially varying.

In our future research, we will seek to refine our method to further control the

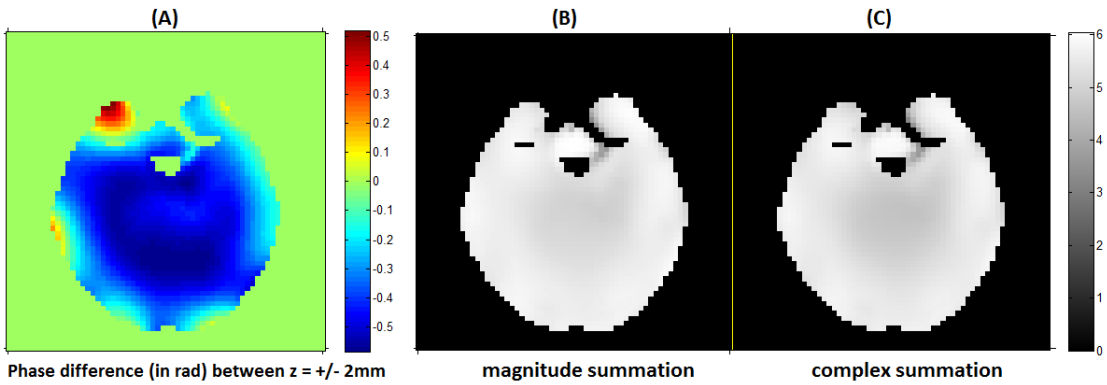

Figure 6.10: Through-plane phase difference in excitation pattern and resulting signal loss. (A) shows through-plane phase difference, and high phase difference is likely to cause signal loss in the reconstructed image. (B) and (C) are sum of excited transverse magnetization along through-plane direction to simulate how much signal loss is caused from through-plane phase difference within the excited slice. (B) is the sum of absolute magnetization and (C) is the sum of the complex magnetization. (B) and (C) are compared to isolate the signal loss by phase incoherence from the non-uniformity in the magnitude of the excited magnetization. (C) show a very slight shading around the center, suggesting that the signal loss from through-plane phase incoherence is not so severe.

through-plane slice profile. As briefly discussed above, our pulse design may yield imperfect through-plane slice profile in both magnitude and phase. In our experiment, we observed that different RF pulse trains have different effective slice-thickness. So, there may be a way to optimize the RF pulse weights considering not only magnetization at the slice center, but also magnetization at different slice locations to explicitly regulate the through-plane slice profile. This may involve modifying the pulse sequence to allow deposition of time-shifted basis pulse as presented in Chapter V to control the magnetization variation within the selected slice volume.

Our pulse design may be directly applicable to excitation of a large volume where no slice selection is necessary. Excitation of a whole brain is such an application. Recently, a small tip RF pulse design using spiral non-selective RF pulses [90] was proposed, but to our knowledge, no arbitrary tip-angle RF pulse design for parallel transmission has been proposed yet. In non-selective RF pulse design, there is no

need for the slice-select gradient. Therefore, we should first remove the slice-select gradient in our assumed pulse sequence and replace the slice-selective basis pulse with a hard pulse. Then we can apply our optimization algorithm to design a non-selective RF pulse. In the optimization, the absence of the slice-select gradient allows us to handle all the magnetization as if it is at the slice center, which makes the problem easier to solve than slice-selective excitation. With a little extension of the dimension of the desired excitation pattern, our current RF and gradient waveform optimization scheme can be used to design the non-selective RF pulse without much difficulty.

6.6 Conclusion

We have presented a joint design optimization method for RF pulse and gradient waveforms in parallel excitation to achieve an arbitrary tip-angle excitation. Our joint optimization algorithm uses the excited magnetization at the slice center to guide the optimization of the RF pulse and gradient waveform. In our preliminary simulation experiments, we have demonstrated the potential of our method with 90 degree excitation and 180 degree inversion. For our future research, we plan to investigate further improve our pulse design to explicitly control the through-plane slice profile. Also developing a fast computational scheme for our joint design method may be another interesting topic to pursue.

CHAPTER VII

Summary and Future Work

7.1 Summary

In this thesis, we have presented a fast joint optimization method for RF pulse and gradient waveforms in parallel excitation. In our optimization, we assumed an RF pulse sequence composed of trains of weighted slice-selective basis RF pulses interleaved by in-plane gradient blips. Our main contribution is that we have developed a fast joint design algorithm for RF and gradient waveforms for general slice-selective excitation with parallel transmission, which provides higher excitation accuracy than previous algorithms. The actual benefits from our pulse design depend on the applications. For example, in the application for the uniform excitation, higher excitation accuracy of our RF pulse design method can lead to the better image contrast because it is not compromised by unwanted shading or brightening that can result from excitation with low accuracy. In the application for the signal recovery for BOLD fMRI with multi-dimensional excitation, our pulse design could provide the image without severe signal loss, yielding a better opportunity to study the functional activation of brain regions that would have been otherwise impossible to investigate.

In Chapter III, we introduced a simple algorithm for a very basic pulse sequence

used to achieve the pseudo-continuous inversion for arterial spin labeling (PCASL). We extended the conventional PCASL sequence by employing parallel excitation to obtain spatial selectivity on the tagging plane. Our approach was applied to invert the spins only on the selected vessel locations. The conventional method for the vessel-selective PCASL used a single transmission coil and depended upon linear gradient blips to achieve the desired selectivity. However, the dependence on the linear gradient limited the applicability of the conventional method such that it is effective only when the vessels form a rectlinear geometry. On the other hand, our method acquired the selectivity by finding an optimal combination of transmission coil's sensitivity such that only selective vessels experience the normal PCASL RF pulse sequence. With our simulation experiments, we demonstrated that our method can achieve higher tagging efficiency than the conventional method for vessels with non-rectlinear vessel geometry. The main purpose of vessel selective PCASL is to obtain an accurate perfusion map of vessels, and the accuracy and robustness of the estimated perfusion map critically depends on the tagging efficiency. Therefore, we may expect that our method has high potential to provide a more accurate, robust way to estimate the perfusion territory of individual vessels.

In Chapter IV, we presented a fast greedy algorithm to jointly design RF pulse weights and gradient waveforms to mitigate B1 field inhomogeneity and thus obtain a uniform excitation pattern. Our method chooses PE locations considering off-resonance, and chooses the optimal PE location among a smaller set of candidate PE locations than the conventional method by culling effective candidates with a correlation test. In the simulation results, our method yielded an RF pulse with higher excitation accuracy in much shorter time than the previous algorithms. The improvement of excitation accuracy was achieved by considering the off-resonance

effect during the phase encoding location optimization, which has not been accounted for in previous methods. The accelerated computation of our method was due to replacing a large number of computationally expensive orthogonal projections with fast linear correlations implemented with FFT and diagonal matrix multiplications.

In Chapter V, we extended the pulse sequence introduced in Chapter IV to deposit a linear combination of time-shifted basis pulses for each slice-select gradient. This pulse sequence can create a local through-plane variation in the excited magnetization pattern, and we applied it to excite magnetization with a prephasing pattern to compensate for the off-resonance accrual along the through-plane direction in T2* weighted imaging. Our algorithm in Chapter IV was slightly modified to reflect the changes in the pulse sequence, and used to compute effective RF pulse and gradient waveforms for this problem. Our computer simulation result suggested that parallel excitation can help improving the excitation accuracy compared to the single coil excitation. The in-vivo experiment with single coil excitation demonstrated the potential of our RF pulse design approach to excite the desired magnetization pattern and correct for the signal loss problem.

Finally in Chapter VI, we introduced preliminary results of our novel joint design method for RF pulse and gradient waveforms to achieve excitation with an arbitrary tip-angle. Our method assumes the same RF pulse sequence introduced in Chapter IV and optimize the RF pulse weight and gradient waveforms based on the excited magnetization at the slice center. We sequentially update the RF pulse weight and gradient waveforms for each segment. In the update, we fix all other parameters except the one being updated. For the RF pulse update, we used a locally linearized Bloch-equation to find a simple linear relationship between the RF pulse update and the resulting transverse magnetization. For the gradient waveform update, we could

derive an analytical solution, which was easy to compute using FFT. The computer simulation results show that RF pulse and gradient waveforms computed with our method provides far higher excitation accuracy for 90 degree excitation and 180 degree inversion than the scaled version of our small tip-angle RF pulse design.

7.2 Future Work

Our proposed joint design methods are all based on a greedy approach, which selects the PE location among the candidates that reduces the cost function the most when added to the set of previously selected PE locations. Empirically, we have observed that the excitation accuracy of our proposed greedy optimization is comparable with or sometimes better than that of convex optimization methods [14, 16]. We claimed the benefits of our algorithm mostly by this relative comparison with previous methods, but we do not yet know whether the set of selected PE locations is globally optimal. A theoretical guarantee for the accuracy of our algorithm would be very hard to obtain, since the conditions to claim such optimality for the underlying greedy method is hard to verify in our setting, just as those of the convex approaches. Therefore, the only possible way to evaluate the global optimality of our method may be to conduct a exhaustive search for the optimal combination of PE locations from the entire candidates to find the globally optimal set of PE locations and then to compare it with our method. This would obviously take a very long time, but it could be very useful to find out how much improvement one may have through a more sophisticated PE location optimization. Especially for the signal recovery problem introduced in Chapter IV where the excitation accuracy of our proposed method is not so high enough, this evaluation may be very helpful to guide the direction of optimization we should develop in future. For example, if the excitation accuracy

of the globally optimal PE locations is not much higher than that of our method, it may be more practically beneficial to consider other ways for improvement such as a redesign of the RF pulse sequence.

For the signal recovery problem introduced in Chapter V, our proposed pulse design method did not achieve as high excitation accuracy as it did for the uniform excitation, and the computation time also increased as the size of the problem became bigger. There may be a few different approaches to further improve our optimization approach. Revisiting the convex optimization approach may be one option to improve the PE location selection procedure for higher excitation accuracy, since the convex optimization is in general known to have a better performance than greedy methods in terms of accuracy. The major challenge here would be reformulating the problem into a convex optimization problem considering off-resonance effects. Our RF pulse design method may be extended to include non-linear gradients such as shimming gradients to further improve the excitation accuracy. The use of non-linear gradients was first suggested in the signal acquisition side [91, 92], but recently, it has been started to be adopted in the RF pulse design [93, 94]. It may be an interesting opportunity to use non-linear shimming gradients to manipulate the B0 fieldmap pattern to make a desired excitation pattern easier to implement. The desired excitation pattern was a function of B0 fieldmap in a subslice-level resolution. Estimation of B0 fieldmap in such a high resolution for the entire brain volume may cause substantial overhead, so it may be advantageous if there could be any acceleration in either acquisition of the raw data for B0 fieldmap estimation or the estimation of the B0 fieldmap from the raw data. The RF pulse computation may be also accelerated by further reducing the number of parameters to optimize. In our proposed method, we had to compute the RF pulse for each coil, for every

coil can independently transmit an RF pulse. In [95], it was reported that every coil may not need to be driven with an independent amplifier to achieve high excitation accuracy. In other words, there may be a fewer RF amplifiers, thus fewer RF pulses than RF transmission coils. If this may be applicable to our signal recovery problem, it is likely that it can contribute to reduce the computation time, for the number of the RF pulses to compute can be reduced.

In any RF pulse design, both the RF pulse and gradient waveforms should be computed subject to the hardware capability constraints. In all of our methods presented in this thesis, gradient waveforms are determined satisfying the hardware constraints because we first optimize the linear phases that the gradient waveforms are supposed to create, and then derive the gradient waveforms from them using the hardware limit. However, in RF pulse optimization, we did not consider explicitly controlling the maximum RF pulse amplitude. This is in part due to that we do not have working parallel excitation hardware available, so we could not assume a realistic hardware specification. However, we should still need to consider an efficient way to incorporate RF pulse amplitude regularization with an arbitrary hardware constraint. Another important factor in RF pulse regularization is that we also need to consider RF power deposition. This is indirectly related with controlling the peak RF pulse amplitude, because a smaller RF pulse tends to deposit less power. However, there may be a more direct way to control the RF pulse power deposition. In parallel excitation, this becomes more complicated because the power deposition pattern varies locally. It is a very challenging issue, but monitoring the local RF pulse power deposition pattern, and use it to guide RF pulse optimization would be very crucial for clinical applications.

Our joint optimization may be extended to adopt spectral selectivity in the de-

sired excitation pattern. In our applications, we only focused on the excitation of water. However, in many clinical imaging applications, either the water excitation is preceded by fat-saturation or water-selective excitation is performed to suppress the excitation of fat. Parallel excitation has been applied to uniform fat-saturation in presence of severe off-resonance [96], but this method did not consider the joint optimization of RF pulse and gradient waveforms, so it may be possible to further improve the spectral selectivity with our joint design. One important factor to consider here is that in this problem, it has been reported that the phase relaxation of the excitation pattern can contribute to improving the excitation accuracy [25, 54, 83]. Therefore in modifying our joint design algorithm to these applications, we may need to also consider the phase relaxation to maximize the excitation accuracy.

Another interesting topic to investigate is to develop a faster computation scheme for the joint optimization of large tip-angle RF pulse and gradient waveforms. In our proposed optimization, estimating the magnetization behavior took a relatively longer time than the linear estimation used in a small tip-angle RF pulse design because it involved performing a 3D rotation for each voxel. SLR pulse design methods [19, 20, 97] may be an interesting reference for solving this issue because it solved the similar problem of processing a large number of 3D rotations by using a more compact spinor-domain representation for the rotation. Grissom et al. [98] recently proposed to extend the SLR pulse design for the multi-dimensional excitation pulse design, so this may serve another intriguing reference in developing a new, fast computation scheme for our joint design method for RF pulse and gradient waveforms using parallel excitation.

BIBLIOGRAPHY

BIBLIOGRAPHY

[1] U. Katscher, P. Börnert, C. Leussler, and J. S. van den Brink. Transmit SENSE. *Magnetic Resonance in Medicine*,49(1):144-150, 2003.

[2] Y. Zhu. Parallel excitation with an array of transmit coils. *Magnetic Resonance in Medicine*, 51(4):775-784, 2004.

[3] F Bloch. W. W. Hensen, and M. E. Packard. The Nuclear Induction Experiment. *Physics Review*, 70:460-473, 1946.

[4] E. T. Jaynes. Matrix Treatment of Nuclear Induction. *Physics Review*, 98:1099, 1955.

[5] D. I. Hoult. The Solution of the Bloch Equations in the Presence of a Varying B1 Field-An Approach to Selective Pulse Analysis. *Journal of Magnetic Resonance*, 82:571-587, 1989.

[6] J. M. Pauly, D. G. Nishimura, and A. Macovski. A k-space analysis of small-tip-angle excitation. *Magnetic Resonance in Medicine*, 81:43.56, 1989.

[7] P. Börnert and B. Aldefeld. On spatially selective RF excitation and its analogy with spiral MR image acquisition. *Magma: Magnetic Resonance Materials in Physics, Biology and Medicine*, 7:166-178, 1998.

[8] H. Schomberg and P. Börnert. Off-resonance correction of nD spatially selective RF pulses. *In: Proceedings of the 6th Annual Meeting of ISMRM, Sydney, Australia*, p 2059, 1998.

[9] D. C. Noll, C. H. Meyer, J. M. Pauly, D. G. Nishimura, and A. Macovski. A homogeneity correction method for magnetic resonance imaging with timevarying gradients. *IEEE Transactions on Medical Imaging*, 10:629-637, 1991.

[10] C. Y. Yip, J. A. Fessler, and D. C. Noll. Iterative RF pulse design for multidimensional, small-tip-angle selective excitation. *Magnetic Resonance in Medicine*, 54(4):908.917, 2005.

[11] C. Y. Yip, J. A. Fessler, and D. C. Noll. Advanced three-dimensional tailored RF pulse for signal recovery in T2*-weighted functional magnetic resonance imaging. *Magnetic Resonance in Medicine*, 56(5):1050-9, 2006.

[12] S. Saekho, C. Y. Yip, D. C. Noll, F. E. Boada, and V. A. Stenger. Fast-kz Three-Dimensional Tailored Radiofrequency Pulse for Reduced B1 Inhomogeneity. *Magnetic Resonance in Medicine*, 55:719-724, 2006.

[13] C. Y. Yip, W. A. Grissom, J. A. Fessler, and D. C. Noll. Joint design of trajectory and RF pulses for parallel excitation. *Magnetic Resonance in Medicine*, 58(3):598-604, 2007.

[14] A. C. Zelinski, L. L. Wald, K. Setsompop, V. A. Alagappan, B. A. Gagoski, V. K. Goyal, and E. Adalsteinsson. Fast Slice-Selective Radio-Frequency Excitation Pulses for Mitigating B_1^+ Inhomogeneity in the Human Brain at 7 Tesla. *Magnetic Resonance in Medicine*, 59:1355-1364, 2008.

[15] S. S. Chen, D. L. Donoho, and M. A. Saunders. Atomic decomposition by basis pursuit. *SIAM Journal on Scientific Computing*, 20(1):33-61, 1998.

[16] A. C. Zelinski, L. L. Wald, K. Setsompop, V. K. Goyal, and E. Adalsteinsson. Sparsity-Enforced Slice-Selective MRI RF Excitation Pulse Design. *IEEE Transacations on Medical Imaging*, 27(9):1213-1229, 2008.

[17] S. M. Conolly, D. G. Nishimura, and A. Macovski. Optimal control solutions to the magnetic resonance selective excitation problem. *IEEE Transactions on Medical Imaging*, 5:106-115, 1986.

[18] J. M. Pauly, D. G. Nishimura, and A. Macovski. A linear class of large-tip-angle selective excitation pulses. *Journal of Magnetic Resonance*, 82(3):571-587, 1989.

[19] M. Shinnar and J. S. Leigh. The application of spinors to pulse synthesis and analysis. *Magnetic Resonance in Medicine*, 12:93-98, 1989.

[20] P. L. Roux. Exact synthesis of radiofrequency waveforms. *Proceedings of 7th Annual Meeting of SMRM*, p.1049, 1988.

[21] T.S. Ibrahim, R. Lee, A. M. Abduljalil, B. A. Baertlein, and P. M. Robitaille. Dielectric resonances and B(1) field inhomogeneity in UHFMRI: computational analysis and experimental findings. *Magnetic Resonance Imaging*, 19:219-226, 2001.

[22] Q. X. Yang, J. Wang, X. Zhang, C. M. Collins, M. B. Smith, H. Liu, X. H. Zhu, J. T. Vaughan, K. Ugurbil, and W. Chen. Analysis of wave behavior in lossy dielectric samples at high field. *Magnetic Resonance in Medicine*, 47:982-989, 2002.

[23] C. M. Collins, W. Liu, W. Schreiber, Q. X. Yang, and M. B. Smith. Central brightening due to constructive interference with, without, and despite dielectric resonance. *Journal of Magnetic Resonance Imaging*, 21:192-196, 2005.

[24] J. A. Heilman, J. D. Derakhshan, M. J. Riffe, N. Gudino, J. Tkach, C. A. Flask, J. L. Duerk, and M. A. Griswold. Parallel excitation for B-field insensitivie fat-saturation prepartion. *Magnetic Resonance in Medicine*, 2012 Jan 13. online available.

[25] S. J. Malik, D. J. Larkman, and J. V. Hajnal. Subject-specific water-selective imaging using parallel transmission. *Magnetic Resonance in Medicine*, 63(4):988-997, 2010.

[26] J. Nielsen, D. Yoon, and D. C. Noll. Toward robust banding suppression in balanced SSFP using a two-pulse RF pre-phasing approach. *ISMRM Third International Workshop on Parallel MRI*, 2009.

[27] J. Nielsen, D. Yoon, and D. C. Noll. Small-tip fast recovery imaging using non-slice selective tailored tip-up pulses and radiofrequency-spoiling. *Magnetic Resonance in Medicine*, 20120 Apr 17. online available.

[28] D. Yoon, J. A. Fessler, A. C. Gilbert, and D. C. Noll. Simultaneous signal loss correction from B1 and B0 field inhomogeneity in BOLD fMRI with parallel excitation. *ISMRM Third International Workshop on Parallel MRI*, 2009.

[29] W. Deng, C. Yang, V. Alagappan, L. L. Wald, F. E. Boada, and V. A. Stenger. Simultaneous z-shim method for reducing susceptibility artifacts with multiple transmitters. *Magnetic Resonance in Medicine*, 61(2):255-259, 2009.

[30] D. K. Sodickson and W. J. Manning. Simultaneous acquisition of spatial harmonics (SMASH): Fast imaging with radiofrequency coil arrays. *Magnetic Resonance in Medicine*, 38(4):591-603, 1997.

[31] K. P. Pruessmann, M. Weiger, M. B. Scheidegger, and P. Boesiger. SENSE: Sensitivity encoding for fast MRI. *Magnetic Resonance in Medicine*, 42(5):952-962, 1999.

[32] M. A. Griswold, P. M. Jakob, R. M. Heidemann, M. Nittka, V. Jellus, J. Wang, B. Kiefer, and A. Haase. Generalized autocalibrating partially parallel acquisitions (GRAPPA). *Magnetic Resonance in Medicine*, 47(6):1202-1210, 2002.

[33] W. A. Grissom, C. Y. Yip, Z. Zhang, V. A. Stenger, J. A. Fessler, and D. C. Noll. Spatial domain method for the design of RF pulses in multicoil parallel excitation. *Magnetic Resonance in Medicine*, 56(3):620-9, 2006.

[34] Z. Zhang, C. Y. Yip, W. A. Grissom, D. C. Noll, F. E. Boada, and V. A. Stenger. Reduction of transmitter B1 inhomogeneity with transmit SENSE slice-select pulses. *Magnetic Resonance in Medicine*, 57(5):842-847, 2007.

[35] J. A. Heilman, J. J. Derakhshan, M. J. Riffe, N. Gudino, J. Tkach, C. A. Flask, J. L. Duerk, and M. A. Griswold. B0 and B1 correction using the inherent degrees of freedom of a multi-channel transmit array. *In: Proceedings of the 17th Annual Meeting of ISMRM, Honolulu, U.S.A.*, p.251, 2009.

[36] J. A. Fessler and B. P. Sutton. Nonuniform fast Fourier transforms using min-max interpolation. *IEEE Transactions on Signal Processing*, 51(2):560-574, 2003.

[37] J. A. Tropp. Algorithms for Simultaneous Sparse Approximation (Parts I and II). *Signal Processing, special issue Sparse approximations in signal and image processing*, 86:589-602, 2006.

[38] D. Yoon, H. Jahanian, D. C. Noll, and L. Hernandez-Garcia. Spatially Selective PCASL with Parallel Excitation. *In: Proceedings of the 19th Annual Meeting of ISMRM, Montreal, Canada.*, p.2087, 2011.

[39] D. S. Williams, J. A. Detre, J. S. Leigh, and A. P. Koretsky. Magnetic resonance imaging of perfusion using spin inversion of arterial water. *Proceedings of the National Academy of Sciences*, 89(1):212-216, 1992.

[40] N. P. Davies, and P. Jezzard. Selective arterial spin labeling (SASL): perfusion territory mapping of selected feeding arteries tagged using two-dimensional radiofrequency pulses. *Magnetic Resonance in Medicine*, 49(6):1133-1142, 2003.

[41] J. Hendrikse, J. van der Grond, H. Lu, P.C. van Zijl, and X. Golay. Flow territory mapping of the cerebral arteries with regional perfusion MRI. *Stroke*, 35(4), 882-887, 2004.

[42] R. Werner, D. G. Norris, K. Alfke, H. M. Mehdorn, and O. Jansen. Continuous artery-selective spin labeling (CASSL). *Magnetic Resonance in Medicine*, 53(5):1006-1012, 2005.

[43] G. Zaharchuk, P.J. Ledden, K. K. Kwong, T. G. Reese, B. R. Rosen, and L. L. Wald. Multislice perfusion and perfusion territory imaging in humans with separate label and image coils. *Magnetic Resonance in Medicine*, 41(6):1093-1098, 1999.

[44] K. Alfke, R. Werner, M. Helle, A. Rohr, K. Borsch, R. Stingele, and O. Jansen. Magnetic resonance imaging of individual cerebral perfusion territories improves the diagnosis of embolic stroke. *Journal of Computer Assisted Tomography*, 31(6):894-95, 2007.

[45] J. Hendrikse, A. van der Zwan, L. M. Ramos, M. J. P. van Osch, X. Golay, C. A. Tulleken, and J. van der Grond. Altered flow territories after extracranial-intracranial bypass surgery. *Neurosurgery*, 57(3):486-94, 2005.

[46] X. Golay, J. Hendrikse, and J. van Der Grond. Application of regional perfusion imaging to extra-intracranial bypass surgery and severe stenoses. *Journal of Neuroradiology*, 32(5):321-24, 2005.

[47] P. J. van Laar, J. van der Grond, W. P. Mali, and J. Hendrikse. Magnetic resonance evaluation of the cerebral circulation in obstructive arterial disease. *Cerebrovascular Diseases*, 21(5-6):297-306, 2006.

[48] P. J. van Laar, J. Hendrikse, X. Golay, H. Lu, M. J. P. van Osch, and J. van der Grond. In vivo flow territory mapping of major brain feeding arteries. *Neuroimage*, 29(1):136-44, 2006.

[49] E. C. Wong. Vessel-encoded arterial spin-labeling using pseudocontinuous tagging. *Magnetic Resonance in Medicine*, 58(6):1086-1091, 2007

[50] T. W. Okell, M. A. Chappell, M. W. Woolrich, M. Gunther, D. A. Feinberg, and P. Jezzard. Vessel-encoded dynamic magnetic resonance angiography using arterial spin labeling. *Magnetic Resonance in Medicine*, 64(2):698-706, 2010.

[51] M. A. Chappell, T. W. Okell, P. Jezzard, and M. W. Woolrich. A general framework for the analysis of vessel encoded arterial spin labeling for vascular territory mapping. *Magnetic Resonance in Medicine*, 64(5):1529-1539, 2010.

[52] M. Helle, D. G. Norris, S. Rufer, K. Alfke, O. Jansen, and M. J. P. Osch. Superselective pseudocontinuous arterial spin labeling. *Magnetic Resonancne in Medicine*, 64(3):777-786, 2010.

[53] W. Dai, D. Garcia, C. de Bazelaire, and D. C. Alsop. Continuous flow-driven inversion for arterial spin labeling using pulsed radio frequency and gradient fields. *Magnetic Resonance in Medicine*, 60(6):1488-97. 2008.

[54] K. Setsompop, L. L. Wald, V. Alagappan, B. A. Gagoski, and E. Adalsteinsson. Magnitude least squares optimization for parallel radio frequency excitation design demonstrated at 7 Tesla with eight channels. *Magnetic Resonance in Medicine*, 59(4):908-915. 2008.

[55] K. N. Kurpad, E. B. Boskamp, and S. M. Wright. A parallel transmit volume coil with independent control of currents on the array elements. *In: Proceedings of the 13th Annual Meeting of ISMRM, Miami Beach, U. S. A.*, p.16, 2005.

[56] S. M. Wright. 2D full-wave modeling of SENSE coil geometry factors at high fields. *In: Proceedings of the 10th Annual Meeting of ISMRM, Honolulu, U. S. A.*, p.854, 2002.

[57] A. Oliver-Taylor, R. J. Ordidge, and D. L. Thomas. Parallel Transmit Vessel Selective Arterial Spin Labelling: A Proof of Concept Simulation. *In: Proceedings of the 19th Annual Meeting of ISMRM, Montreal, Canada.*, p.2086, 2011.

[58] H. Jahanian, D. C. Noll, and L. Hernandez-Garcia. B0 field inhomogeneity considerations in pseudo-continuous arterial spin labeling (pCASL): effects on tagging efficiency and correction strategy. *NMR in Biomedicine*, 24(10):1202-1209, 2011.

[59] D. Yoon, J. A. Fessler, A. C. Gilbert, and D. C. Noll. Fast joint design method for parallel excitation RF pulse and gradient waveforms considering off-resonance. *Magnetic Resonance in Medicine*, 68(1):278-285, 2012.

[60] C. Ma, D. Xu, K. F. King, and Z. P. Liang. Joint design of spoke trajectories and RF pulses for parallel excitation. *Magnetic Resonance in Medicine*, 65(4):973-985, 2011.

[61] C. Yang, W. Deng, and V. A. Stenger. Simple analytical dual-band spectral-spatial RF pulses for B1+ and susceptibility artifact reduction in gradient echo MRI. *Magnetic Resonance in Medicine*, 65(2):370-376, 2011

[62] K. Setsompop, V. Alagappan, A. C. Zelinski, A. Potthast, U. Fontius, F. Hebrank, F. Schmitt, L. L. Wald, and E. Adalsteinsson. High-flip-angle slice-selective parallel RF transmission with 8 channels at 7 T. *Journal of Magnetic Resonance*, 195(1):76-84, 2008.

[63] W. A. Grissom, A. B. Kerr, P. Stang, G. C. Scott, and J. M. Pauly. Joint Design of Large-Tip-Angle RF and Gradient Waveforms in Parallel Excitation. *ISMRM Third International Workshop on Parallel MRI*, 2009.

[64] D. Chen, F. Bornemann, M. W. Vogel, L. I. Sacolick , G. Kudielka, and Y. Zhu. Sparse parallel transmit pulse design using orthogonal matching pursuit method. *In: Proceedings of the 17th Annual Meeting of ISMRM, Honolulu, U. S. A.*, p.171, 2009.

[65] D. Yoon, R. Maleh, A. C. Gilbert, J. A. Fessler, and D. C. Noll. Fast selection of phase encoding locations in parallel excitation. *In: Proceedings of the 17th Annual Meeting of ISMRM, Honolulu, U.S.A.*, p.2595, 2009.

[66] Y. C. Pati, R. Rezaiifar, and P. S. Krishnaprasad. Orthogonal matching pursuit: recursive function approximation with applications to wavelet decomposition. *In: Proceedings of the 27th Asilomar Conference on Signals, Systems and Computers, Pacific Grove, U. S. A.*, p.40-44, 1993.

[67] S. J. Reeves, and Zhao Z. Sequential algorithms for observation selection. *IEEE Transactions on Signal Processing*, 47(1):123-132, 1999.

[68] D. Needell, and Tropp JA. CoSaMP : Iterative signal recovery from incomplete and inaccurate samples. *Communications of the ACM*, 53(12):93-100,2010.

[69] S. Ogawa, T. M. Lee, A. S. Nayak, P. Glynn. Oxygenation-sensitive contrast in magnetic resonance image of rodent brain at high magnetic fields. *Magnetic Resonance in Medicine*, 14(1):68-78, 1990.

[70] J. L . Wilson, M. Jenkinson, and P. Jezzard. Optimization of static field homogeneity in human brain using diamagnetic passive shims. *Magnetic Resonance in Medicine*, 48(5):906-914, 2002.

[71] J. J. Hsu, and G. H. Glover. Mitigation of susceptibility-induced signal loss in neuroimaging using localized shim coils. *Magnetic Resonance in Medicine*, 53(2):243-248, 2005.

[72] E. C. Wong, and Y. Mazaheri. Shimming of the inferior frontal cortex using an external local shim coil. *In: Proceedings of the 12th Annual Meeting of ISMRM, Kyoto, Japan*, p. 520, 2004.

[73] R. T. Constable and D. D. Spencer. Composite image formation in z-shimmed functional MR imaging. *Magnetic Resonance in Medicine*, 42(1):110-117, 1999.

[74] A. W. Song. Single-shot EPI with signal recovery from the susceptibility induced losses. *Magnetic Resonance in Medicine*, 46:407-411, 2001.

[75] Single-shot interleaved z-shim EPI with optimized compensation for signal losses due to susceptibility-induced field inhomogeneity at 3 T. H. Gu, H. Feng, W. Zhan, S. Xu, D. A. Silbersweig, E. Stern E, and Y. Yang. *Neuroimage*, 17(3):1358-64, 2002.

[76] Improved Interleaved Single-shot z-shim EPI via Spatial and Temporal Encoding W. S. Hoge, H. Pan, H. Tan, E. Stern, and R. A. Kraft. *In: Proceedings of the 19th Annual Meeting of ISMRM, Montreal, Canada.*, p. 4389, 2011.

[77] K. D. Merboldt, J. Finsterbusch, and J. Frahm. Reducing inhomogeneity artifacts in functional MRI of human brain activation-thin slices vs. gradient compensation. *Journal of Magnetic Resonance*, 145(2):184-91, 2000

[78] G. H. Glover and S. Lai. Reduction of susceptibility effects in BOLD fMRI using tailored RF pulses. *Proceedings of the ISMRM 6th Scientific Meeting, Sydney*, p.298, 1998.

[79] N-K. Chen and A. Wyrwicz. Removal of intravoxel dephasing artifact in gradient-echo images using a field-map based RF refocusing technique. *Magnetic Resonance in Medicine*, 42(4):807-812, 1999.

[80] V. A. Stenger, F. E. Boada, and D. C. Noll. Variable-density spiral 3D tailored RF pulses. *Magnetic Resonance in Medicine*, 50(5):1100-1106, 2003.

[81] B. P. Sutton, D. C. Noll, and J A Fessler. Fast, iterative image reconstruction for MRI in the presence of field inhomogeneities. *IEEE Transactions on Medical Imaging*, 22(2):178-88, 2003.

[82] A. K. Funai, J. A. Fessler, D. T. B. Yeo, V. T. Olafsson, and Douglas C Noll. Regularized field map estimation in MRI. *IEEE Transactions on Medical Imaging*, 27(10):1484-94, 2008.

[83] W. A. Grissom, M. M. Khalighi, L. I. Sacolick, B. K. Rutt, M. W. Vogel. Small-tip-angle spokes pulse design using interleaved greedy and local optimization methods. *Magn Reson Med*, online available, Mar. 2012.

[84] D. Xu, K. F. King, Y. Zhu, G. C. McKinnon, and Z-P Liang. A noniterative method to design large tip-angle multidimensional spatially-selective radio frequency pulses for parallel transmission. *Magnetic Resonance in Medicine*, 58(2):326-334, 2007.

[85] D. Xu, K. F. King, Y. Zhu, G. McKinnon, and Z-P Liang. Designing multichannel, multidimensional, arbitrary flip angle RF pulses using an optimal control approach. *Magnetic Resonance in Medicine*, 59(3),547-560, 2008.

[86] W. A. Grissom, C. Y. Yip, S. M. Wright, J. A. Fessler, and D. C Noll. Additive angle method for fast large-tip-angle RF pulse design in parallel excitation. *Magnetic Resonance in Medicine*, 59(4):779-787, 2008.

[87] K. Setsompopa, V. Alagappan, A. C. Zelinski, A. Potthast, U. Fontius, F. Hebrank, F. Schmitt, L. L. Wald, and E. Adalsteinsson. High-flip-angle slice-selective parallel RF transmission with 8 channels at 7 T. *Journal of Magnetic Resonance*, 195(1):76-84, 2008.

[88] W. A. Grissom, D. Xu, A. B. Kerr, J. A. Fessler, and D. C. Noll. Fast large-tip-angle multidimensional and parallel RF pulse design in MRI. *IEEE Transactions on Medical Imaging*, 28(11):1688-1702, 2009.

[89] H. Zheng, T. Zhao, Y. Qian, T. S. Ibrahim, and F. E. Boada. Improved large tip angle parallel transmission pulse design through a perturbation analysis of the Bloch equation. *Magnetic Resonance in Medicine*, 66(3):687-696, 2011.

[90] S. J. Malik, S. Keihaninejad, A Hammers, and J. V. Hajnal. Tailored excitation in 3D with spiral nonselective (SPINS) RF pulses. *Magnetic Resonance in Medicine*, 67(5):1303-1315, 2012.

[91] J. Hennig, A. M. Welz, G. Schultz, J. Korvink, Z. Liu, O. Speck,and M. Zaitsev. Parallel imaging in non-bijective, curvilinear magnetic field gradients: a concept study. *Magnetic Resonance Materials in Physics, Biology and Medicine*, 21(1-2):5-14, 2008.

[92] J. P. Stockmann, P. A. Ciris, G. Galiana, L. Tam, and R. T. Constable. O-space imaging: Highly efficient parallel imaging using second-order nonlinear fields as encoding gradients with no phase encoding. *Magnetic Resonance in Medicine*, 64(2):447-456, 2010.

[93] W. A. Grissom, L. Sacolick, and M. W. Vogel. B1+ Inhomogeneity Compensation Using 3D Parallel Excitation Is Enhanced by Simultaneous Linear and Nonlinear Gradient Encoding. *In: Proceedings of the 19th Annual Meeting of ISMRM, Montreal, Canada*, p. 2898, 2011.

[94] C. Ma, K. F. King, D. Xu, and Z. P. Liang. A Spatial-Spectral Pulse Approach for Reduced FOV Excitation Using Second-Order Gradients. *In: Proceedings of the 19th Annual Meeting of ISMRM, Montreal, Canada*, p. 2899, 2011.

[95] V. Alagappan, J. Nistler, E. Adalsteinsson, K. Setsompop, U. Fontius, A. Zelinski, M. Vester, G. C. Wiggins, F. Hebrank, W. Renz, F. Schmitt, and L. L. Wald. Degenerate mode band-pass birdcage coil for accelerated parallel excitation. *Magnetic Resonance in Medicine*, 57(6):1148-58, 2007.

[96] J. A. Heilman, J. D. Derakhshan, M. J. Riffe, N. Gudino, J. Tkach, C. A. Flask, J. L. Duerk, and M. A. Griswold. Parallel excitation for B-field insensitive fat-saturation preparation *Magnetic Resonance in Medicine*, 68(5):631-638, 2012.

[97] J. M. Pauly, P. Le Roux, D. Nishimura, and A. Macovski. Parameter Relations for the Shinnar-Le Roux Selective Excitation Pulse Design Algorithm. *IEEE Transactions on Medical Imaging*, 10(1):53-65, 1991.

[98] W. A. Grissom, G. C. McKinnon, and M. W. Vogel. Nonuniform and multidimensional Shinnar-Le Roux RF pulse design method *Magnetic Resonance in Medicine*, Dec., 2012, online available.